

AN ABSTRACT OF THE THESIS OF

Thomas L'Estrange for the degree of Master of Science in Mechanical Engineering
presented on August 3, 2015.

Title: Experimental Characterization of a Supercritical Carbon Dioxide
Microchannel Solar Thermal Receiver

Abstract approved:

Vinod Narayanan

Characterization of a microchannel solar thermal receiver for supercritical carbon dioxide (sCO₂) is presented. The receiver design is based on conjugate computational fluid dynamics and heat transfer simulations as well as thermo-mechanical stress analysis. Two lab scale receivers with a 2x2 cm² absorber area are fabricated and experimentally characterized – a parallel microchannel design and a microscale pin fin array design. Static pressure experiments are used to demonstrate receiver integrity at the design pressure of 125 bar at 750°C surface temperature. A concentrated solar simulator was designed and assembled to characterize the thermal performance of the

lab scale receiver test articles. Results indicate that, for a fixed exit fluid temperature of 650°C, increase in incident heat flux results in an increase in receiver and thermal efficiency. At a fixed heat flux, efficiency decreases with an increase in receiver surface temperature. The ability to absorb flux of up to 100 W/cm² at thermal efficiency in excess of 90 percent and exit fluid temperature of 650°C using the microchannel receiver is demonstrated. Pressure drop for the pin array at the maximum flow rate for heat transfer experiments is less than 0.64 percent of typical line pressure of 200 bar. Following the successful test of the 2 x 2 cm lab-scale receiver, a larger 8x8 cm² integrated receiver was designed and fabricated. The integrated receiver is shown to withstand 200 bar of static pressure at 600°C. Furthermore, infrared imaging is used to glean the flow distribution from the headers into the microscale region of the receiver. While the integrated receiver could not be tested in the solar simulator due to limitations of the facility, receiver scale-up from 2 x 2 cm to 8 x 8 cm with more effective material usage is demonstrated.

©Copyright by Thomas L'Estrange

August 3, 2015

All Rights Reserved

Experimental Characterization of a Supercritical Carbon Dioxide Microchannel Solar
Thermal Receiver

by
Thomas L'Estrange

A THESIS
submitted to
Oregon State University

in partial fulfillment of
the requirements for the
degree of

Master of Science

Presented August 3, 2015

Commencement June 2016

Master of Science thesis of Thomas L'Estrange presented on August 3, 2015

APPROVED:

Major Professor, representing Mechanical Engineering

Head of the School of Mechanical, Industrial and Manufacturing Engineering

Dean of the Graduate School

I understand that my thesis will become part of the permanent collection of Oregon State University libraries. My signature below authorizes release of my thesis to any reader upon request.

Thomas L'Estrange, Author

ACKNOWLEDGEMENTS

I would like to express my deepest appreciation to my friend, project member, and lab mate Eric Truong. Without his persistent push to help me continue my education I would not have been a part of this project and would have forgone many rewarding experiences.

I would like to thank my professor, Dr. Vinod Narayanan. Even with his relentless commitments he was always available to help. His work ethic and the level of quality he demands on any project has shaped the way I see research and has made me expect a high level of quality out of myself and those I work with. Without his help this thesis would not have been possible.

I would like to thank my project members, Dr. Sourabh Apte, Dr. Kevin Drost, Charles Rymal, Dr. Erfan Rasouli, Eric Truong, and Dr. Vinod Narayanan, whose contribution and drive to tackle the demanding deadlines of the project molded the successful outcome.

I would like to thank every technician, receptionist, teacher, student, tradesman and salesman that took the time to answer my questions and help to fulfill my requirements. I know I took a lot of your time.

I would like to express my appreciation to my committee members Dr. Sourabh Apte, Dr. Kevin Drost, and Dr. John Sessions for their insight and judgment on my research. Finally I would like to thank all of my friends and family that stood by all the stressful times I put myself through by procrastinating and helped me to find a way from beginning to end.

TABLE OF CONTENTS

	<u>Page</u>
1. Introduction.....	1
1.2 Background on microchannel heat exchangers.....	7
1.1 Objectives.....	9
2. Lab-scale Receiver Design and Fabrication.....	12
2.1 Material Selection.....	12
2.2 Lab Scale Receiver Design.....	14
2.3 Lab Scale Receiver Fabrication.....	19
2.3.1 LSR Fabrication.....	19
2.3.2 Nickel Plating and Diffusion Bonding.....	25
2.3.3 Absorber Coating Application.....	27
3. Test Facility.....	30
3.1 Pressure and Temperature Test Facility.....	30
3.2 Thermal Fluidic Test Facility.....	31
3.2.1 High Flux Solar Concentrator.....	32
3.2.2 Supercritical CO ₂ Test Loop.....	36
3.3 Pressure Drop Test Facility.....	39
4. Lab-scale Receiver- Data Analysis, & Results.....	41
4.1 Integrity test.....	41
4.2 Definitions of Receiver and Thermal Efficiency for Experiments.....	42
4.3 Reflectivity.....	43

TABLE OF CONTENTS (Continued)

	<u>Page</u>
4.4 Incident Heat Flux.....	45
4.5 Results.....	48
4.5.1 Pressure drop.....	48
4.5.2 Thermal efficiency tests.....	49
4.6 Heat Loss.....	53
4.7 Uncertainty Analysis.....	56
5. Integrated Receiver - 8cm x 8cm Test Article.....	58
5.1 Structural Design.....	58
5.2 Design Revision.....	71
5.3 Integrity Testing.....	80
6. Conclusion.....	90
7. References.....	91
8. Appendix.....	95
8.1 In Depth Coating Study – Pyromark 2500.....	95
8.2 Detailed Pressure Testing Procedure.....	102

LIST OF FIGURES

<u>Figure</u>	<u>Page</u>
1a. Central receiver diagram	1
1b. Parabolic trough receiver diagram	1
2. Solar Two central tower 10 MW power plant, Barstow, California	2
3. (a) Theoretical limit for receiver efficiency as a function of receiver temperature. (b) Theoretical limit for combined receiver and Carnot solar plant efficiencies as a function of receiver temperature. The red line indicates the increase in efficiency in going from an incident heat flux of 30 W/cm ² (C= 300) to 100 W/cm ² (C=1000) using the proposed microchannel receivers	5
4. High level flow chart for visualizing design process	10
5. Pictures of the LSR 1, (a) welded microchannel receivers, (b) side view of the microchannel section and plena, (c) assembled view of the plena and microchannel sections prior to welding, and (d) reference scale for the sections.....	20
6a. LSR 2, parallel channels, exploded view with layer indication	21
6b. LSR 2, parallel channels, wire frame model with flow path indicators	21
7. Exaggerated Ansys model of layer 1 failure	22
8. Completed LSR 2 Lamina	23
9a. LSR 3, pin array, exploded view with layer indication	24
9b. LSR 3, pin array, wire frame model with flow path indicators	24
10. Completed LSR 3 lamina	24
11a. Surface profile of LSR 2, showing 6μm of relative surface roughness	26
11b. Surface profile of LSR 3, showing 6μm of relative surface roughness	26
12. Diffusion bonded LSR 2 and LSR 3 test articles	27

LIST OF FIGURES (Continued)

<u>Figure</u>	<u>Page</u>
13. Measured spectral reflectivity values compared with the data provided by the Tempil	28
14a. LSR 2 coated with Pyromark 2500 prior to testing	29
14b. Pyromark 2500 after low flux testing	29
14c. Pyromark 2500 after high flux testing	29
15. Surface finish progression from the lapping process performed on LSR 3	29
16. Pressure and Temperature testing facility (a) schematic, (b) picture of test chamber	31
17. Simulation of the reflector using TracePro ® (a) reflector geometry, predicted flux map for 100 W/cm ² achieved at a distance of ~65 mm downstream of the second focal point (b), and 400 W/cm ² achieved at a distance of ~25 mm downstream of the second focal point (c).....	33
18. High flux concentrator facility. Key components include the lamp power supply and igniter (a), a parabolic reflector (b), and cooling system for the cathode.....	35
19. Supercritical carbon dioxide test loop schematic incorporated with the high flux solar concentrator	36
20. Supercritical carbon dioxide facility with each major component labeled.....	38
21. Modified sCO ₂ test loop with added differential pressure transducer	40
22a. Parallel channel integrity test at operating temperature and pressures	41
22b. Pin array integrity test at operating temperature and pressures	41
23a. Test article channel area after testing without absorber coating	44
23b. Test sample without absorber coating after burn in cycle to match channel area .	44

LIST OF FIGURES (Continued)

<u>Figure</u>	<u>Page</u>
24. Reflectivity of the bare Haynes surface compared to Pyromark paint	44
25. Spectral dependence of reflectivity and lamp irradiation	45
26. (a) Heat flux gage mounted to water cooled plate along with the insulated test article (b) Custom heat flux meter used to confirm incident heat flux data collected using Vatell heat flux meter	46
27a. Incident flux map of $\sim 100 \text{ W/cm}^2$ over 3 cm diameter.....	47
27b. Incident flux map of $\sim 350 \text{ W/cm}^2$ over 1cm diameter	47
28. Experimental pin fin array pressure drop	49
29. Receiver and thermal efficiency with variation of incident flux at a fixed exit temperature of $\sim 650^\circ\text{C}$. Also plotted is the average surface temperature of the device	51
30. Receiver and thermal efficiency variation with exit temperature at a fixed incident flux of 68.1 W/cm^2 for the parallel channel and 72.95 W/cm^2 for the pin array	52
31. Schematic of the facility for in-situ heat loss calibration. The entire LSR was insulated and no concentrated flux was applied	55
32. Heat loss calibration curve for the LSRs	55
33. Receiver and thermal efficiency with variation of incident flux at a fixed exit temperature of approximately 650°C with the inclusion of heat loss	56
34a. Unit cells in scaled up test article	59
34b. Inlet and outlet slots for each unit cell	59
35. Illustration of the test section header (a) Inflow plenum. (b) Outflow plenum, and (c) The channels which distribute or collect fluid from each unit cell	60

LIST OF FIGURES (Continued)

<u>Figure</u>	<u>Page</u>
36. Cutaway schematic of a simulated plenum region and a pin fin microchannel region	61
37. (a-c) Comparison of stress contours for wall thicknesses of 1, 2, and 3 mm; (d) Stress distribution comparison for the three wall thicknesses along path 2 in Fig. 36 (d).....	63
38. (a-b) Exploded views of the test sections sent out for fabrication. (c) Top view of the assembly showing the plenum section of the test article indicating the larger support pin structures that are widely spaced. (d) Bottom view of the assembly showing the microscale pin fin section with smaller pins that are closely spaced.....	64
39. Front view of the mid layer in the test sections sent out for fabrication	65
40. Schematic of designed pressure testing facility	66
41. Pressure testing of SS test articles depicted in (a), (b), (c). Figure 39d shows pictures of the test articles upon completion of testing	67
42. Sectioning and optical measurements of test sections upon completion of pressure testing	68
43. (a-b) Exploded views of the new concept for 8x8 cm ² test article. (c) Top view of the flux receiver plate with guiding arrows which shows the flow direction across the microscale pins. (d) Top view of the headering section with blue arrows showing the inflow in distributor channels and red arrows showing outflow in collector channels	72
44. Fluid passage in a concept with 2 unit cells with a micro gap as simplified receiver plate.....	73
45. (a) The side distributor header modelled with Ansys Mechanical (b) Von-Mises equivalent stress distribution in the model with 200 bar internal pressure and atmosphere outside pressure	74

LIST OF FIGURES (Continued)

<u>Figure</u>	<u>Page</u>
46. (a) Simulated fluid passage model in Fluent as a section of a unit cell (b) Pressure contour maps in the simulated model for SCO_2 working with required mass flow rate to dissipate 100 W/cm^2 incidental heat flux	75
47. (a and b) Exploded view of the finalized design from top and bottom (c) The laminates of the fabricated test section	76
48. Surface profilometry from the receiver plate showing the pitch distance between two adjacent pin fins	76
49. Diffusion bonded $8 \times 8 \text{ cm}^2$ test section showing apparent registration of pin features. Welds on the edges are from attempts to seal the bond seams after discovery of leaks	77
50. Exploded view of the modified design sent out for fabrication a) from top and b) from bottom with a zoom in showing the difference in the height of pin fins' base and edges on the receiver plate.....	79
51. (a) Revised design after fabrication stack and offset to view layers, (b) Flipped-revised design after fabrication stack and offset to view layers, (c) Aligned stack, (d) Post bond stack, (e) Detail view of bond interface, (f) Final IR design with inlet/outlet tubes weld in place	80
52. Schematic of assembled pressure testing facility	81
53. Schematic of assembled temperature and pressure testing facility	81
54. Results of the IR test article pressure test	82
55. Two views of the insulation setup for the IR pressure test at temperature	82
56. Static pressure testing at temperature of the IR test article	83
57. IR test article after structural verification testing.....	83
58. Pressure testing after top plate has been machined down to approximately $500 \mu\text{m}$	84

LIST OF FIGURES (Continued)

<u>Figure</u>	<u>Page</u>
59. Pressure testing at high temperature after top plate has been machined down to approximately 500 μ m	84
60. Test article surface condition after structural testing. Notice discoloration, but no visible signs of deformation.....	85
61. Pyromark 2500 Coating applied prior to IR imaging and data collection	85
62. Schematic of infrared imaging facility	86
63. (a) Test article header orientation (b) exploded view of the lamina in reference to the infrared camera viewing direction	87
64. Location of thermocouple for room temperature calibration	87
65. Room temperature IR camera calibration.....	88
66a. Infrared image of the 100°C flow test.....	88
66b. Plot of the data lifted from the 100°C infrared image	88
67a. Infrared image of the 250°C flow test	89
67b. Plot of the data lifted from the 250°C infrared image	89

LIST OF TABLES

<u>Table</u>	<u>Page</u>
1. Material selection list.....	13
2. Numerical design summarization and keynotes.....	18
3. Experimental device list.....	39
4. Results of custom heat flux meter used to confirm incident heat flux data collected using Vatell heat flux meter	47
5. Representative measurement uncertainty estimate.....	57
6. Optical profilometry and bulk strain measurements	70
7. Temperature point measurement from infrared image calibration.....	87

NOMENCLATURE

ROMAN

C	concentration ratio, Carnot cycle
E_{Lamp}	energy of Xe lamp (rel. units)
$E_{\lambda,Lamp}$	wave length dependent energy of Xe lamp (rel.units/nm)
h_{in}	enthalpy in of the fluid (J/kg)
h_{out}	enthalpy out of the fluid (J/kg)
I	solar insolation (MJ/m ²)
k	thermal conductivity (W/m.K)
\dot{m}_{sCO_2}	mass flow rate of sCO ₂ (g/s)
P	absolute pressure (bar)
ΔP	measured pressure drop (bar)
$q_{conv.}$	convective energy (W)
q_{fluid}	energy in the working fluid (W)
q_{in}	energy into receiver (W)
q_{abs}	energy absorbed by receiver (W)
$q_{incident}$	incident solar energy (W)
q_{loss}	heat loss (W)
q_{re-rad}	re-radiated energy(W)
q''_{inc}	incident heat flux (W/cm ²)
Re	Reynolds number
Re_{DH}	Reynolds number based on hydraulic diameter
Re_{Dp}	Reynolds number based on pin diameter
t	time (min)
T_H	heat addition temperature (C)
T_C	heat rejection temperature (C)
T_s	microchannel surface temperature (C)
$T_{body,ave}$	average microchannel body temperature (C)
V	gas velocity in pinfin array (m/s)

NOMENCLATURE (Continued)

GREEK

α	absorptivity
ϵ	emissivity
σ	Stephan-Boltzmann constant ($\text{W}/\text{m}^2 \cdot \text{K}^4$)
η	efficiency
η_{th}	theoretical efficiency
η_{rec}	solar receiver efficiency
λ	Wavelength (nm)
ρ	reflectance
$\rho_{effective}$	effective reflectance
$\rho_{\lambda, Haynes}$	wavelength dependent reflectance of Haynes 230

SUBSCRIPTS

<i>Carnot</i>	Carnot cycle
<i>ch</i>	parallel microchannel
D_h	hydraulic diameter of pin fin array
<i>exp</i>	experimental value
Loss	estimated heat loss
<i>net</i>	total energy
Pin	pin fin array
<i>rec</i>	solar receiver
<i>s</i>	device surface
<i>sCO₂</i>	super-critical carbon dioxide
<i>th</i>	theoretical efficiency

Experimental Characterization of a Supercritical Carbon Dioxide Microchannel Solar Thermal Receiver

1. Introduction

Electric power from solar energy is harnessed typically in two ways- by using photovoltaic cells or by concentrating solar energy thermally to run a traditional power generation cycle. The focus of this thesis is on concentrated solar thermal technology wherein solar energy is concentrated through the use of mirrors onto a receiver. The receiver contains a working fluid that absorbs this concentrated energy and transfers it to a power block. Two major methodologies are used to accomplish concentration. First is by using a large field of mirrors, also known as heliostats, to focus the sun's energy to a central (power) tower, Fig. 1a. The second is by using a parabolic trough to focus the energy to a single line of tubing, Fig. 1b. Thermal power plants that operate at high temperatures, greater than 400°C , rely on the power tower design.

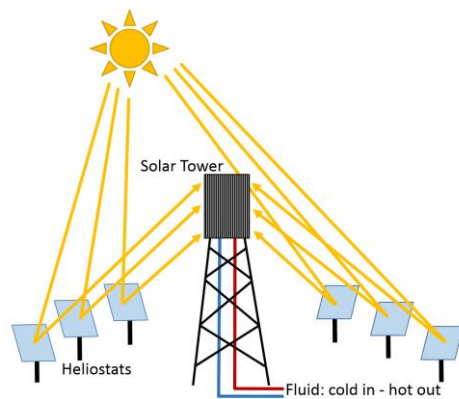


Figure 1a. Central receiver diagram

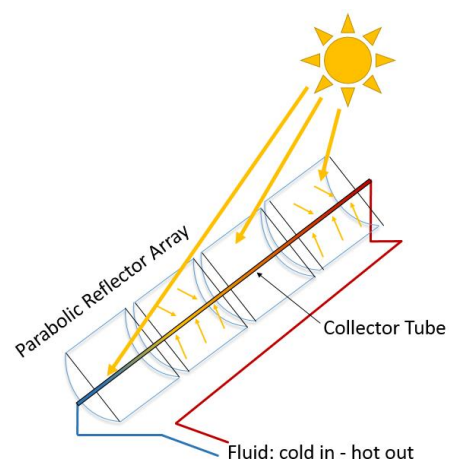


Figure 1b. Parabolic trough receiver diagram

In a typical power tower plant, the working fluid that is heated in the receiver exchanges heat with water in a secondary heat exchanger. The most common working fluid in the receiver (primary) loop is solar salt, a mixture of sodium and potassium nitrate. The steam generated in the heat exchanger of the secondary loop goes through the Rankine cycle power block. The current status of molten salt technology, as represented by the Solar Two molten salt power plant, Fig. 2, was assessed by Pacheco [1].



Figure 2. Solar Two central tower 10 MW power plant, Barstow, California [2]

The Solar Two receiver produced 565°C molten salt with a receiver efficiency of 88 percent at an average incident flux of 43 W/cm². The efficiency included a 95 percent absorptivity (5% reflection losses) achieved through application of a high temperature paint, Pyromark 2500. In a more recent assessment, Kolb [3] estimates that while

current state-of-the-art technology might operate with an incident flux on the order of 80 W/cm^2 , next generation high temperature molten salt power towers could operate at incident fluxes of around 100 W/cm^2 with a corresponding receiver efficiency of 89 percent, including reflection losses based on an absorptivity of 95 percent. There has been recent discussion and research on the use of supercritical carbon dioxide (sCO_2) as the working fluid of solar thermal plants as it lends to small power generation units and plant size. Advantages of using sCO_2 include smaller power block size, higher cycle efficiency owing to potential for higher exit temperatures in the receiver, and potential simplicity in power plant controls. The Department of Energy's Sunshot office has set target of 90% or greater receiver efficiency at exit fluid temperatures of 650°C or greater for such sCO_2 solar thermal receivers. In addition to the increased requirement for efficiency over molten salt plants, the high exit fluid temperature places a stringent requirement on the thermofluidic design of the receiver since radiation and convective losses increase with temperature. Moreover, from a structural standpoint, the receiver has to be able to withstand temperatures of about 750°C and pressures of about 200 bar. Limited open literature exists on sCO_2 solar receivers. Published project summaries and presentations at Department of Energy's Sunshot Annual Reviews indicate that the Sunshot program is funding the development of alternative different sCO_2 receiver concepts [4]. Brayton Energy has developed two designs; one operating at 750°C that uses a cavity and low-cost cover glass to reduce thermal losses [4] and a second open receiver design for which predicted receiver efficiency or incident flux on the receiver surfaces has not yet been reported in open literature. National Renewable Energy Laboratory (NREL) is also developing a sCO_2 receiver, but details of the

design, incident flux or performance are not publically available. Typical gas-cooled central receivers had incident fluxes of 20 to 30 W/cm² [5].

Before considering specific designs of receivers, some ideal limits are considered. As is well known, the Carnot efficiency increases with increase in temperature of the receiver (heat addition side of the cycle) for a fixed low temperature (heat rejection side temperature), Eq. [1]

$$\eta_{th} = 1 - \frac{T_C}{T_H} \quad [1]$$

where T_H is the hot side fluid temperature and T_C is the heat rejection temperature. However, with an increase in T_H , the re-radiation loss increases as the fourth power. Assuming a 100 percent absorptivity of solar irradiation onto the receiver, an emissivity of unity, and no convection losses solar receiver efficiency can be written as Eq. [2]

$$\eta_{rec} = \frac{q_{fluid}}{q_{incident}} = \frac{q_{incident} - q_{re-radiation}}{q_{incident}} = 1 - \frac{\sigma \epsilon (T_H^4 - T_C^4)}{IC} \quad [2]$$

where I is the solar insolation and C is the concentration ratio. A concentration ratio of unity would imply solar insolation without any concentration. This value is nominally about 1000 W/m² (0.1 W/cm²) in the southwestern United States in summer months. Combining Eqs. 1 and 2, the Carnot solar cycle efficiency can be expressed as Eq. [3]

$$\eta_{rec,Carnot} = \left\{ 1 - \frac{T_C}{T_H} \right\} \left[1 - \frac{\sigma \epsilon (T_H^4 - T_C^4)}{IC} \right] \quad [3]$$

Figure 3 shows a plot of the receiver efficiency (Eq. 2, Fig. 3a) and the Carnot solar cycle efficiency (Eq. 3, Fig. 3b) as a function of hot side temperature T_H for various concentration ratios and an assumed solar insolation of 1000 W/m^2 . A $C=1000$ would therefore correspond to an incident flux of 100 W/cm^2 on the receiver. As can be seen from Fig. 3a, at a T_H of 923 K (650°C), the receiver efficiency increases from 85 percent to 95 percent with an increase in flux from 30 W/cm^2 to 100 W/cm^2 . The increase in efficiency at a fixed T_H is to be expected since the re-radiation losses are dictated by T_H . The corresponding Carnot solar cycle efficiency, Fig. 3b, increases from 57 percent to 64 percent with an increase in incident flux on the receiver from 30 W/cm^2 to 100 W/cm^2 .

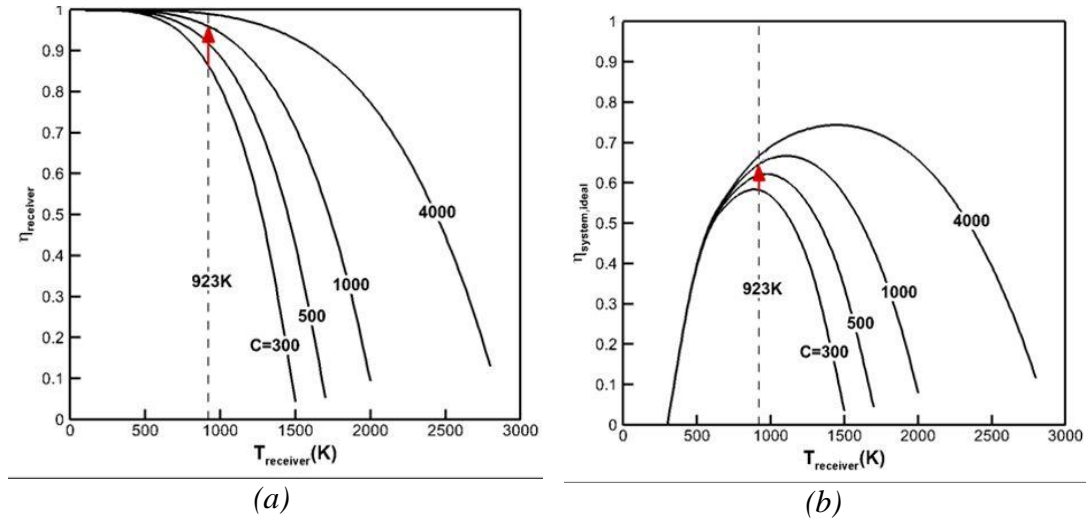


Figure 3. (a) Theoretical limit for receiver efficiency as a function of receiver temperature. (b) Theoretical limit for combined receiver and Carnot solar plant efficiencies as a function of receiver temperature. The red line indicates the increase in efficiency in going from an incident heat flux of 30 W/cm^2 ($C=300$) to 100 W/cm^2 ($C=1000$) using the proposed microchannel receivers

The above discussion related to the Carnot solar cycle efficiency suggests that high thermal efficiencies can be achieved if one were able to design a receiver that could absorb higher fluxes at the same temperature. One such design could be through the

use of microscale flow passages within the receiver. By reducing the diffusion length for thermal transport, microchannels permit increased flux of incident solar energy at the same fixed surface temperature of the solar receiver.

Heat transfer is a diffusion limited process, meaning that the heat transfer from the channel wall to the fluid is the limiting factor in determining the rate. Therefore the time required for the fluid and channel wall to reach an equilibrium temperature will decrease as a square to the diffusion length. Hence the residence time for equilibrium is dependent on the channels cross sectional geometry. In general if the channel cross section is reduced then the residence time will decrease and the required channel length will shrink, thus reducing the overall size of the device. This reduction in size can save cost in material, space, and in some cases manufacturing. Furthermore the decreased diffusion length allows for high rates of heat transfer and the ability to absorb high heat fluxes allowing for a broad range of applications. For solar thermal energy production the development of a high flux microchannel receiver has the potential to dramatically reduce the size and cost of a solar receiver. The size reduction can result in the reduction of re-radiation and convective losses and the high rate of heat transfer can allow an increase in incident flux without a large increase in surface temperature thus increasing the overall efficiency. The use of microchannel receiver architecture for sCO_2 solar thermal cycles is explored in this thesis. In order to assess the effectiveness of microchannel use in a solar thermal application lab scale receivers (LSR) were designed and fabricated for thermal performance characterization.

1.2 Background on microchannel heat exchangers

Tuckerman and Pease [6] demonstrated how microchannels utilizing water are able to remove heat fluxes as high as 790 W/cm^2 . Their work propelled further research into the field of microchannel technology. When large scale channels, or macro channels, can be redesigned into the form of several parallel microchannels, higher heat transfer rates at the same fluid flow rates can be achieved. This is accomplished in microchannels by the increase of the ratio of channel surface area to fluid volume within the channel. The small geometry of microchannels along with increased heat transfer rates allows for an overall reduction in device size compared to conventional devices and yet maintain the same thermal performance. However, the reduction in channel size will impose a higher pressure drop. This can be overcome by connecting several parallel channels through unique heading schemes [7], diverging and converging channel walls [8], or fractal like branching channel designs [9].

Microchannel technology has been applied to a wide range of applications including catalytic combustors [10-11], electronics cooling [12], chemical reactors [13], and compact heat and mass exchangers [14]. Single phase flows utilizing water or refrigerants have the ability to remove moderate heat fluxes up to about 200 W/cm^2 . High heat fluxes around 1000 W/cm^2 can be managed through the use of liquid metals. Phase change heat transfer applied in microchannel devices has led to the miniaturization of condensers and evaporators [15].

Since this study's interest is in the use of high temperature and pressure microchannel devices, the review indicated that typically a nickel super alloy is used in the construction of the device. Some noted materials for this application were nickel alloy 617, 800H, 230 (Haynes 230) and HX; of which nickel alloy 617 had the most favorable properties for high temperature applications (above 800°C). Common forms of manufacturing microchannel heat exchanger is through chemical etching and diffusion bonding. Mylavarapua et al. [16] constructed a heat exchanger using these methods and tested at a sustained temperature of 823°C and pressure of 2.7 MPa. To test the durability of the device creep tests were performed. These were completed over 1461 hours at temperature of 650°C and 3.5 MPa pressure resulting in a final creep of 0.02%. In the construction of the device a pure Ni interlayer of approximately 2.5µm thickness between the bonding surfaces was applied. It was reported the layer compromised the bond strength. High strength bonds, near native material strength, was reported by Li et al. [17] without the use of interlayers. The heat exchanger devices Li et al. (2008) studied were actually produced by Heatric. Heatric has commercialized the fabrication concepts of diffusion bonding multiple layers of chemically etched microchannel structures. Li et al. [18] also fabricated a supercritical carbon dioxide reactor using nickel alloy 617 and tested at 950°C and above 7 MPa, successfully.

Reviewing microchannel manufacturing studies suggested that microchannel heat exchangers could reach the cost of conventional heat exchanger based on volume production [19-21]. Several other studies have investigated solar applications of small channel [22-23] and microchannels devices [24-26]. A large focus has been on the use

of microstructures in the use chemical processing and solar powered hydrocarbon fuel reformation.

In conclusion it has been found that microchannels in the application of heat exchangers have the ability to remove high heat fluxes with the use of fluids. Refractory metals, such as nickel super alloys, have been used in the successful fabrication of micro-devices. Companies have commercialized the fabrication methods and use of microchannel devices in both chemical and heat transfer applications to create a cost effective product.

1.1 Objectives

The overall objective of this study was to experimentally characterize the performance of microscale solar thermal receivers that utilize supercritical CO₂ as the working fluid. The targets of the receiver performance were based on DOE's Sunshot Concentrating Solar goals: the fluid should have an exit temperature of at least 650°C, and the receiver thermal efficiency (excluding reflection losses) should be in excess of 90 percent. The goal of the study is to explain the development, fabrication, and demonstration of the performance of receivers based on lab-scale experiments. In order to do this Lab-scale Receivers (LSR) with an absorber area of 2x2 cm² were developed. With the successful demonstration of a LSR design, it was to be scaled up to an 8x8 cm² absorber area Integrated Receiver (IR) to verify scalability of concept.

The development of LSRs was an iterative process between CFD simulations, structural analysis, material selection and fabrication methods and constraints. Based on the operating parameters set by DOE's Sunshot Concentrating Solar goals of demonstrating an absorbed flux of 100 W/cm^2 at a receiver thermal efficiency in excess of 90 percent operating at 120 bar pressure and an exit fluid temperature of 650°C , simulation results were required to have 90 percent or greater thermal efficiency with a pressure drop less than 0.3 bar. Based on simulation results designs could be refined, but based on the operational goals of 120 bar and 650°C fluid exit temperatures, structural analysis in turn placed limits on the microchannel design. Alongside the fluid dynamics and structural analysis, fabrication and material choices would place constraints on the both the fluid paths and structural design. Below a simple flow chart is provided to visualize the parallel and iterative design processes, Fig. 4.

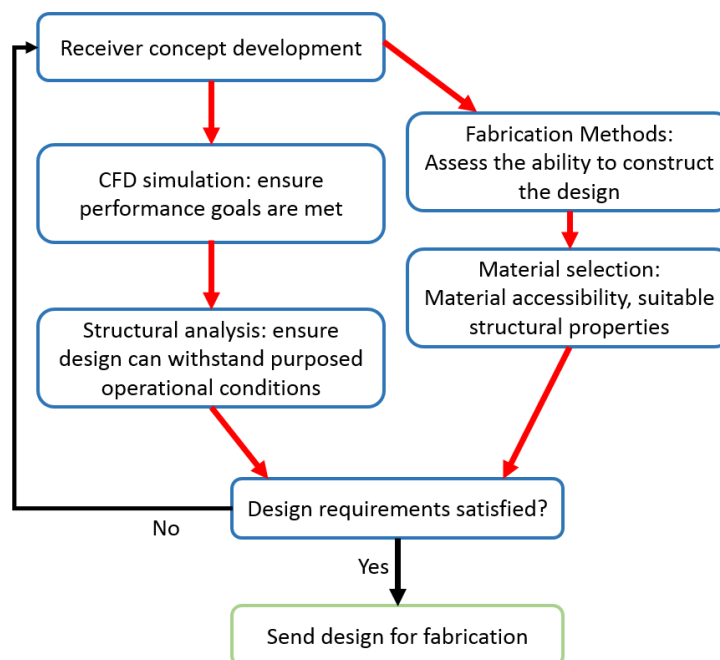


Figure 4. High level flow chart for visualizing design process

Given the limited information available in open literature on the design as well as the integrity and performance of high temp HXs, the objectives of the work were as follows:

- i. By working iteratively with CFD analysis [27], identify options for fabrication of microchannel sCO₂ receivers
- ii. By working with various vendors, develop the fabrication methods for the lab-scale receivers
- iii. Characterize the mechanical integrity of the receivers through static pressure tests at operating temperature
- iv. Characterize the thermofluidic performance through global measures of efficiency and pressure drop

2. Lab-scale Receiver Design and Fabrication

In this chapter, the process adopted in the design of the lab-scale receivers (LSRs) as well as the material selection and fabrication process steps will be discussed. All three aspects- materials selection, design, and fabrication are closely intertwined with the latter two aspects playing a major role in constraining the design.

Fabrication includes the material selection, laminae patterning, plating, diffusion bonding, and absorber coating. Design of the receiver was completed through the use of numerical modeling based on desired operation conditions and efficiency goals. For a complete study of the computational design, the reader is referred to a companion study [27].

2.1 Material Selection

A key driver in the manufacturing process of the LSR was based on material selection. The chosen material had to maintain a high strength at elevated temperatures. A list of available materials was generated based on vendor published data sheets of refractory materials. The results of this review are summarized in Table 1 below.

Table 1 – Material selection list

Vendor	Alloy Name	T _m [C]	Composition for bonding*	Thermal Conductivity [W/m-K] @ 700°C	Rupture Stress @ 100hr [Mpa]	Temperature for rupture stress @ 100hr [C]	Material thickness affected by oxidation after 1000hr @ 980°C [μm]
Specialty Metals	Inconel 800H & HT	1360	23%	22.8	-	-	312
Specialty Metals	Inconel X750	1400	17%	22.2	241**	730	-
Specialty Metals	Inconel 751	1400	17%	-	352	732	-
Specialty Metals	Inconel 718	1270	21%	23.1	-	-	-
Specialty Metals	Nimonic 80A	1330	21%	22.3	305**	750	-
Haynes	230	1350	36.02%	22.4	185	760	20
Haynes	214	1370	16%	26.9	235	760	5
Haynes	25	1365	35%	22.6	250	730	211
Haynes	R41	1325	19%	22	-	-	-
Haynes	Waspalov	1340	19%	20.9	365	760	-

*Must have a % composition sum of Cr, W, and La that is <35-40% to be chemically etched

** Approximated from Fatigue Chart

Initial focus was on developing a design that used chemically etched micro pins in place of microchannels. Originally Haynes 214 was selected based on its ability to be chemically etched, good rupture strength at high temperature, and resistance to oxidation. The plan was to fabricate the test articles out of Haynes 214 and a vendor was identified that could perform the etching and bonding of this material. Unfortunately, the material could not be obtained at a reasonable cost in smaller quantities needed for the project.

Materials within the above list were then reconsidered. Based on the project's tight schedule and limited funding, the timely availability of small quantities of material was the primary consideration for material selection. Inconel 800H&HT, Haynes 230, and Haynes 25 were widely available in small quantities but Inconel 800H&HT and Haynes 25 were rejected due to the high rate of oxidation. Consequently, the primary focus was on Haynes 230. The challenge with Haynes 230 was the difficulty of chemical etching

and lower rupture stress compared with Haynes 214 at comparable temperatures for the application. The inability to etch Haynes 230 is due to the high concentration of Chromium, Tungsten, and Lanthanum. The total concentration of these element should be less than 35-40 percent of the total material composition in order to chemically etch. Since the concentration in Haynes 230 is 36 percent a sample was sent out to test the ability to be chemically etched. Unfortunately it could not be and hence other methods of patterning such as micromachining or sinker EDM were sought. Further details of fab steps will be discussed in a later section in this chapter. The availability of a number of other refractory metals with superior properties to Haynes 230 suggests that the performance of the concept can be significantly improved, although, as noted above, the cost and availability of these materials prevented their use in this project.

2.2 Lab Scale Receiver Design

The design approach of the LSRs consisted of establishing the general layout of the test article (multiple cooling channels attached to one or more inlet and outlet headers), characterization of the performance through computational fluid dynamics (CFD) simulations, and model iteration to meet the performance targets. The goal was to demonstrate an absorbed flux of 100 W/cm^2 at a receiver thermal efficiency in excess of 90 percent and an exit fluid temperature of 650°C . Based on achieving a target absorbed flux of 100 W/cm^2 , the constraint on the LSR size to a $2 \times 2 \text{ cm}^2$ absorber area was based on the input electrical power requirements of the high flux concentrator. Development and construction of the testing facility is detailed in the following chapter.

CFD simulations were utilized to predict flow distribution followed by design modifications to attain the desired uniformity of flow and pressure drop. CFD simulations were also used to solve the conjugate problem to obtain thermal distribution within the solid and fluid. Computational fluid and thermal analysis has been carried out in three-dimensions using the commercial software ANSYS Fluent and are detailed in a separate thesis [27]. Most of the simulations involved complex configurations that combined Fluent's unstructured grid solver with grid generation software. Fluid properties for supercritical carbon-dioxide were taken directly from Engineering Equation Solver (EES). For estimation of properties, the pressure in the device was held constant at the operating pressure of 120 bar because the change in pressure through the device is assumed small. The fluid temperature was varied from 527 to 827°C. A polynomial curve-fit was computed for each fluid property of interest and used in the simulations.

Haynes 230 property data was manually extracted from plots on the datasheet available from Haynes [28]. Properties were tabulated as functions of temperature, except for density, which is assumed constant. A polynomial curve-fit was computed for each physical property of interest.

In the CFD models the thermal receiver efficiency was defined as the heat transferred to the fluid, divided by the heat absorbed on the receiver surface (not including reflection losses). Total receiver efficiency includes reflection losses from the receiver along with thermal losses. In simulations, the thermal boundary at the heated surface is one of specified constant heat flux, with no radiation or external convection modeled. This specified heat flux is the numerator to the efficiency equations. The denominator

is equal to the specified heat flux, plus an estimated heat flux loss due to incident radiation, natural convection, and re-radiation. The final form of the efficiency equation is

$$\eta = \frac{\alpha q''}{(q'' + h(T - T_{\infty}) + \epsilon \sigma (T^4 - T_{\infty}^4))} \quad [4]$$

where η is the surface efficiency, α is the absorptivity of the surface, ϵ is the emissivity of the surface, q'' is the specified heat flux absorbed by the fluid, h is the heat transfer coefficient for natural convection, T is the average surface temperature, T_{∞} is the ambient surface temperature (25°C), and σ is the Stefan-Boltzmann constant. The emissivity of the surface is determined by the coating used and for the simulations it is assumed that the absorptivity is equal to the emissivity. The coating to be used is Pyromark 2500, a high temperature paint, which has an advertised absorptivity of approximately 95 percent when averaged over 200-2600 nm range. Appendix 8.1 details the application process, testing and effectiveness of Pyromark.

Not only is the thermal performance of interest, the microchannel receivers need to be able to withstand high mechanical and thermally induced stresses. Given the non-traditional designs, for which there were no codes and standards for mechanical designs, it was imperative that mechanical and thermal stress models be developed. Finite element stress analysis was conducted using Ansys. Wherever appropriate, 2D models were first used because of their lower computational complexity. The lower complexity allowed higher resolution in high-stress regions. Based on the 2D models, and for selected designs, full 3D models were also investigated. The 3D models were

limited to about 3 million nodes by the available license. To increase accuracy in certain 3D models, small high stress regions of the model were refined while applying a very coarse grid to the rest of the model.

For stress analysis, mechanical properties for Haynes 230 were again taken from the data sheet available from Haynes [28]. A constant value was used at an appropriate temperature, generally being the average temperature of the metal in the region being modeled. In order to evaluate stress analysis results and determine a factor of safety, creep strength was used. The benchmark used was 185 MPa, the 10-hour rupture strength at 790°C (1063 K). This temperature is based on the maximum temperature observed in the solid in the areas of highest stress for the various designs.

In order to avoid stress singularities caused by sharp interior corners, a small radius of 25 microns was used as first estimate. Stress singularities and other anomalies can also result from poor choices of boundary conditions. Care was taken to constrain the models in a way that would accurately capture the device's behavior, yet avoid the use of external constraints. Geometries were made with internal cavities completely enclosed and in situations where symmetry planes were used in the geometry frictionless supports were used as constraints. All supports and constraints were applied well away from areas of interest to reduce and prevent any unrealistic behavior.

Upon completion of the numerical analysis and design, three general models were finalized. Each of these designs were categorized based on manufacturing ease, scalability and flow distribution. LSR 1 would be the simplest design to fabricate and could be fabricated in the shortest amount of time. The design would involve micromachining parallel circular microchannels by drilling and welding headers to the

channel section. This device would be difficult to scale to a larger receiver in terms of manufacturing techniques. LSR 2 would consist of an array of parallel microchannels and header plates that would direct fluid into and out of the array. The parallel microchannel array would be micro-machined and the plates would be diffusion bonded together to form the receiver. This design would be less difficult to scale. LSR 3 is similar to LSR 2 but the micro pin fin array would be formed by sinker EDM. In addition, a pin fin array would be investigated rather than a parallel microchannel array owing to the potential for better flow distribution in case of non-uniform fluxes. Similar to LSR 2, the microchannel plates and header plates would be diffusion bonded. Table 2, below, summarizes the key points from the design results.

Table 2 – Numerical design summarization and key notes

LSR	Manufacturing complexity	Stress	Flow Distribution	Pressure Drop	Scalability
1	Low	Stresses in the channels expected to be low (no sharp corners for high stress concentration); header design needs careful thought to minimize stresses	Can be uniform	Could be low if large aspect ratio channels are used	No
2	Medium	Stresses in channels expected to be low	Can be uniform	Could be low if large aspect ratio channels are used	Potentially, but more complex than LSR 3
3	High	Stresses could be high if pins are misaligned due to the large number of 90° corners	Can be uniform	Could have larger pressure drop due to pin packing	Yes

2.3 Lab Scale Receiver Fabrication

Fabrication of the LSRs was completed in the order of material selection, laminae fabrication, nickel plating, diffusion bonding, and absorber coating application. The following is the detailed discussion of each process step.

2.3.1 LSR Fabrication

The LSRs were manufactured in two ways. LSR 1 is machined using conventional methods and welded together. LSR 2 & 3 are manufactured in 3 major steps; patterning of laminae, nickel plating, and diffusion bonding. All of these design were tested to ensure structural safety, as outlined in chapter 4, prior to thermofluidic testing in the high flux concentrator setup.

The LSR 1 design, shown in Figs. 5 a-d, consists of three sections: two header sections and one channel section. The circular microchannels are machined by drilling through a 20 mm x 20 mm x 2 mm piece with the channels drilled such that the distance from the absorption face is only 500 μm , Fig. 5b. The header sections slide on to either end of the channel piece and are welded in place. The header sections each have a circular hole to which the inlet and outlet tubes are welded.

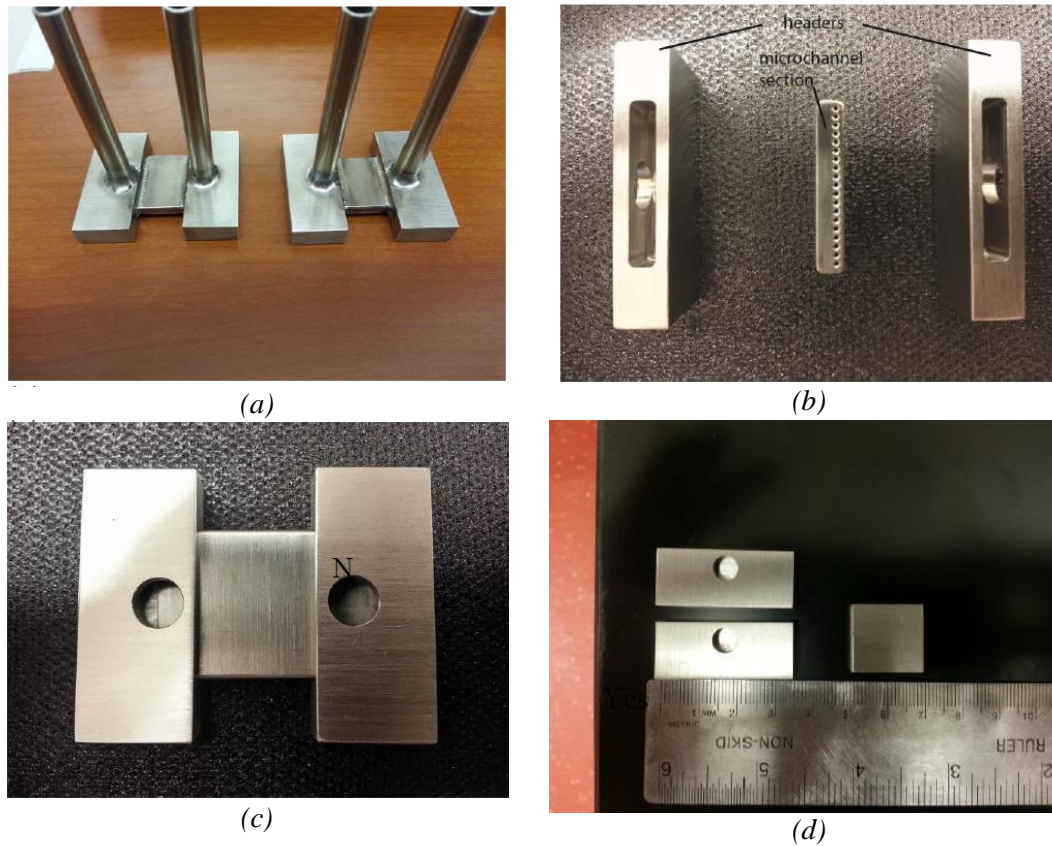


Figure 5. Pictures of the LSR 1, (a) welded microchannel receivers, (b) side view of the microchannel section and plena, (c) assembled view of the plena and microchannel sections prior to welding, and (d) reference scale for the sections

In the final design, the channels were 500 μm in diameter and spaced 500 μm apart. The distance from the centerline of the channel to the heated surface was 700 μm . The heated area was 1 cm by 2 cm. This configuration resulted in a designed pressure drop much lower than the maximum pressure drop constraint of 0.3 bar. However, due to the machining techniques used for this design (specifically drilling the channels), the length and diameter of the channels are limited. This LSR design was pursued since it was assumed to have the lowest risk of failure in term of manufacturing methods since it did not involve diffusion bonding. However, given the success in fabricating LSR 2 and 3, and the difficulty in scaling up an LSR 1 design, sCO₂ testing using this receiver

was deemed not necessary and this design will only be discussed further in structural testing, Appendix [8.2].

LSR 2 is constructed of three laminae. Each lamina was cut to 40 mm wide and 60 mm long, and the subsequent features were machined. The header plate was 6.25 mm thick and consisted of inlet and outlet openings for header tubes, similar to the LSR 1, layer 1 in Fig. 6a. On the underside, two header slots were machined for flow distribution. The second plate is 2 mm thick and consists of several slots machined using wire electrical discharge machining (EDM) that align with the header plate slots, layer 2 in Fig. 6a.

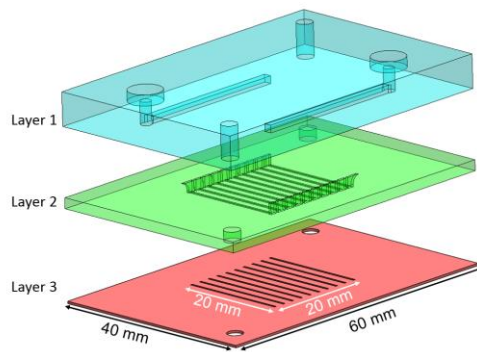


Figure 6a. LSR 2, parallel channels, exploded view with layer indication

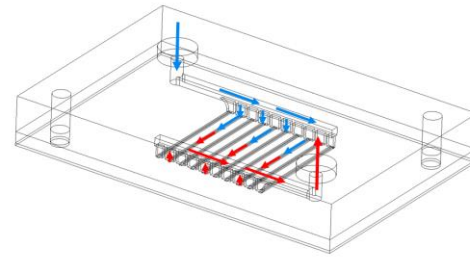


Figure 6b. LSR 2, parallel channels, wire frame model with flow path indicators

The slots on the middle plate form a series of reinforcing ribs. These ribs were implemented during a design iteration of the structural analysis in. The issue was discovered with the initial header concept. This header featured two relatively large dimensions the over 12-mm height and the 2-cm length that are necessary to deliver fluid to all of the channels that cover a 2-cm by 2-cm heated area. The resulting interior surfaces of the header lead to high force on the walls of the header, causing a structural

failure. Failure would occur in layer 3, where the thin plate is stretched by the force on the header walls. The exaggerated Ansys model is presented in Fig. 7. The solution to this problem was to divide the header into two regions: one in layer 2 and one in layer 3. In layer 2, the continuous slots are divided into nine separate slots, with ribs between the two walls of the header. The ribs remove the majority of the stress imparted in layer 1. Also, the height was reduced in order to reduce the force on the header walls. In the final design, the highest stress results in a safety factor of approximately 1.3.

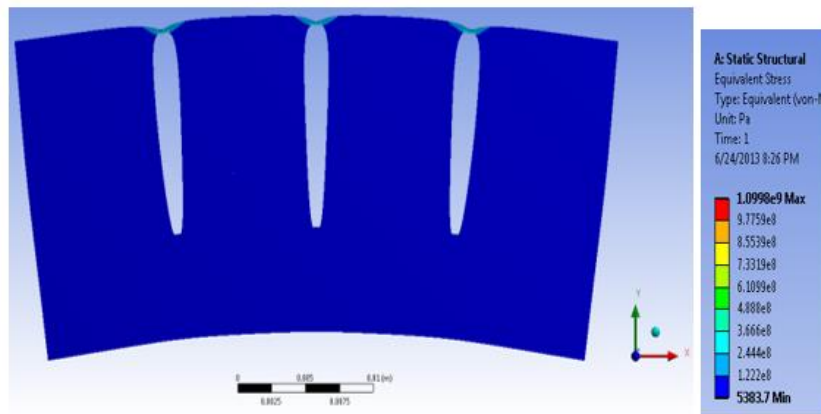


Figure 7. Exaggerated Ansys model of layer 1 failure

The underside of the plate had ten parallel 500 μm wide channels machined 130 μm deep, as seen in Fig 6a. The third and final plate was only 430 μm thick and ten matching channels machined into it, layer 3 in Fig. 6a. The thickness of the final plate is the bottleneck for heat transfer. Since the diffusion length is reduced greatly in a micro structure the conduction through the absorbing plate creates the highest resistance. Reducing the thickness increases the receiver's ability to maintain a low surface temperature by allowing the fluid to rapidly remove the imposed heat flux. A wire frame view of the assembled lamina stack with flow direction is shown in Fig. 6b. The two holes in opposite corners of the each sheet of the device are alignment holes

used for positive registration during diffusion bonding. The fabricated LSR 2 plates are shown in Fig. 8, below.

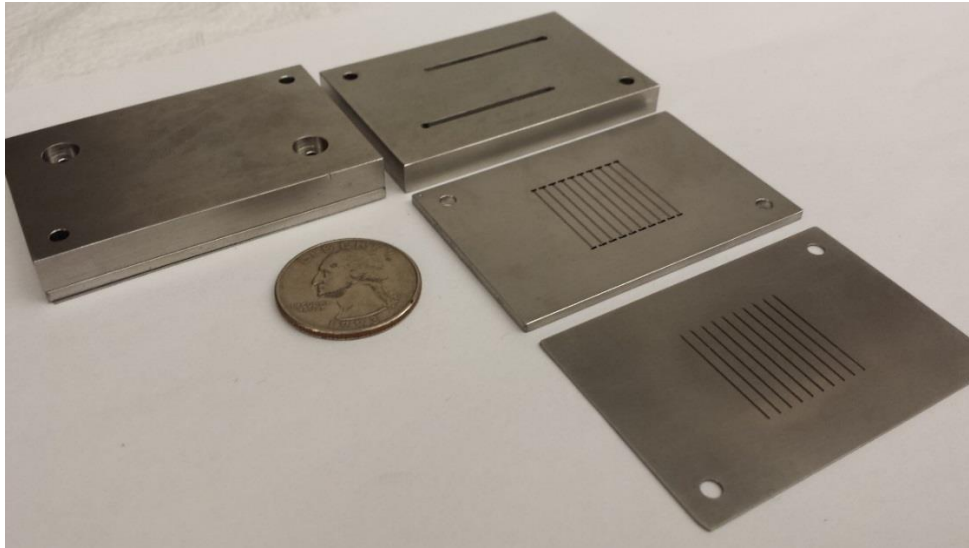


Figure 8. Completed LSR 2 Lamina

LSR 3 follows a similar make up of LSR 2, but instead of parallel channels the receiver section is made up a micro pin-fin array. Again the plates are cut to 40 mm by 60 mm out of the Haynes 230 stock and then the features are machined. In this design the header plate is 6.25 mm thick and has three header slots, layer 1 in Fig. 9a. Two exterior channels are connected by a horse shoe feature and make up the inlet header. The central slot is the single outlet header. This configuration effectively splits the overall 20 mm x 20 mm absorption area in to two 10 mm x 20 mm sections where the gas flowed from the outer edges inward. This entire plate was machined using conventional milling techniques. The mid plate is constructed in the same manner as LSR 2 with the exception of the channel side. The plate is still 2 mm thick and has several slots machined using wire EDM that align with the header plate slots, similar as in LSR 2.

In this plate there is an addition of a third set for the central outlet header. The parallel channels are replaced with sinker EDM formed micro pin fins measuring $700\ \mu\text{m}$ in diameter and $180\ \mu\text{m}$ tall, layer 2 in Fig. 9b. The final plate, flux absorber plate, was again $430\ \mu\text{m}$ as in LSR 2 and has matching pin features sinker EDM into it, layer 3 in Fig. 9a. A wireframe model is shown in Fig. 9b for flow path visualization. Figure 10 shows the final machined plates for LSR 3. Once the lamina for LSR 2 and 3 were fabricated they were sent for nickel plating.

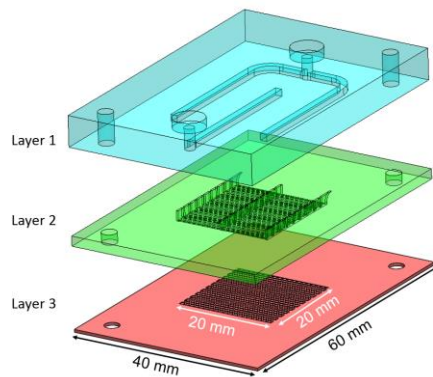


Figure 9a. LSR 3, pin array, exploded view with layer indication

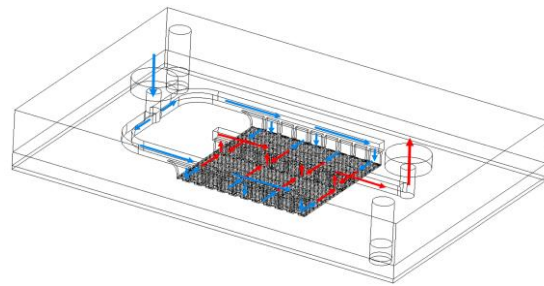


Figure 9b. LSR 3, pin array, wire frame model with flow path indicators

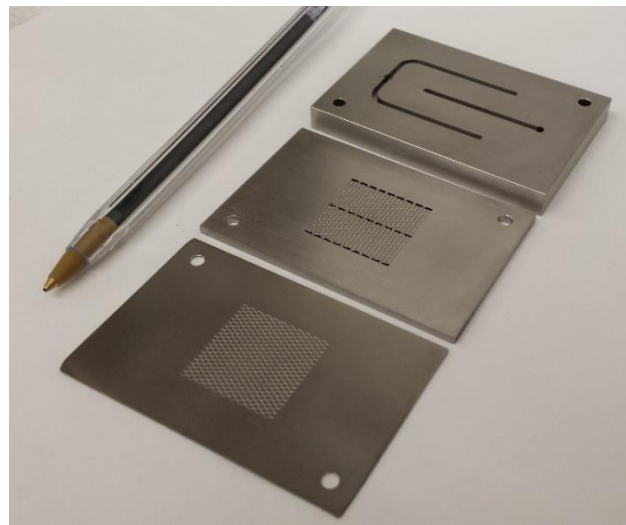


Figure 10. Completed LSR 3 lamina

2.3.2 Nickel Plating and Diffusion Bonding

Bonding was performed by an external vendor (Refrac Systems). Based on prior experience with bonding Nickel super alloys, they recommended nickel plating the laminae to industry specifications prior to bonding. All of the laminates needed to be flat and parallel to within 12.5 μm after plating with a plating thickness of 2-4 μm per side. Prior to plating, the surfaces should be aggressively reverse current etched to remove surface oxides. Nickel standard AMS2405 was used to plate the entire laminate. ASME2405 is an electro-less nickel plating process (ENP) that contains a small amount of phosphorus, <2 percent of bath volume. The ENP allows Liquid Interface Diffusion Bond (LID) to form. As strain is imparted and held the interfaces contact and diffusion occurs, but the interface material, ENP, will also diffuse into the parent metal. The phosphorus will either vaporize or react as nickel phosphides. This process generates a strong bond, but the NiP are brittle phases. These phases could present problems if the process is used for parts that undergo bending or forming processes.

Ideally, only the surfaces of the laminae that would be undergoing diffusion bonding would be plated to ensure that the channel dimensions would be unchanged. However, masking to expose only the bonding surfaces could potentially cause plating build up at masking interfaces. If the plating builds up at the corners or the edges, it could create regions of excess deposition that would result in leak paths if they cannot be pressed out during diffusion bonding.

For a diffusion bond to be accomplished the stack would have to undergo loading during a high temperature cycle. This loading will impart strain into the lamina stack. Based on Refrac's experience, a 2 percent (± 0.5 percent) bulk strain was imparted to the stacks. Adequate loading and subsequent strain was required to ensure that any surface imperfections that can be leak paths were eliminated. To further reduce this risk the lamina were precision ground to 6 μm relative surface roughness, R_y , Fig. 11 (a-b).

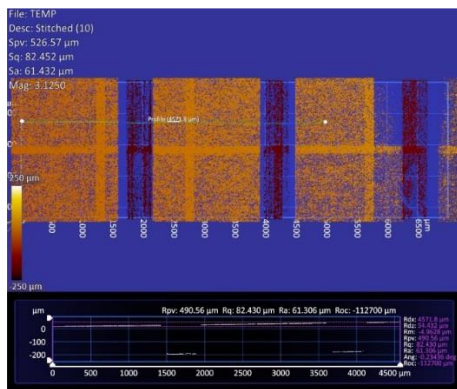


Figure 11a. Surface profile of LSR 2, showing 6 μm of relative surface roughness

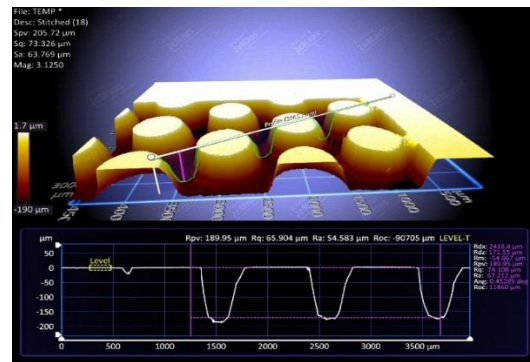


Figure 11b. Surface profile of LSR 3, showing 6 μm of relative surface roughness

The bonding process completed by Refrac was completed in hydrogen partial vacuum environment. The furnace operation is proprietary of Refrac systems and were performed in compliance of SAE-AMS-H-6875 Revision B. The compression load was applied at temperatures exceeding 1100°C for a duration that achieved a dial reading of 2.5 percent strain. Final measurements of the stack using a digital caliper indicated an imparted strain of approximately 1.5 percent. Figure 12 shows the diffusion bonded LSR 2 and 3.



Figure 12. Diffusion bonded LSR 2 and LSR 3 test articles

2.3.3 Absorber Coating Application

The LSRs were coated with Pyromark 2500 flat black paint. The manufacturer-recommended procedure was used to apply the paint. Upon application of a thin coat using a paintbrush, the coating was air-cured for 12 hours followed by furnace curing at 250°C. The temperature was then ramped to 540°C over a period of an hour to provide added resistance to thermal shock. The spectral reflectivity of the paint, coated on a sample Haynes 230 shim, was measured using a spectrophotometer (JASCO UV-670). The receiver itself could not be used for reflectivity measurements due to its larger size and the welded tubes at the back end. A sample was prepared with Pyromark 2500 and the reflectivity was measured as a function of wave length over the range of 400-2500 nm. Figure 13 shows a comparison of the measured spectral reflectivity values compared with those provided by the paint manufacturer, Tempil [31]. The coated shims had a reflectivity that was almost constant at 5 percent over a wavelength range of 600 – 1700 nm. While there was good agreement between the measured and manufacturer values in the range of 1000- 2000 nm, the measured reflectivity was

approximately 2-4 percent higher in the lower wavelengths (300-1000 nm). The average reflectivity over a wave-length range of 400-2500 nm was 5.3 percent for the Pyromark coating.

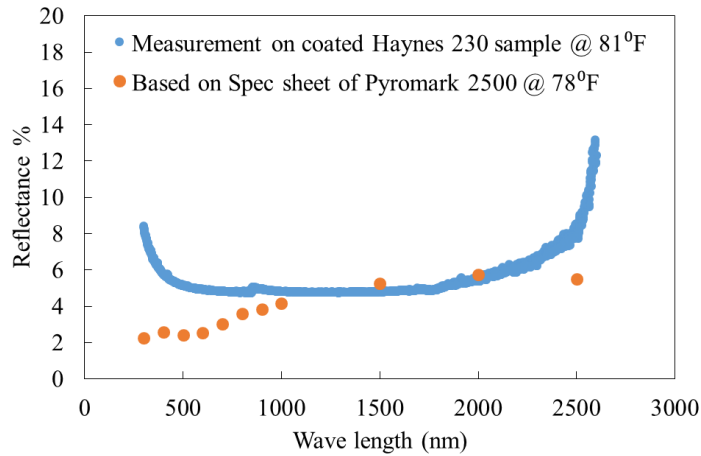


Figure 13. Measured spectral reflectivity values compared with the data provided by the Tempil

The Pyromark coating showed signs of progressively degrading during the course of experimentation. Figure 14 (a-c) shows images of the coating after curing and prior to an experiment, after the low heat flux experiments, approximately 50 W/cm² and 500-650°C fluid outlet temperatures, and after the 100 W/cm² and 650°C outlet test, respectively. Some degradation in coating can be observed after the low flux experiments and a substantial clear degradation in coating was observed at a 100 W/cm².

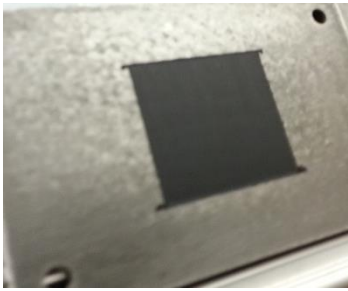


Figure 14a. LSR 2 coated with Pyromark 2500 prior to testing



Figure 14b. Pyromark 2500 after low flux testing



Figure 14c. Pyromark 2500 after high flux testing

To avoid further complications with coating degradation during testing, any further experiments were performed with no paint. The LSR surface was lapped down to bare Haynes 230, Fig. 15.

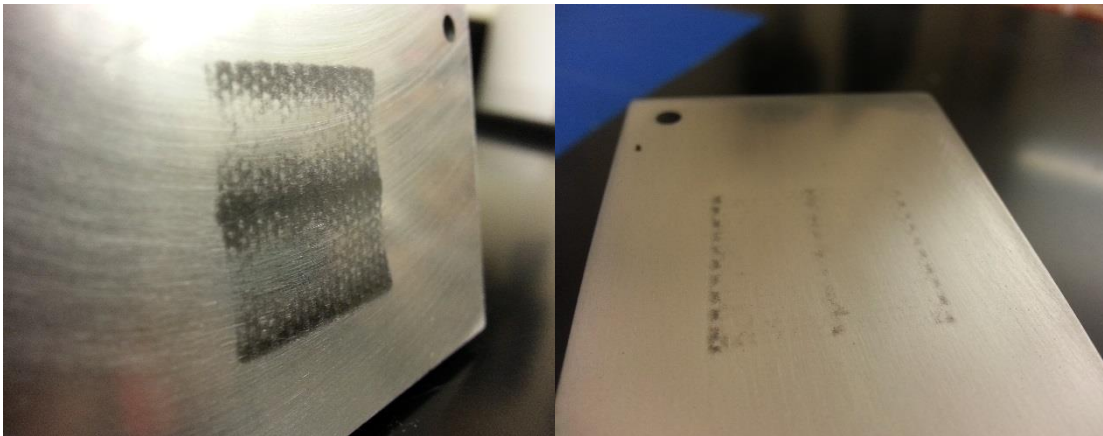


Figure 15. Surface finish progression from the lapping process performed on LSR 3

While the receiver efficiency was expected to be low for such experiments, with appropriate account for the surface reflectivity, the thermal efficiency of the receiver, could still meet the target of 90 percent or higher. These two measures of efficiency are defined in the Data Analysis section along with the discussion of reflectivity measurement.

3. Test Facility

This chapter reviews the main testing facilities used in the characterization of the developed test articles. The first facility was used for static pressure testing at temperature to characterize and ensure the structural robustness of the receiver designs. The second facility consisted of a complete test loop integrated under and automated high flux solar concentrator for the use in assessing the thermal performance of the receivers. The third and final facility was used to measure the pressure drop across the receiver.

3.1 Pressure and Temperature Test Facility

To ensure the structural robustness of each LSR, a pressure testing facility was designed and constructed. Figure 16a shows a schematic of the pressure and temperature test facility, while Fig. 16b shows a picture of the actual test enclosure. The enclosure is located within a sheet metal frame and inside a large vent hood. The LSR was located within the chamber using welded inlet and exit tubes as shown in Fig. 16a. A high pressure line from a nitrogen tank was connected to the inlet tube while the exit tube was connected to an Omega MMA2.5K absolute pressure transducer. A propane flame was used to heat the test section, and an Omega type K surface mount thermocouple located at the back face of the test section was used to record the surface temperature. Thermocouple and pressure transducer data were recorded using a National Instruments data acquisition system and LabView.

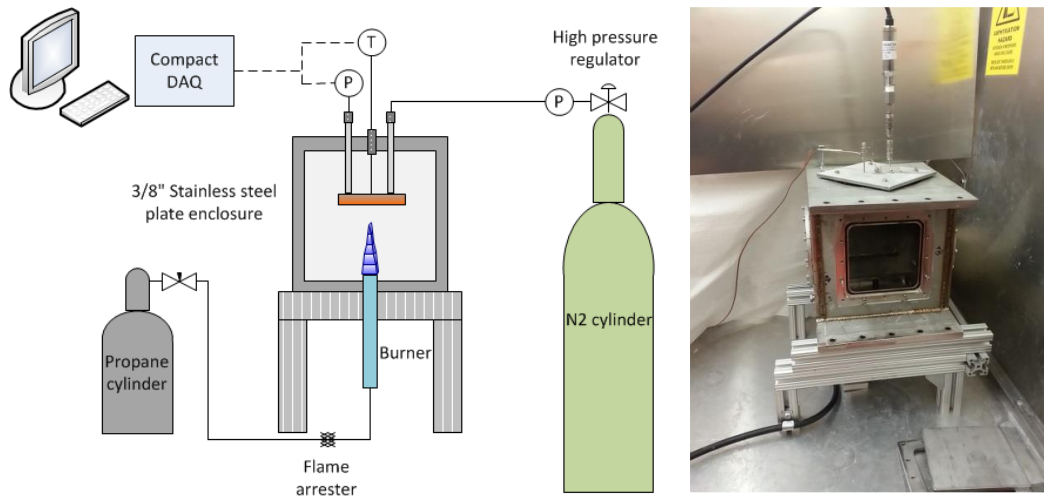


Figure 16. Pressure and Temperature testing facility (a) schematic, (b) picture of test chamber

The testing was undertaken in three stages: (a) pressure testing up to 130 bar at room temperature; (b) temperature testing up to 800°C at 20 bar; and (c) pressure and temperature testing at 130 bar and 800°C, respectively. ASME Section VIII Div. 1 UG-101 code was followed as closely as possible in preparing the test procedures.

3.2 Thermal Fluidic Test Facility

The experimental approach for thermal tests consisted of performing separate effects tests on small-scale microchannel sCO₂ receiver test articles in the laboratory. A key part of the lab-scale test facility is the ability to obtain high flux from a simulated solar source. A custom-built high flux concentrator consisting of a Xenon arc lamp and an elliptical reflector was used to simulate concentrated solar irradiation onto the receivers. The remainder of the facility consisted of a multi-component open flow facility for sCO₂.

3.2.1 High Flux Solar Concentrator

The high flux solar concentrator was constructed as part a senior design team project that was completed with Eric Truong and the author. Based on the literature survey and power restrictions in the laboratory, the design of the concentrator consisted of a single 6 kW Xenon arc lamp (Osram XBO 6kW HS XL OFR) that was located at the focal point of a truncated ellipsoidal reflector. The design of the reflector was based on Monte-Carlo ray tracing simulations conducted by Mr. Truong and completed using the commercial software TracePro® (Lambda Research). Figure 17 (a-c) shows the schematic of the reflector along with simulations indicating that fluxes of 100 W/cm^2 and 400 W/cm^2 can be attained over a diameter of about 3.8 cm and 1 cm, respectively. It should be noted that the geometry of the lamp and the lamp support was modeled in TracePro so that any shadows cast on the receiver due to the support would also be modeled.

Once the design was finalized, manufacturing of the reflector was undertaken in three phases at three different facilities. The rough shape of the reflector was milled out of a single 193 kg block of 6061 aluminum using a Fadal CNC88HS mill at Oregon State University's machine shop. The reflector was then shipped to KAF Manufacturing in Stamford, CT, for precision diamond-turning to generate a mirror surface finish. This machining step was necessary to ensure that the shape was precisely formed and the surface was adequately reflective. Following the surface preparation, the reflector was silver coated via a vapor deposition method by Universal Thin Film Lab in Newburgh, NY. Silver coating was necessary to ensure a high reflectance in the entire spectrum of

the Xenon arc lamp (data in literature suggests an average reflectance greater than 97 percent through the entire emitted spectrum).

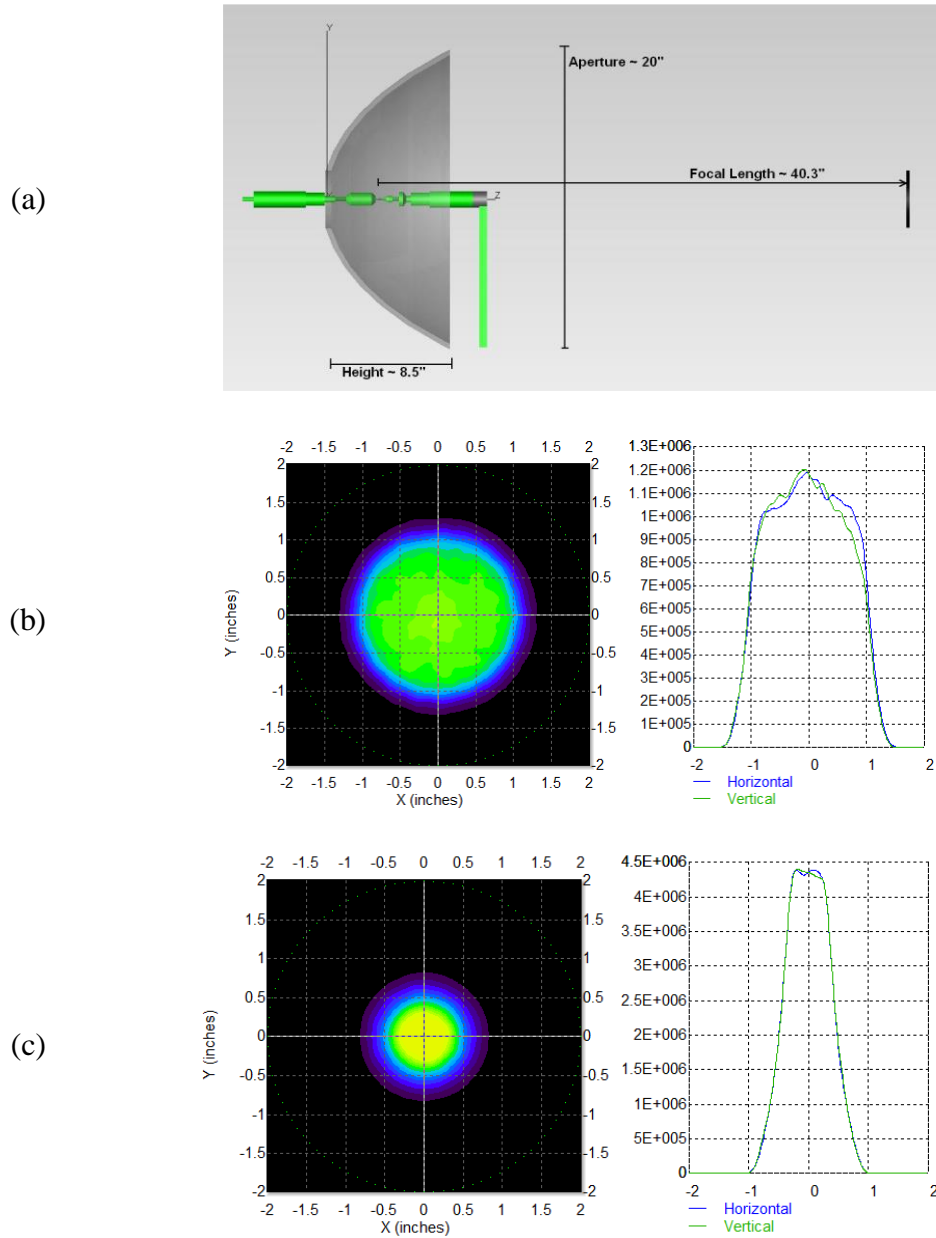
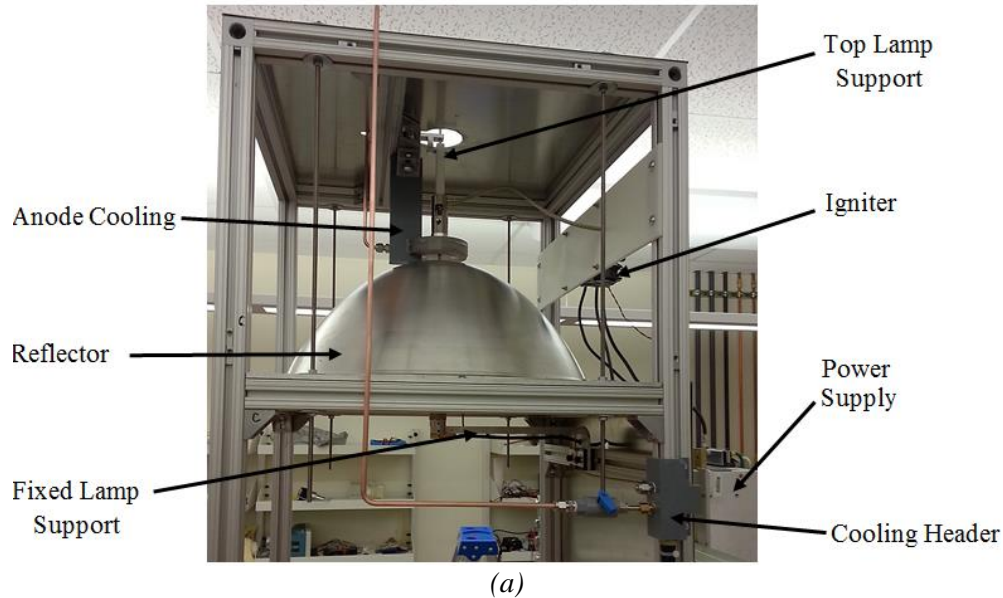


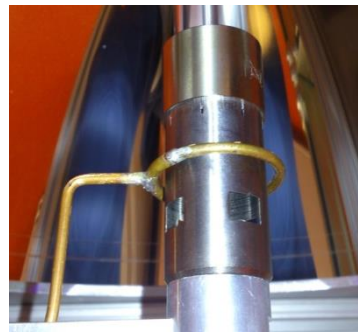
Figure 17. Simulation of the reflector using TracePro ® (a) reflector geometry, predicted flux map for 100 W/cm^2 achieved at a distance of $\sim 65 \text{ mm}$ downstream of the second focal point (b), and 400 W/cm^2 achieved at a distance of $\sim 25 \text{ mm}$ downstream of the second focal point (c).

Figure 18a shows the key components of the reflector, lamp, power supply, and cooling systems. Aluminum sheeting was installed around the outside of the frame and above the test section to protect operators from emitted light and heat. The completed reflector and bulb were installed in the facility structure as shown in Figure 18b. The xenon arc lamp operates at a nominal current of 160A and 37V. A dedicated power supply (Lumina Power Inc. in Bradford, MA), along with an igniter, was used. Upon initiating start up, the igniter supplies up to 40 kV of ignition voltage to the bulb with a 1 microsecond rise time. This high voltage, low amperage supply is changed to the operating current and voltage conditions using a proprietary zero-voltage switching mechanism that minimizes the losses and noises. The power supply was controlled using a LabVIEW program via a 15 pin interface.





(b)



(c)

Figure 18. High flux concentrator facility. Key components include the lamp power supply and igniter (a), a parabolic reflector (b), and cooling system for the cathode.

The lamp is rigidly fixed at the base by an electrically isolated aluminum support arm. The top of the lamp is supported by a spring loaded high-temperature plastic connection to eliminate stress caused by thermal expansion. In order to remain under the permissible temperature limit of 200°C , a cooling system was developed. The cooling system consisted of two rings of forced air jets, one located at the base of the bulb and the other at the top. Figure 18c shows the cathode cooling arrangement which consists of a ring of 3.175 mm outer diameter (1.55 mm inner diameter) copper tubing arranged around the base of the bulb, with nine drilled holes directed vertically with the flow parallel to the major axis of the bulb. A similar cooling scheme was followed for the anode. A pilot probe along with a NIST traceable pressure transducer were used to determine the velocity of cooling flow around the lamp and ensure that the cooling air velocity was in excess of the requirements stipulated by the manufacturer.

3.2.2 Supercritical CO₂ Test Loop

The supercritical test facility is shown schematically in Fig. 19. The test facility located at the bottom of the flux concentrator facility and the test section was placed at the same vertical location from the bulb as the heat flux gage but at a precise offset horizontal distance from the gage. The x-y traverse was moved by this horizontal distance so that the same flux map that was recorded by the gage would be incident on the test section.

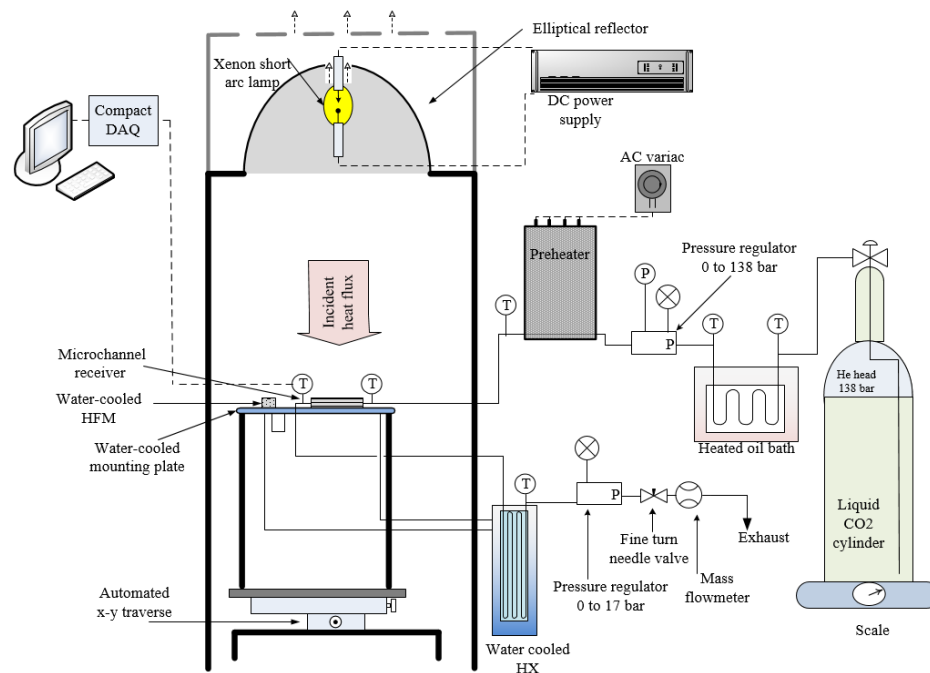


Figure 19. Supercritical carbon dioxide test loop schematic incorporated with the high flux solar concentrator

A wall panel was located beside the enclosure to mount test loop instrumentation such as inline pressure regulators and the mass flow meter. Liquid CO₂ at supercritical pressure is heated in two stages: first, the liquid CO₂ is vaporized at approximately

50°C in a hot oil bath and then heated to supercritical gas to approximately 450°C in a custom-built preheater.

Supercritical pressure within the test section was maintained using two high pressure regulators. The first regulator was used to adjust the cylinder pressure to the desired test condition 120 bar, but restrictions from the sCO₂ supply tanks forced an actual typical operational pressure of 85 bar. An absolute pressure transducer was located on the exit port to measure the test article inlet pressure. A second pressure regulator maintains the system pressure and reduces the CO₂ pressure to near atmospheric at its exit prior to the flowmeter. A dial pressure gauge located on this regulator was used to monitor the downstream pressure. Past the receiver and prior to the second pressure regulator, the temperature of the fluid was reduced in a water cooled heat exchanger. A fine turn needle valve with Vernier handle was used to control the flow rate through the test section. Down-stream of the valve, the gas was cooled to around 40°C before entering the pressure regulator. A calibrated Brooks mass flow meter was used for measuring the CO₂ mass flow rate. Data from the flowmeter, pressure transducer, and thermocouples were read directly by LabVIEW, using National instrument DAQs. An image of the constructed sCO₂ test facility is provided in Fig. 20.

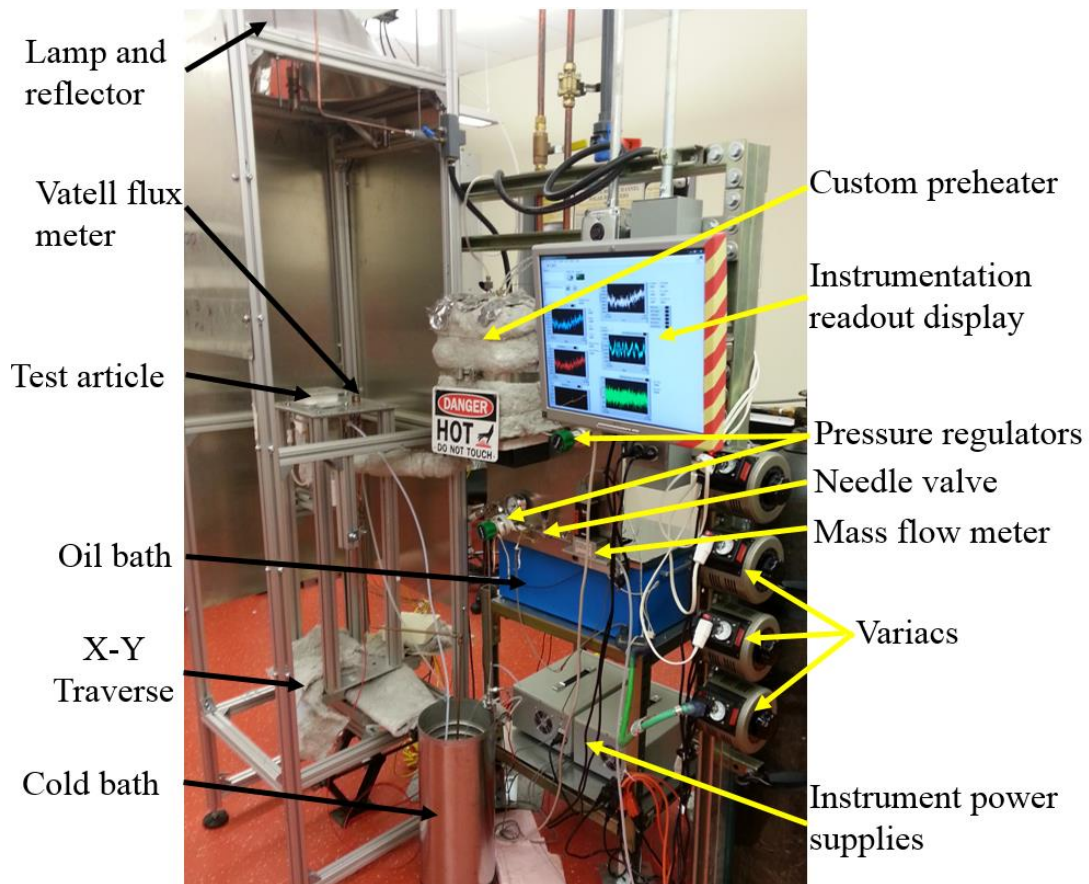


Figure 20. Supercritical carbon dioxide facility with each major component labeled

A design stage uncertainty analysis was undertaken to estimate the errors to be anticipated using this facility for estimation of the efficiency. The results from this analysis indicate that efficiency could be determined with an uncertainty of about 6 percent and that this estimate is dominated by error in heat rate estimation. A complete list of the instrumentation used in the test loop is provided below in Table 3.

Table 3 –Experimental device list

Manufacturer	Device Type	Model Number	Operational range	Factory Calibration
Vatell Corporation	Flux meter	TG1000-1 w/ AMP-15	0-600W/cm ²	Yes
Brooks Instrument	Mass flow meter	SLA5861S1BAA0B2A1	0-2.50g/s	Yes
Omega	Abs. pressure transducer	MMA2.5KV10P4C0T3A5CE	0-175 bar	Yes
Omega	Type K thermocouple	TJ36-CASS-116U-2	899°C max	
Swagelok	Inlet pressure regulator	KPP1NNF422P20000	0-2000psi control	
Swagelok	Outlet pressure regulator	KPR1GPM412A20000	0-250psi control	
Swagelok	Needle valve	SS-4MG-MH	42 slpm	
Validyne Engineering	Differential pressure transducer	P55E1N246S4A	±50psi	Yes
National Instruments	16bit analog voltage output module	NI 9263	±10V	
National Instruments	16bit analog input module	NI 9205	±200mV to ±10V	
National Instruments	Digital in/out module	NI 9375	In: 0-30VDC Ext Out:6-30VDC	
National Instruments	16 Channel Thermocouple module	NI 9213	±78.125mV	
Airgas	CO ₂ Cylinder	CD SFE15ASHP	2000psig	99.9995% Purity

3.3 Pressure Drop Test Facility

During the time frame for pressure drop testing phase, the solar concentrator was sought for alternative applications. To accommodate these changes the sCO₂ test loop was moved to another section of the lab and reassembled in the exact configuration. The only alteration to the loop were 4 way cross fittings put in place of the T fittings used to mount the inlet and outlet thermocouples for measuring gas temperature of the LSR. These 4 way fitting were used to incorporate a Validyne P55E differential

pressure transducer. Figure 21 is the modified test loop with added differential pressure transducer.

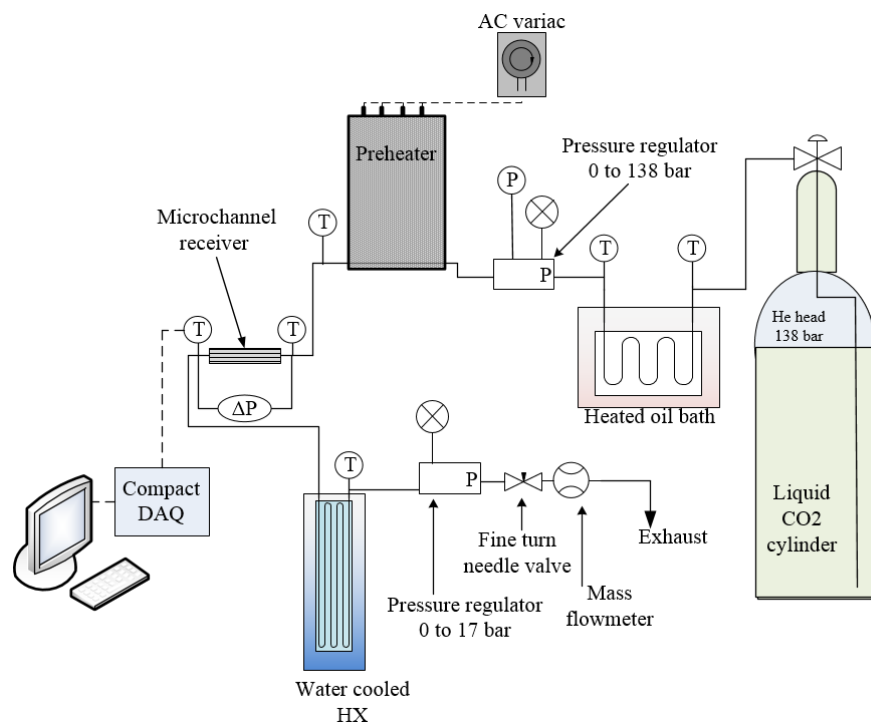


Figure 21. Modified $s\text{CO}_2$ test loop with added differential pressure transducer.

4. Lab-scale Receiver- Data Analysis, & Results

Experiments and data analysis performed on the LSRs is presented in this chapter. Prior to thermofluidic testing, the fabricated receivers were verified for structural integrity through static pressure tests at temperature. The main parameters of interest in thermofluidic testing of the LSRs were the receiver and thermal efficiencies as a function of incident heat flux and exit fluid temperature. Also of interest was a measurement of pressure drop across the LSR. This chapter details the efforts in data analysis and the uncertainty involved in each measurement and final reported values.

4.1 Integrity test

Structural integrity tests were performed using the facility shown in Fig. 16 in the prior chapter. Pressure testing at temperature of the parallel channel and pin arrays are shown in Fig. 22a & 22b. As seen from the plots, both receivers passed the integrity tests at the expected temperatures for which they were designed, approximately 730°C at 125 bar. Note that the dwell times and pressure increments were in accordance with the ASME test standards, see Appendix 8.1 for more details.

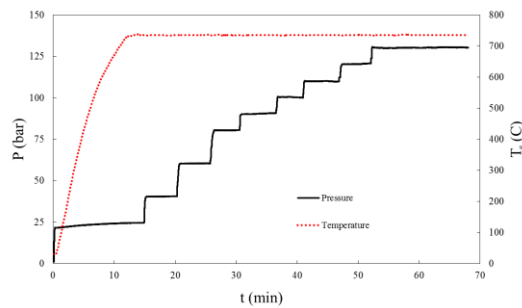


Figure 22a. Parallel channel integrity test at operating temperature and pressures

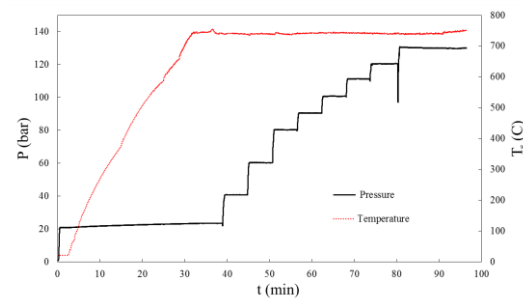


Figure 22b. Pin array integrity test at operating temperature and pressures

4.2 Definitions of Receiver and Thermal Efficiency for Experiments

Receiver efficiency was defined based on the absorbed heat by the working fluid to that incident on the receiver surface,

$$\eta_{rec,exp} = \frac{\dot{m}_{sCO_2}(h_{out} - h_{in})}{q_{incident}} \quad [5]$$

A second receiver performance parameter, the thermal efficiency, was also used to represent the receiver performance. The thermal efficiency of the receiver was defined as the ratio of the heat absorbed by the working fluid to the heat absorbed by the receiver,

$$\eta_{rec,exp} = \frac{\dot{m}_{sCO_2}(h_{out} - h_{in})}{\alpha \cdot q_{incident}} \quad [6]$$

Thus, in this efficiency definition, the reflection losses are not included. Therefore the thermal efficiency is a measure of the efficacy of using microchannels and is decoupled from the performance of the optical coating on the receiver surface.

Based on the above definition of receiver and thermal efficiency, it is clear that three quantities needed to be estimated: spectrally-averaged surface absorptivity in the insolation wavelength, the incident heat flux produced by the solar concentrator, and the heat rate absorbed by the sCO₂. The spectrally averaged absorptivity is determined based on the assumption of opacity from the spectrally-averaged reflectivity,

$$\alpha_{Haynes} = 1 - \rho_{haynes} \quad [7]$$

The spectrally averaged reflectivity is determined by integrating the spectral reflectivity with the spectral irradiation of the Xenon arc lamp,

$$\rho_{Haynes} = \frac{\sum(\rho_{\lambda,Haynes} \cdot E_{\lambda,Lamp} \cdot d\lambda)}{\sum(d\lambda \cdot E_{\lambda,Lamp})} \quad [8]$$

In the LSR experiments, with the exception of the 2 cm x 2 cm insolation area, the rest of the LSR was covered in insulation. The next step was to characterize the surface condition in terms of reflectivity, and ultimately absorptivity, of the LSR.

4.3 Reflectivity

Figure 23a shows a picture of the bare Haynes 230 receiver surface upon completion of the high-flux experiments. A bluish purple discoloration of the surface was observed. A sample was prepared in a similar manner (sanded and exposed to concentrated flux) for reflectivity measurements in the spectrophotometer (Fig. 23b). A burn in cycle of the surface was performed by running the high flux experiment first until steady state; thus any discoloration of the surface would have been completed during burn in.

The reflectivity of the bare Haynes was assessed using a spectrophotometer (JASCO UV-670), with a manufacturer stated accuracy of 0.3% for transmittance measurement and 0.05 nm for wavelength. Reflectance was measured at room temperature and at a

single angle of approximately 10 degrees off normal. In order to obtain an accurate surface reflectance, the device was cut using wire EDM after all testing was complete so the channel section could be placed into the spectrophotometer part holder. Since the output of the Xe lamp is dependent on the wavelength, the relative output of the lamp was obtained as a function of wavelength.

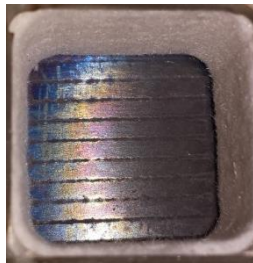


Figure 23a. Test article channel area after testing without absorber coating



Figure 23b. Test sample without absorber coating after burn in cycle to match channel area

Figure 24 shows results of the spectrophotometer. It can be seen that the reflectivity of the bare Haynes surface is significantly larger than that with the Pyromark paint.

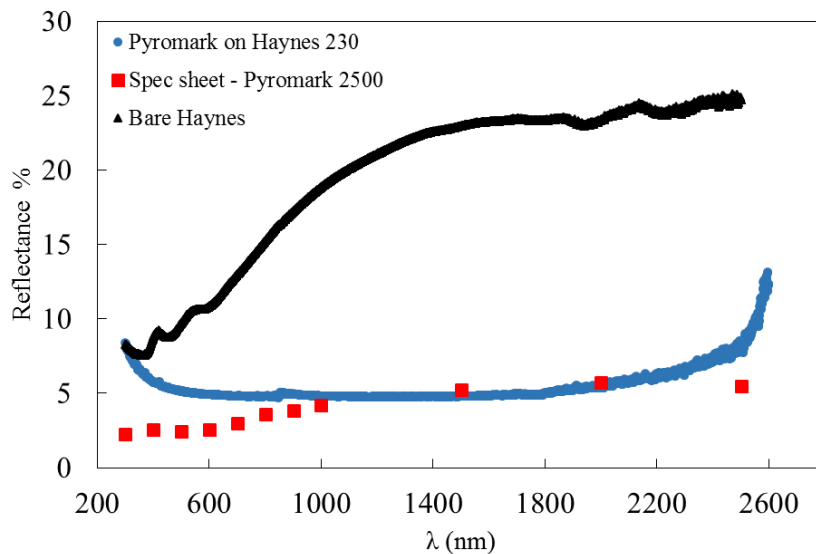


Figure 24. Reflectivity of the bare Haynes surface compared to Pyromark paint.

To determine the spectrally-averaged reflectivity over a wavelength range of 200 to 2500 nm, numerical integration was performed on Eq. 8. An eight term Fourier curve fit was generated using Matlab's built in curve fitting software applied to the Haynes reflectivity data. This curve fit was then used to numerically integrate at the same wavelengths as the lamp output. Curves of spectral dependence of reflectivity and lamp irradiation are shown in Fig. 25. The integration provided a ρ_{Haynes} of approximately 0.172. The absorptivity, for use in Eq. 10, was evaluated based on this surface reflectivity and the assumption of opacity of the surface.

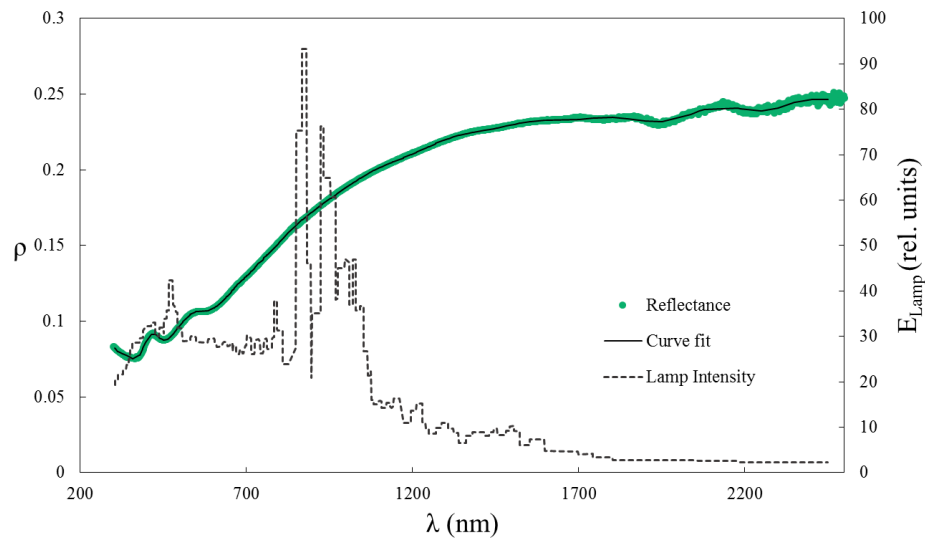


Figure 25. Spectral dependence of reflectivity and lamp irradiation

4.4 Incident Heat Flux

Heat flux values were determined through a water cooled Vatell TG1000-1 flux meter gauge with an AMP-15 amplifier to read fluxes ranged from 0 to 600W/cm². Vatell provided a NIST traceable certificate of calibration for this flux meter. The heat flux meter is fixed to a 26 x 26 cm² water-cooled aluminum plate and mounted to a stage

that is connected to a 2D stepper-motor controlled traverse. This traverse is controlled using a LabVIEW program that specifies the area over which heat flux measurements are to be recorded. Figure 26a shows a picture of the heat flux gage with the lamp in operation. The obtained flux distribution is found to be very sensitive to the placement of the lamp with respect to the first focal point. A secondary heat flux meter was constructed to refine the obtained flux distributions, as seen in Fig. 26b.

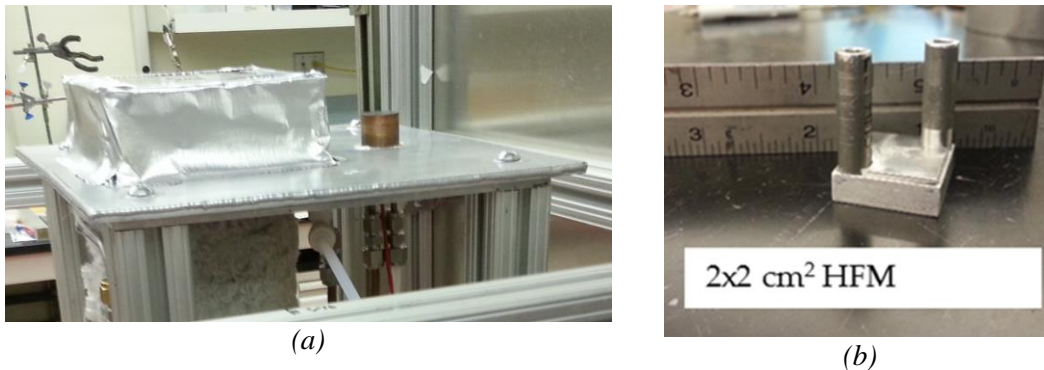


Figure 26. (a) Heat flux gage mounted to water cooled plate along with the insulated test article (b) Custom heat flux meter used to confirm incident heat flux data collected using Vatell heat flux meter

Heat fluxes on the average of 90 W/cm^2 , with a peak of 119 W/cm^2 (peak to average flux ratio of 1.37) could be obtained over a circular region of diameter of approximately 2 cm, Fig. 27a. As an example of higher flux distribution, an average flux of 291 W/cm^2 with a peak of 391 W/cm^2 (peak to average flux ratio of 1.34) was obtained as shown in Figure 27b. Higher values of average fluxes (with peaks upwards of 600 W/cm^2) were obtained in experiments; however the peak-to-average values for these maps were large. A custom heat flux meter was fabricated used to confirm incident heat flux data collected using Vatell heat flux meter. Table 4 displays the results.

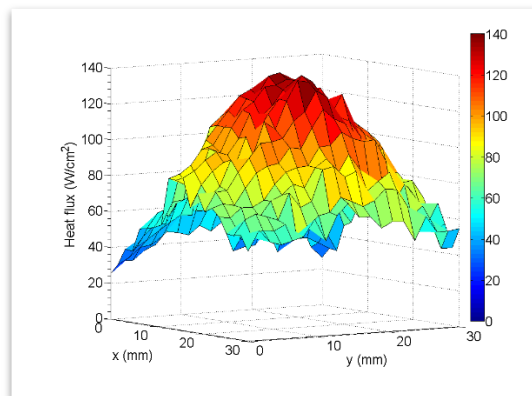


Figure 27a. Incident flux map of $\sim 100 \text{ W/cm}^2$ over 3 cm diameter

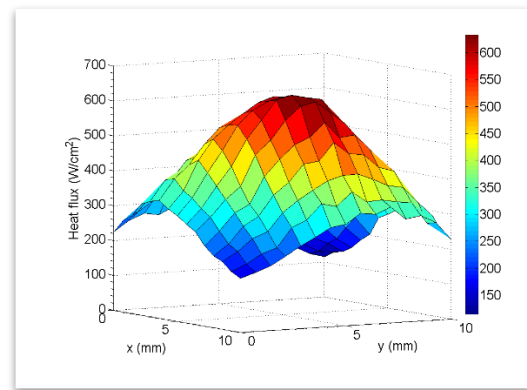


Figure 27b. Incident flux map of $\sim 350 \text{ W/cm}^2$ over 1 cm diameter

Table 4. Results of custom heat flux meter used to confirm incident heat flux data collected using Vatell heat flux meter

Custom heat flux meter (W/cm^2)	Vatell heat flux gage map average (W/cm^2)	Difference (%)
83.7	77.9	7.2
107.2	104.3	2.7

4.5 Results

This subsection covers the results of all experiments of the LSRs. Pressure drop results are covered first followed by the thermal performance characterization. During thermal characterization a need to characterize heat loss of the experimental setup arose. The explanation of the methods and concerns are thoroughly detailed. Finally an uncertainty analysis of the experimental process is covered.

4.5.1 Pressure drop

Pressure drop for the pin fin array was experimentally obtained using a high line pressure differential pressure transducer (Validyne P55E-1N246S4A). Flow was held at approximately 100°C to ensure the gas was above critical temperature and pressure was matched to be identical to that in efficiency experiments. As can be seen in Fig. 28, the pressure drop increases with an increase in mass flow rate. The pressure drop is also plotted against Reynolds number based on hydraulic diameter, R_{DH} , for reference. For typical heat transfer experiments, where the flow rate is about 1 g/s, the pressure drop across the LSR is under 0.5 bar. Similar pressure drops could be expected in larger scale receivers since the flow through the micro pin fin regions would occur in a parallel network. It is also important to note that, based on the R_{DH} , the flow is expected to be in the transitional to turbulent regime through the pin fin receiver. Given that most of the correlations for pressure drop and heat transfer rate in micro-pin fin heat sinks have been developed for the laminar flow regime, there is a need for expanding the correlation database to cover the transitional and turbulent regimes as seen with the present sCO₂ LSRs.

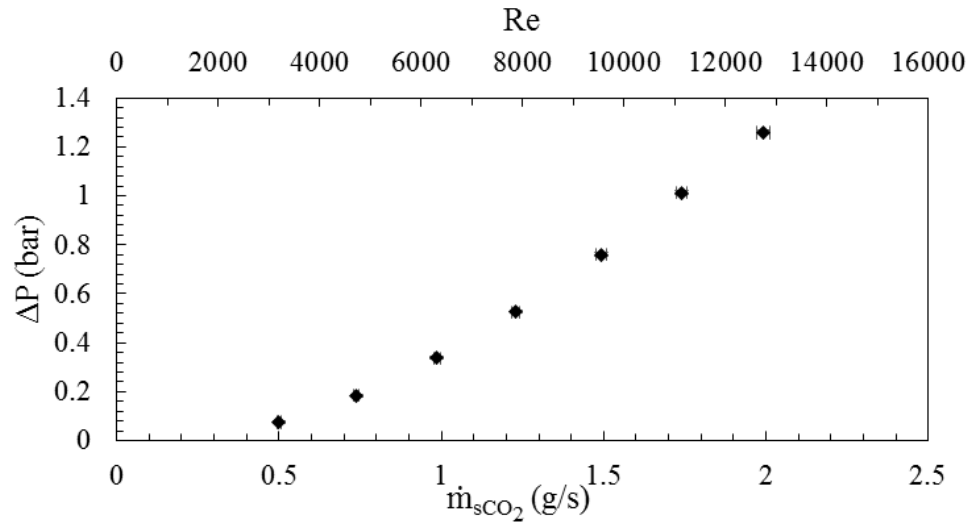


Figure 28. Experimental pin fin array pressure drop

4.5.2 Thermal efficiency tests

Characterization of the receiver efficiency was accomplished by measuring the mass flow rate of the gas, the inlet and outlet flow temperatures, operating line pressures, and the incident flux. Experiments were performed at varying gas exit temperatures and constant incident flux to compare the theoretical trend. If the incident flux is constant, but the receiver temperature and therefore the fluid exit temperature rises, the efficiency of the receiver will diminish. The reverse was also characterized, the exit temperature of the fluid was held constant and the incident solar flux was varied.

The parallel channel and pinfin array LSRs were characterized for efficiency in the sCO₂ test facility. Figures 29 & 30 summarize the experimental runs performed for these receivers. Two main parameters were varied- (a) the incident flux at a fixed fluid exit temperature (Fig. 29), and (b) fluid exit temperature at a fixed input flux (Fig. 30).

In all experiments the inlet fluid temperature was maintained at approximately 400°C and the receiver pressure was maintained between 81-86 bar.

As shown in Fig. 29, both thermal and receiver efficiency are seen to increase with increasing heat flux. The thermal efficiency for the parallel channel varies from 60.7 percent at 68.1 W/cm² to about 71.6 percent at 120.3 W/cm², while the receiver efficiency increases from 73.3 percent to 86.4 percent over this same range of heat fluxes. As for the pin array LSR, the thermal efficiency for the pin array varies from 72.3 percent to 83.9 percent with the variation in heat flux from 73 W/cm² to 120 W/cm². With an increase in irradiation, the amount of heat transferred to the working fluid increases; however there is not much variation in surface temperature. The negligible change in receiver surface temperature results in a negligible variation in re-radiation and natural convective losses from the 2 x 2 cm² exposed area. However, since the flux is increasing, an increase in efficiency with incident heat flux increase is observed, as per Eq. 2. The ability to be able to absorb high incident fluxes at a fixed surface temperature is a crucial advantage of the microchannel receivers. It should be emphasized that the receiver efficiency is for a bare surface and not with a high absorptivity coating. Since the intent was to demonstrate that the use of microchannels permits removal of high incident fluxes at high efficiency, the metric that really matters is the thermal efficiency, since this is independent of the receiver coating.

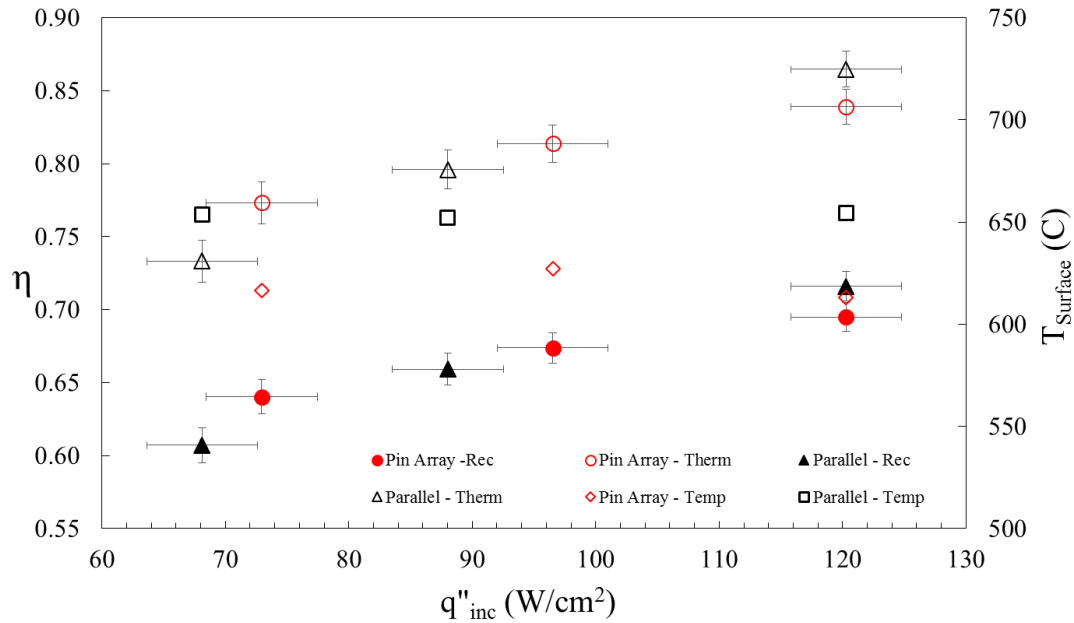


Figure 29. Receiver and thermal efficiency with variation of incident flux at a fixed exit temperature of $\sim 650^{\circ}\text{C}$. Also plotted is the average surface temperature of the device

Figure 30 shows the variation of thermal and receiver efficiency for a fixed input heat flux but varying exit temperatures. The exit temperature variation is caused in experiments by varying the mass flow rate of sCO_2 . Variation in the exit temperature for a fixed inlet temperature and input heat flux caused changes to the surface temperature. Lower exit temperatures result in lower surface temperatures, and thereby increased efficiencies as per Eq. 2. The trend in Fig. 30 shows that commensurate with this increase in surface temperature, a reduction in thermal and receiver efficiency is observed due to increased losses. The thermal efficiency of the pin array drops from 80.3 percent at a receiver exit fluid temperature of 606°C to 70.1 percent at an exit fluid temperature of 735°C . The thermal efficiency of the parallel channel drops from 81.0 percent at a gas exit temperature of 624°C to 73.1 percent with an exit temperature of

715°C. The non-uniform drop in efficiency for the parallel channel as compared to the pin array is likely due to experimental error in the data at a surface temperature of 650°C. The ability of the microchannel receiver to reduce the diffusion resistance in the fluid results in a reduced surface temperature for a fixed flux resulting in an increased efficiency. Regardless, thermal efficiencies above 90 percent were not achieved for both LSR designs at exit fluid temperatures of 735°C. To account for the inability to achieve the efficiencies, heat loss from the test article through the insulation had to be characterized.

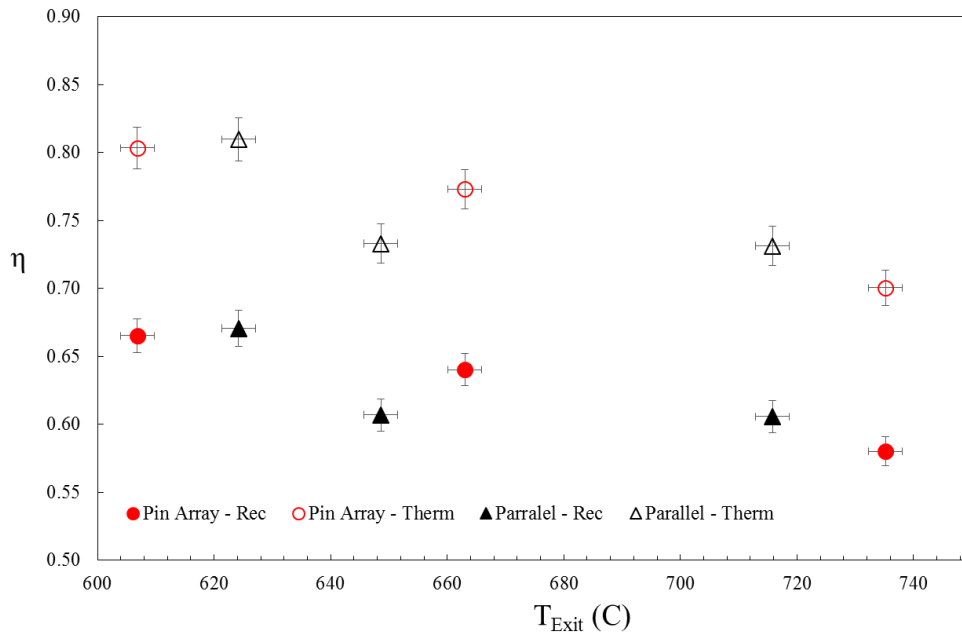


Figure 30. Receiver and thermal efficiency variation with exit temperature at a fixed incident flux of 68.1 W/cm² for the parallel channel and 72.95 W/cm² for the pin array

4.6 Heat Loss

Heat losses, on the order of 10 percent, occurred through the insulation. Since the microscale area of the LSRs spanned only $2 \times 2 \text{ cm}^2$ while the overall receiver surface area was $6 \text{ cm} \times 4 \text{ cm}$, the metal area was 6 times larger than the microchannel insulation area ($2 \times 2 \text{ cm}^2$) leading to approximately 10 percent thermal losses through the un-insolated area of the receiver. Since in a commercial receiver, the microscale area would cover the entire face of the flux absorber surface, such thermal losses from the non-microscale regions would be an artifact solely of the LSR tests. Efficiency numbers, corrected for such thermal losses through the insulation, would be more representative of the commercial scale receiver efficiencies that can be obtained using microchannels. The inefficiencies would then arise solely due to the re-radiation and convective losses from the surface of the receiver that is exposed to the simulated solar flux. Upon correction for heat losses, a modified receiver efficiency is defined as the heat gained by the fluid to the net heat incident on the receiver,

$$\eta_{rec,exp,heatloss} = \frac{\dot{m}_{SCO_2}(h_{out} - h_{in})}{q_{incident} - q_{loss}} \quad [9]$$

where the net heat is determined by subtracting thermal losses from the incident heat rate. Similarly, the modified thermal efficiency was defined as

$$\eta_{therm,exp,heatloss} = \frac{\dot{m}_{SCO_2}(h_{out} - h_{in})}{\alpha \cdot q_{incident} - q_{loss}} \quad [10]$$

In order to estimate heat losses through the insulation, a separate heat loss calibration experiment was performed for each of the lab-scale receivers, as discussed in the next chapter.

In order to estimate heat losses through the insulation in Eq. 9-10, a separate heat loss calibration experiment was performed for each of the lab-scale receivers. A schematic representation of the test facility for heat loss calibration is shown in Fig. 31. The upper $2 \times 2 \text{ cm}^2$ surface of the receiver that is exposed to concentrated radiation in the sCO_2 experiments was thoroughly insulated for the heat loss experiments. The remainder of the receiver insulation was identical to that during the sCO_2 tests. Heated nitrogen gas was flowed at a metered flow rate through the receiver and the drop in temperature of the gas at the exit of the receiver at steady state was noted to determine the heat loss. The average of the seven thermocouples located on the body of the LSRs was averaged to represent the body temperature at which the heat loss was determined. Figure 32 shows a plot of estimated heat losses as a function of this average body temperature. A best fit curve that represented the data was used to estimate heat losses in the sCO_2 experiments. Note that the curve fit was linear, indicating that heat loss was by conduction through the insulation. The heat loss experiments were restricted to temperatures of $\sim 400^\circ\text{C}$, the highest gas temperature possible with the preheater. However, since the curve fit was linear, the heat loss projections were extrapolated to higher surface temperatures ($600\text{-}750^\circ\text{C}$) seen in actual experiments. The slight difference in slope of heat loss between designs is attributed to the variation of insulation during setup of the two separate experiments.

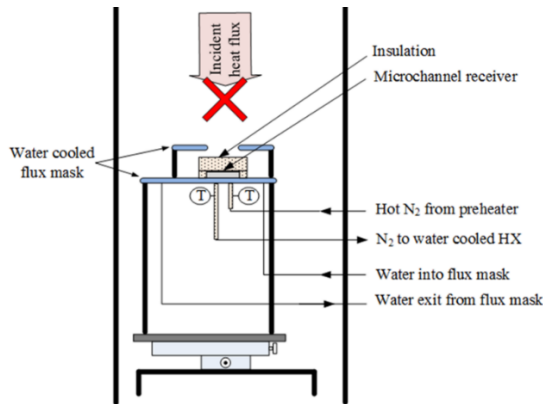


Figure 31. Schematic of the facility for in-situ heat loss calibration. The entire LSR was insulated and no concentrated flux was applied.

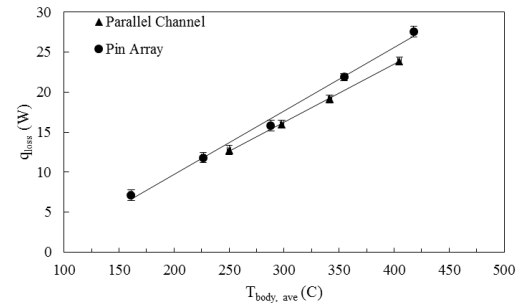


Figure. 32. Heat loss calibration curve for the LSRs

Losses are proportional to the surface temperature and at a constant surface temperature and an increase in incident heat flux will produce an increase in efficiency. Figure 33 replots the points of Fig.29 with the inclusion of the heat loss term in Eqs. [9-10], the thermal efficiency for the parallel channel varies from 89.9 percent at 68.1 W/cm^2 to about 96.6 percent at 120.3 W/cm^2 , while the receiver efficiency increases from 71.7 percent to 78.4 percent over this same range of heat fluxes. The thermal efficiency for the pin array LSR is largely constant around 94 percent with variation in heat flux from 73 W/cm^2 to 120 W/cm^2 . When the heat loss through the insulation is taken into account, the thermal efficiency of both devices is shown to exceed the mark of 90 percent efficiency.

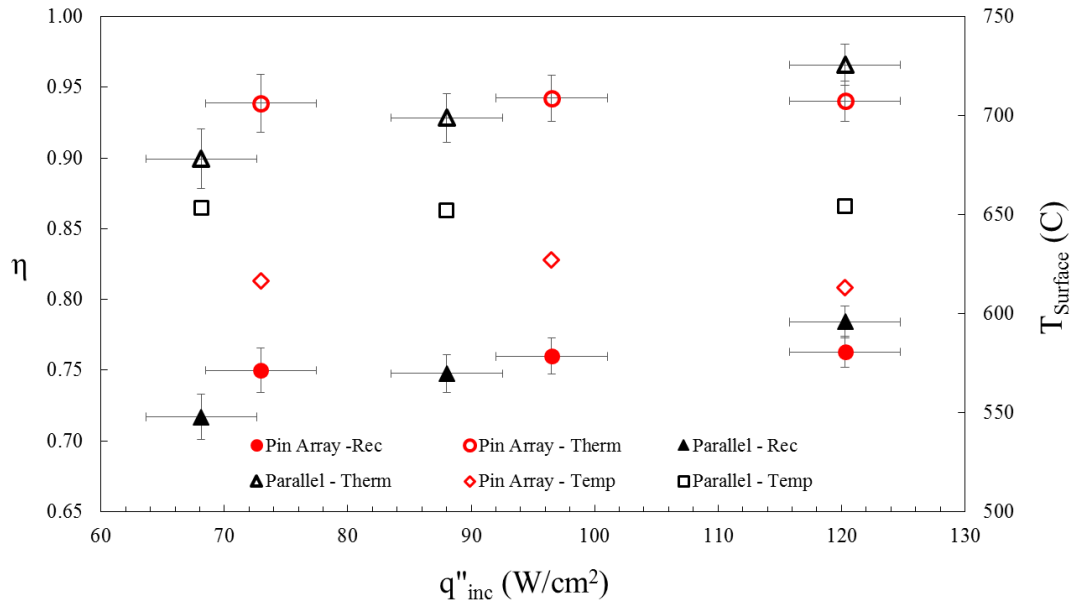


Figure 33. Receiver and thermal efficiency with variation of incident flux at a fixed exit temperature of approximately 650°C with the inclusion of heat loss

4.7 Uncertainty Analysis

Thermocouples reading the fluid temperatures were calibrated using a NIST-traceable hand held calibrator (Omega, PCL-1B) as a standard. The calibration error included errors associated with the calibrator, the calibration precision error and the curve fit error. The differential and absolute pressure transducers and both the volumetric and mass flow meters were factory calibrated.

The Kline and McKlintock error propagation method [30] was used to determine uncertainties in the calculated parameters based on the bias and precision errors of the measured variables. Uncertainties in measured parameters were obtained by combining the measurement precision calibration errors in a root-sum-square manner. Engineering

Equation Solver (EES, Fchart Inc.) was used to perform the propagation of errors. Maximum uncertainty in measured variables was propagated into the dependent variables. Representative measurements of the uncertainty are provided in Table 5.

Table 5. Representative measurement uncertainty estimate

Measurement	Maximum Uncertainty (\pm)
Volumetric flow rate (N_2)	± 0.115 slpm (0.32%)
Mass flow rate (sCO_2)	± 0.0114 g/s (1.0%)
Average gas temperature	± 0.46 °C (0.12%)
Surface temperature	± 2.81 °C (0.4%)
Heat flux	± 4.5 W/cm ² (6.17%)
Absolute pressure	± 0.35 bar (1.63%)
Pressure drop	± 0.004 bar (6.28%)

5. Integrated Receiver - 8cm x 8cm Test Article

The LSR design was used to develop a concept for a scaled up 8x8 cm² test article also denoted as an Integrated Receiver (IR). Since the ability of the unit cell in removing desired heat fluxes was demonstrated in Chapter 4, in designing the scaled up receiver, the main design objectives were to determine the fluidic headering design and integrated fabrication of the multiple unit cells with the headers. This design work was completed by Dr. Erfan Rasouli. Once the design work completed, the Author completed the fabrication tasks and conducted the experimental testing for structural integrity at proposed operating conditions as was done for the LSR designs. Further the Author completed experimental flow distribution maps through the use of infrared imaging.

5.1 Structural Design

Based on the chosen dimension for the scaled up IR test article of 8 cm x 8 cm, 16 unit cells of the type demonstrated in the LSR design can be located in the plan area. Figure 34a depicts the receiver plate with the 16 unit cell arrangement with micro-pins in the 2cm x 2cm regions. Figure 34b depicts the middle distribution layer, which is when bonded to the receiver plate would form the microchannel and provide inlet and outlet to each unit cell.

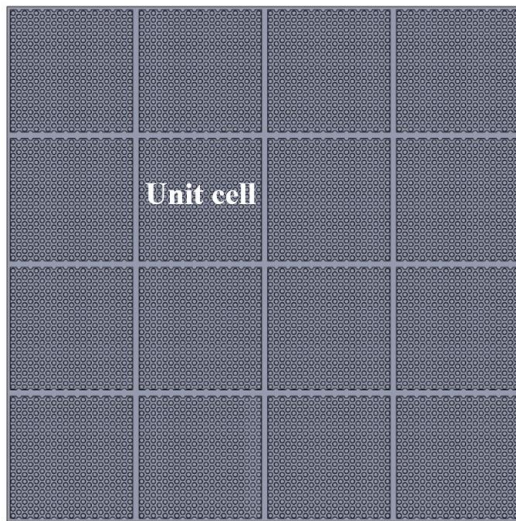


Figure 34a. Unit cells in scaled up test article

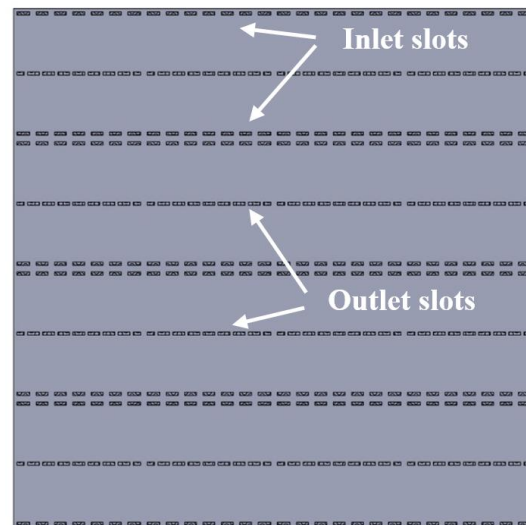


Figure 34b. Inlet and outlet slots for each unit cell

A header laminae would be needed above this layer to distribute fluid to all unit cells from a single inlet and exit. Figure 35 shows the concept for the headers. Two circular holes on the very top layer of test section (see Fig. 35a), are the main inlet and outlet of the 8x8 cm² test article. As is shown in Fig. 35a, the inlet flow enters into a large plenum with high aspect ratio pillars and then is distributed into each unit cell in the flux receiver plate through the guiding channels shown in Fig. 35c. After passing across the unit cells and absorbing incident heat, the hot fluid is collected by collector channels shown in Fig. 35c. Then the collected flow in each channel merges together in the header's outflow plenum and leaves the test article through a single hole on the very top plate of the test article. The aspect ratio of pillars in the plenums in the header section were higher than the micro pin fins in the receiver plate, so the pressure drop in the plenum would be lower compared to the unit cells which enables even distribution. The stack of laminae would be diffusion bonded to form the complete IR test article.

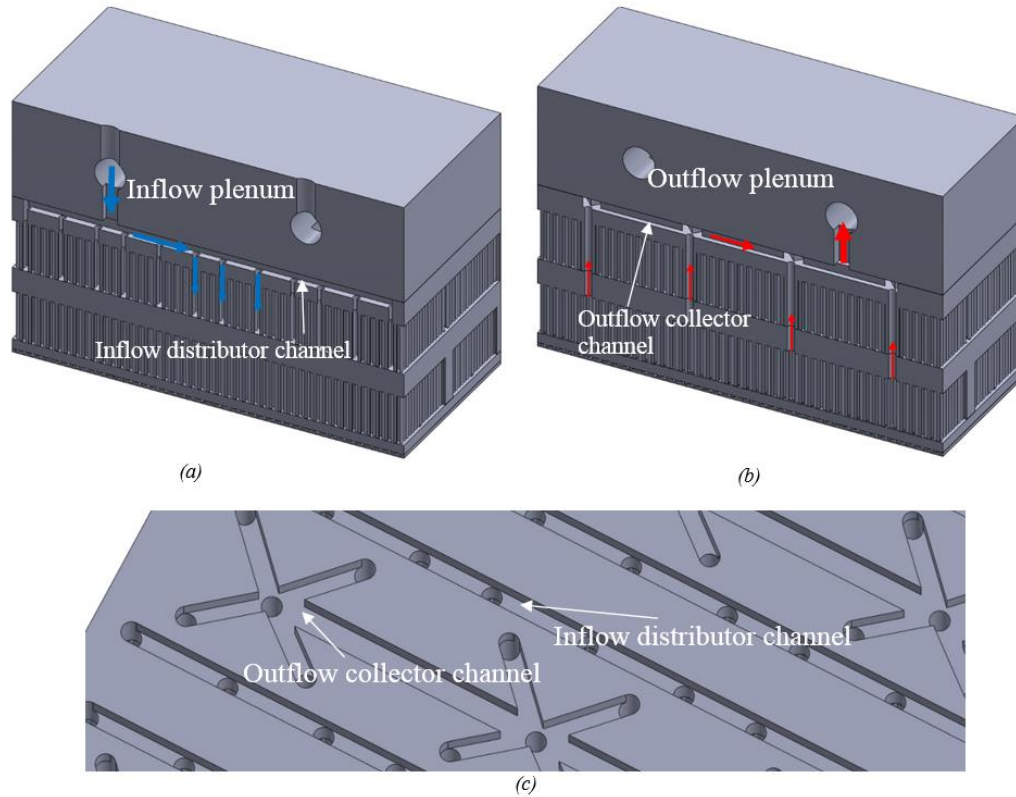


Figure 35. Illustration of the test section header (a) Inflow plenum. (b) Outflow plenum, and (c) The channels which distribute or collect fluid from each unit cell.

Diffusion bonding placed a constraint on the design of header section. For proper diffusion bonding, force have to be transferred from one layer to the next. Consider a scenario such as shown in Fig. 36, where one header layer with larger pins that are widely spaced would be located above the first row of micro pin laminae. High pressure (200 bar) supercritical CO_2 would flow through the plenum and the micro pin fin channel. During diffusion bonding, a uniform load is applied between the top and bottom boundaries of the device shown in Fig. 36. In order to affect a good diffusion bond, the pressure distribution on Path 2 in Fig. 36 has to be uniform during the bonding process.

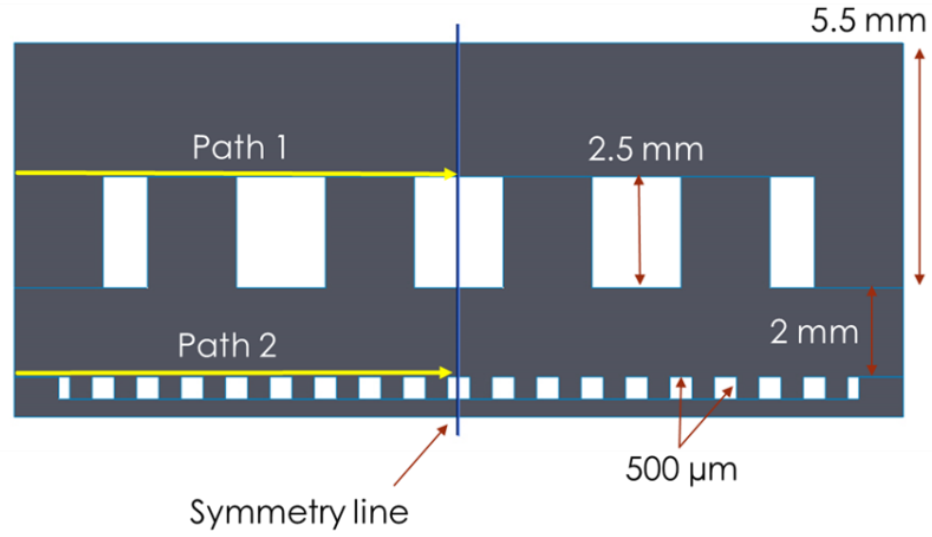


Figure 36. Cutaway schematic of a simulated plenum region and a pin fin microchannel region

The thickness of the metal between the plenum and the micro pin fin channels affects the uniformity of pressure distribution along Path 2 in Fig. 36. Solving Euler-Bernoulli beam equation for a simple beam with fixed ends and under uniform load shows that maximum stress occurs at the ends and it is equal to:

$$\sigma_{\max} = \frac{wl}{12Z} \quad [11]$$

Where W is the total uniform load (N), l is the length of the beam (m), Z and is the section modulus which for a beam with rectangular cross section is defined as,

$$Z = \frac{bh^2}{6} \quad [12]$$

where b is the width and h is the height (thickness) of rectangle. Increasing the thickness of the beam, increases the section modulus and consequently results in a decrease in the maximum stress at the ends of the beam, σ_{\max} . If this thickness is made sufficiently large, the pressure distribution could be made uniform; however making this wall too

large would result in increase in weight and cost of the receiver. FEA analysis was performed using ANSYS to determine the tradeoff between uniformity of pressure in Path 2 and wall thickness. In order to run the simulations, 15 MPa pressure was imposed on the very top layer while the edge on the bottom of part design was selected as fixed support. Results from these simulations are shown in Fig. 37 for wall thicknesses of 1, 2 and 3 mm (Note that Fig. 36 shows a schematic with a wall thickness of 2 mm). Equivalent (von-Mises) stress contours shown in Fig. 37 (a-c) shows qualitatively improvement in the uniformity of stress distribution by increasing the metal thickness. The stress intensity along path 2 for different wall thicknesses is plotted in Fig. 37d and it can be seen that the thinner wall thickness (i.e. 1mm) shows oscillations with larger amplitudes.

The material properties used for the simulations were representative of stainless steel 316. The pillars spacing and dimensions in the plenum section were determined by running simulations when 200 bar pressure was imposed on the internal walls. The critical locations in terms of stress concentration as labeled in Fig. 37 (a-c) with Max stress, are the sharp corners. The FEA analysis showed that stress concentration magnitudes on the corners are sensitive to the grid size.

In order to determine the necessary thickness between the header plena and the micro pin fin regions, test sections with various wall thicknesses of 1, 2 and 3 mm were designed are being fabricated. The intent is to determine what level of non-uniformity in stress intensity in simulations is acceptable for a diffusion bonded part based on rupture tests.

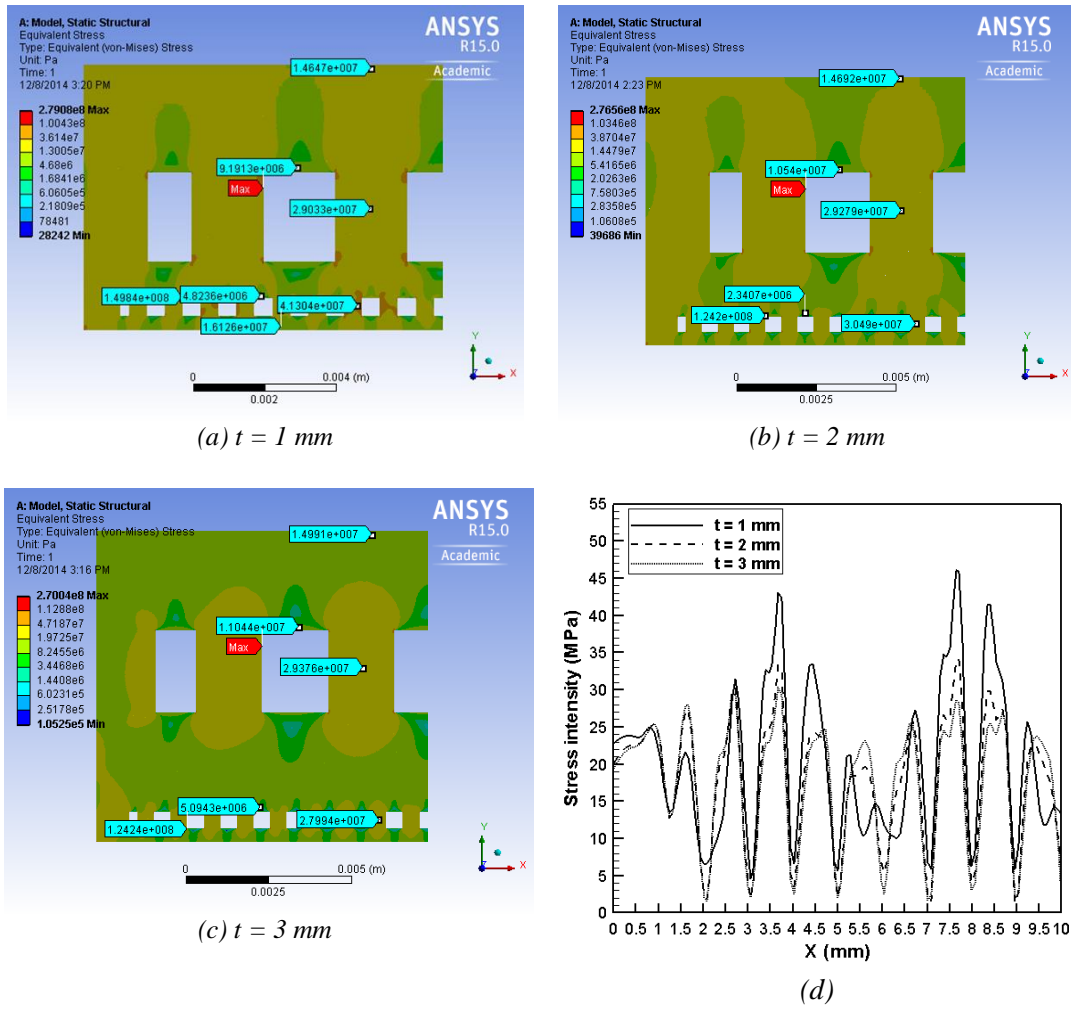


Figure 37. (a-c) Comparison of stress contours for wall thicknesses of 1, 2, and 3 mm; (d) Stress distribution comparison for the three wall thicknesses along path 2 in Fig. 36 (d)

Figure 38 shows assembly views of the stainless steel parts (with wall thickness of 2mm) that are under fabrication. The three piece assembly has $2 \times 2 \text{ cm}^2$ plan area. The through holes in the mid layer are for transferring the pressure from the large plenum into the flux receiver level with microscale pins. The pin spacing and dimensions in the receiver plate have been designed to withstand 200 bar internal pressure at room temperature. Of key interest is to determine whether the burst strength of the 1mm, 2 mm, and 3 mm test devices compare qualitatively with the simulation results.

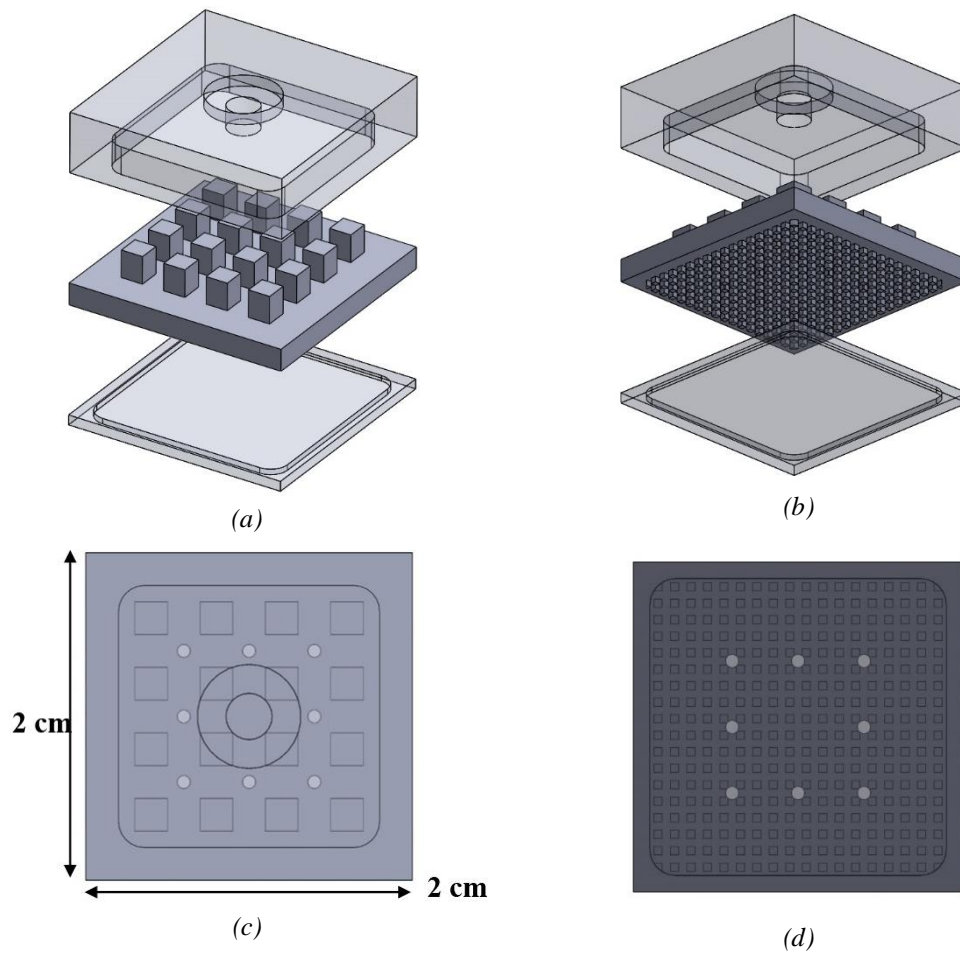


Figure 38. (a-b) Exploded views of the test sections sent out for fabrication. (c) Top view of the assembly showing the plenum section of the test article indicating the larger support pin structures that are widely spaced. (d) Bottom view of the assembly showing the microscale pin fin section with smaller pins that are closely spaced.

Figure 39 (a-c) illustrates the difference of the wall thicknesses in the test sections. A fourth test section was designed with wall thickness of 2 mm and identical pin spacing and dimensions in both plenum and receiver plate but varied in aspect ratio, see Fig. 39d. The comparison of burst results on this device with the one with larger support pin structures sheds light on the effect of unsupported areas which exist beneath plenum open areas with larger pins, on the bonding of microscale pins in the receiver plate. If the results show insignificant change in burst pressure by using microscale pin size in

the plenum, then considerable fabrication cost reduction can be obtained by having larger structures in the plenum.

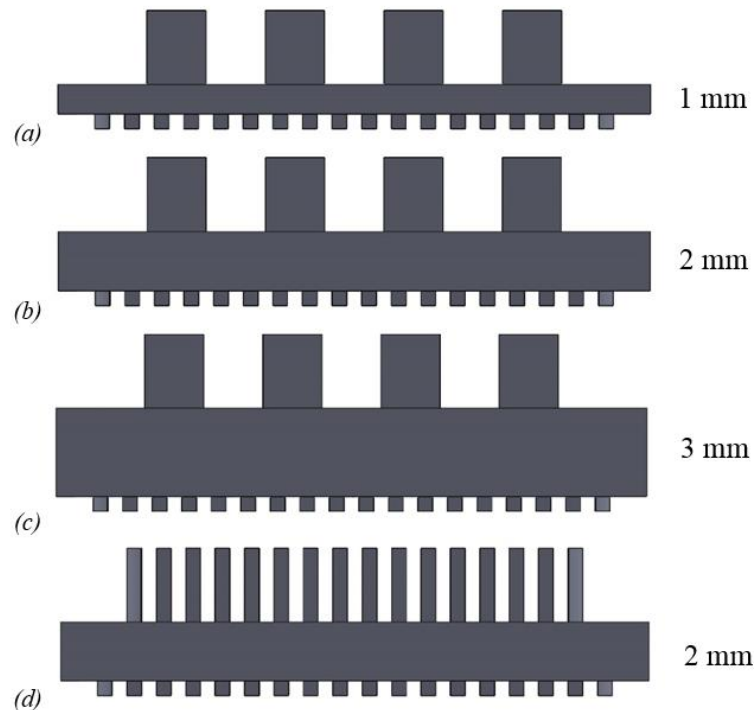


Figure 39. Front view of the mid layer in the test sections sent out for fabrication.

The first test article to be bonded was the one with 3 mm wall thickness (Fig. 39c design). Due to the large strain imparted to the test section ($\sim 25\%$) in the initial bonding recipe used, this test article did not provide usable data as the fluid pathways in the microscale region were heavily distorted. Sample SS 316 pieces of comparable thicknesses were bonded and used to arrive at the proper bonding parameters for the rest of the test sections.

The following bonding parameters were followed consistently for three test articles:

- 1050C bond temperature with 1 hr soak time at 1050C
- 2.10 MPa pressure for 3 hours
- Remove all loads for cooling; cooling at 5C/min

The process parameters resulted in an overall imparted strain (measured using digital calipers) of approximately 4.5 percent. Once the three test articles were bonded, burst tests were performed, and the test articles were subsequently sectioned for detailed measurements using an optical profilometer. Pressure tests were performed with a hand pump and water was used as the working fluid, Fig. 40.

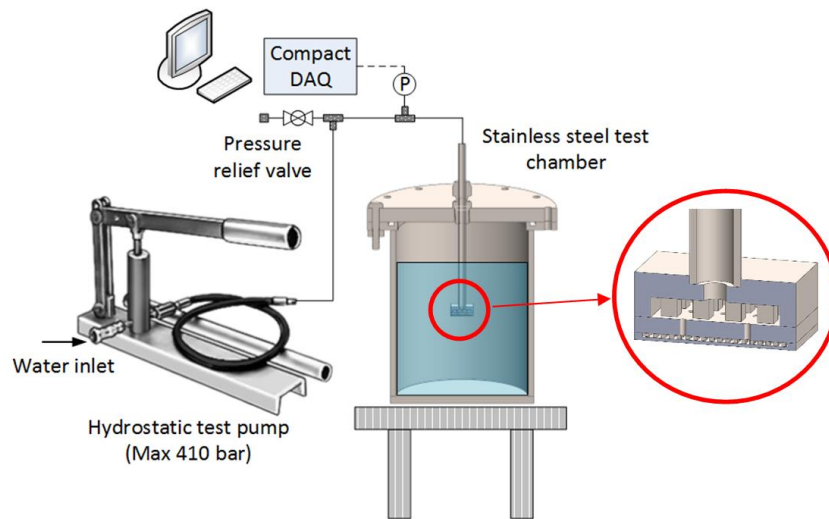


Figure 40. Schematic of designed pressure testing facility

The test sections were placed within a chamber to protect the operators in case of a catastrophic failure of the device. Pressure data was recorded digitally for the duration of the experiment. Figures 41a-c show the results from the pressure tests. As seen from these results, all three test sections survived pressure test up to 360 bar, the highest pressure that could be tested using the facility. Fig. 41d shows a picture of the three test articles upon pressure testing.

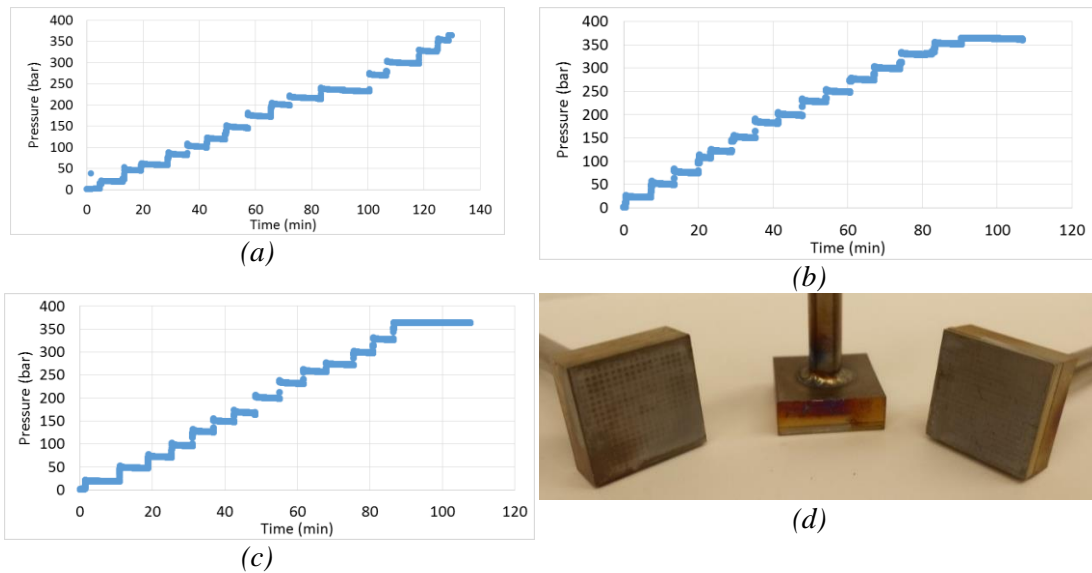
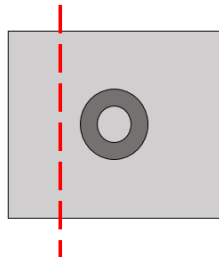


Figure 41. Pressure testing of SS test articles depicted in (a), (b), (c). Figure 39d shows pictures of the test articles upon completion of testing.

The test articles were sectioned upon completion of testing. Fig. 42a-c show top views of the test articles; the red lines indicate approximate locations of sectioning. Figures 42d-f show pictures of the test sections upon sectioning. As seen in Fig. 42f, significant buckling of the pins in the header region is observed for the case where the pin dimensions were the same in the microscale and plenum regions (Fig. 39d design). On the other hand, the bonds in the 2 mm and 1 mm wall thickness test articles with larger pins in the headers (Figs. 39a and 39b designs) appeared visually to have no defects. Optical profilometry was performed on all samples to determine the fluid path dimensions in the plenum and microscale pin regions. Sample optical profile maps are shown in Fig. 42g and 42h for Fig. 39a and Fig. 39d designs. It is important to note that the bonds in the microscale pin region are not compromised in the region where there is a fluidic gap in the header region (Fig. 42g). This observation provides confidence

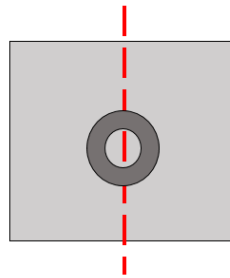
in using a 1 or 2 mm wall thickness between the header and microscale region in the larger scale sCO₂ HX.

*Large pin header, 1mm mid plate
(Fig. 39a design)*



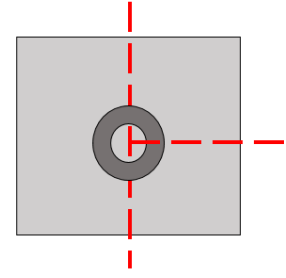
(a)

Large pin header, 2mm mid plate (Fig. 39b)

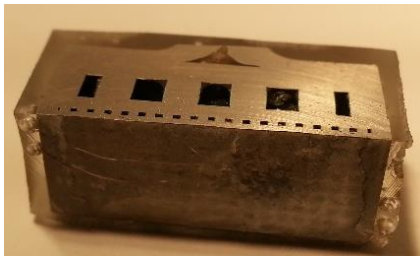


(b)

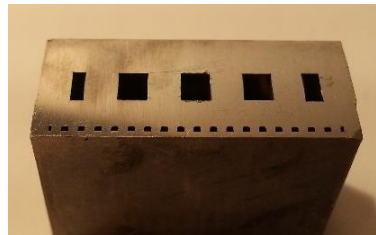
*Small pin header, 2mm mid plate
(Fig. 39d)*



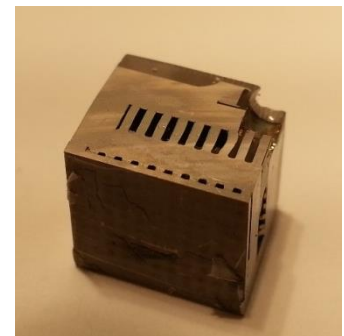
(c)



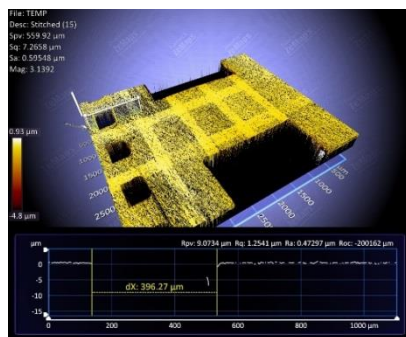
(d)



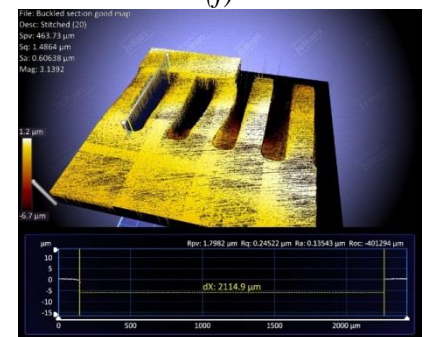
(e)



(f)



(g)



(h)

Figure 42. Sectioning and optical measurements of test sections upon completion of pressure testing

Table 6 presents detailed quantitative information on the profilometry measurements. Profilometry measurements were performed on two different regions in the microscale part and in one header region. Also provided are measurements of the bulk strain as measured before and after bonding using a digital caliper. This value can be contrasted with the local strain in the header and microscale regions. The local strain in these regions was estimated by optical profilometry before and after bonding. It is important to note that the bulk strain is not an accurate measure of the strain in the header or microscale channel regions. The strain in the header region is on the order of 14% while that in the microscale regions is larger at approximately 22%. Given that a bulk strain of 4.5% resulted in an excellent bond, we will likely go with a similar value of bulk strain but overdesign channel dimensions in the header and microscale regions to account for the decrease in channel dimensions upon bonding.

Table 6. Optical profilometry and bulk strain measurements

	Large pin header, 1mm mid plate (Fig. 37a design)			
	Pre-bond (mm)	After (mm)	Difference (mm)	Strain
Overall	7.4041	7.0866	0.3175	4.29%
Pin Type	Pre-bond (μm)	After (μm)	Diff (μm)	Strain
Header	2501.2	2177.2	324	12.95%
Micropin region, location 1	507.65	398.8	108.85	21.44%
Micropin region, location 2	499.07	396.27	102.8	20.60%
	Large pin header, 2mm mid plate (Fig. 37b design)			
	Pre-bond (mm)	After (mm)	Diff (mm)	Strain
Overall	8.382	8.0391	0.3429	4.09%
Pin Type	Pre-bond (μm)	After (μm)	Diff (μm)	Strain
Header	2556.9	2131.5	425.4	16.64%
Micropin region, location 1	486.94	365.13	121.81	25.02%
Micropin region, location 2	490.59	381.34	109.25	22.27%
	Small pin header, 2mm mid plate (Fig. 37d design)			
	Pre-bond (mm)	After (mm)	Diff (mm)	Strain
Overall	8.382	7.9883	0.3937	4.70%
Pin Type	Pre-bond (μm)	After (μm)	Diff (μm)	Strain
Header	2494.2	2114.9	379.3	15.21%

5.2 Design Revision

In addition to the 16 unit cell design, a new concept to reduce complexity and cost of the headers was developed. The basic idea was to relax the width of the unit cell and have it span the entire 8 cm width. The exploded view of the new concept is illustrated in Fig. 43 (a-b). A three layer concept was designed such that all the features could be made through conventional machining process. The overall width of unit cell in this design is 2 cm with identical length as of the test article i.e. 8 cm, see Fig. 43c. As is shown in Fig. 43c, the flow would enter into the flux receiver plate from one of the distributor channels in the middle of test article and split into two flow paths, pass across the microscale pin fins and exit the receiver regions through adjacent exit slits that lead to the upper plenum. (red arrows in Fig. 43d). The new concept provides flow distributor and collector channels all in one layer.

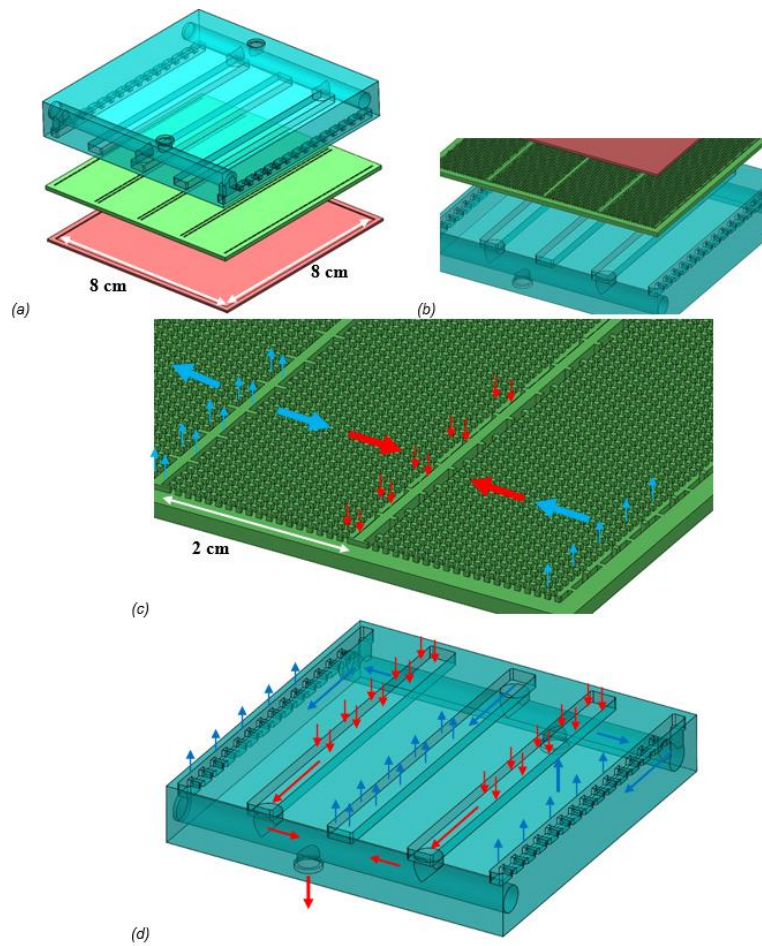


Figure 43. (a-b) Exploded views of the new concept for $8 \times 8 \text{ cm}^2$ test article. (c) Top view of the flux receiver plate with guiding arrows which shows the flow direction across the microscale pins. (d) Top view of the headering section with blue arrows showing the inflow in distributor channels and red arrows showing outflow in collector channels.

In order to have uniform flow distribution by the header into the pin finned receiver plate the pressure drop in the distributor headers needs to be significantly smaller than that of across the pin fin arrays. Fluid passage in a concept with 2 unit cells is shown in Figure 44. The pin finned receiver plate is shown as a micro gap for simplicity. The dimensions in distributor headers were selected based on two criteria. First in order to help better flow distribution the headers should provide fluid volume larger than that of contained by the receiver plate (more than 5 times). Second they can structurally

withstand the pressure difference between 200 bar internal pressure and atmospheric outside pressure. To address the latter the side distributor headers were designed with strengthen ribs in order to reduce the amount of stress. The FEA analysis was performed on the side distributor header, shown in Fig. 45a, to ensure the maximum stress was below yield stress of the Haynes 230. The Von-Mises equivalent stress distribution in the modelled distributor header is shown in Fig. 45b.

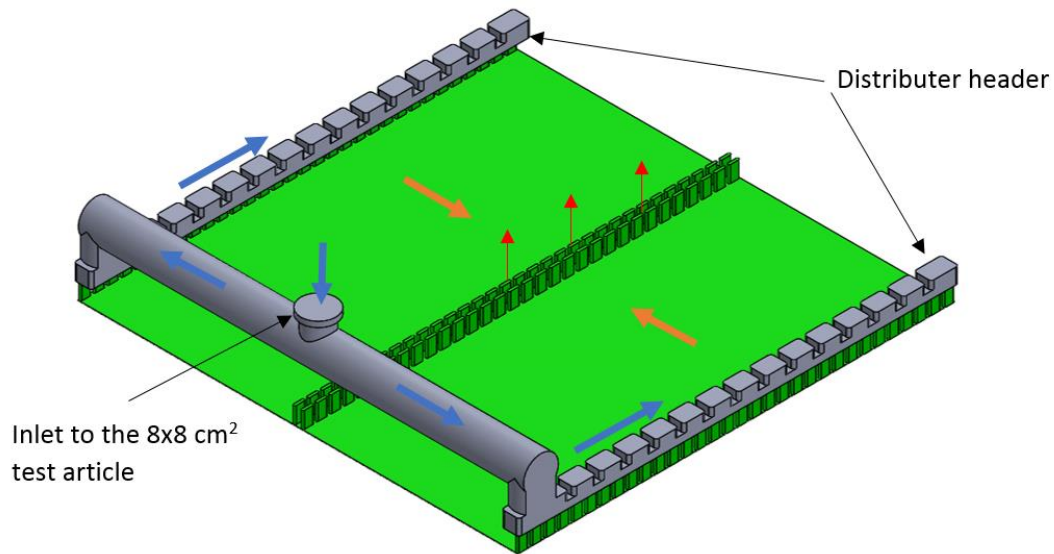


Figure 44. Fluid passage in a concept with 2 unit cells with a micro gap as simplified receiver plate

The approved design for the side distributor header showed pressure drop about 14.5 kPa between the inlet into the side header and the farthest pocket which takes the fluid into the receiver plate. The pressure drop was calculated with assumption that supercritical CO₂ enters into the test section with 500 °C and 200 bar and exits at 650 °C with mass flow rate high enough to dissipate 100 W/cm² incidental heat flux. As mentioned earlier to ensure having uniform flow distribution across the receiver plate

the pressure drop that fluid experiences with passing along the pin finned unit cell should be larger (~ 10 times) than the pressure drop in the distributor header. Either increasing the width of unit cell or decreasing the height of pin fins would help in increasing the pressure drop.

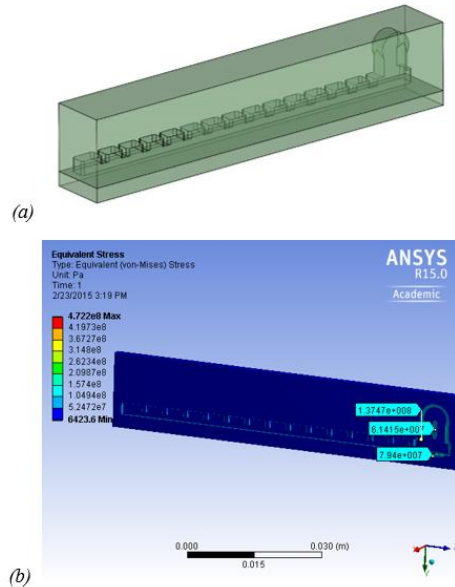


Figure 45. (a) The side distributor header modelled with Ansys Mechanical (b) Von-Mises equivalent stress distribution in the model with 200 bar internal pressure and atmosphere outside pressure.

Ansys Fluent was used to perform simulations to determine the right dimensions for the unit cell. The simulated fluid passage model in Fluent is shown in Fig. 46a. The model is a section of the unit cell with adjusted mass flow rate in order to dissipate 100 W/cm^2 and with fluid temperature-pressure conditions at the inlet and outlet similar to what was assumed for the entire $8 \times 8 \text{ cm}^2$ test section. The pressure contour maps in the simulated model is shown in Fig. 46b. For the 4 cm wide unit cell (39.5 mm fluid passage width) and 200 μm pin fin height the simulations showed about 176.5 kPa pressure drop which this fulfills the ~ 10 times larger DP criteria used for determining

the dimensions of the unit cell in respect to the distributor header design. The square pin fins had 500 μm side width and space with 1000 μm pitch in both transverse and longitudinal directions. Hence the final design for the test section had 2 unit cells with 8 cm length and 4 cm width.

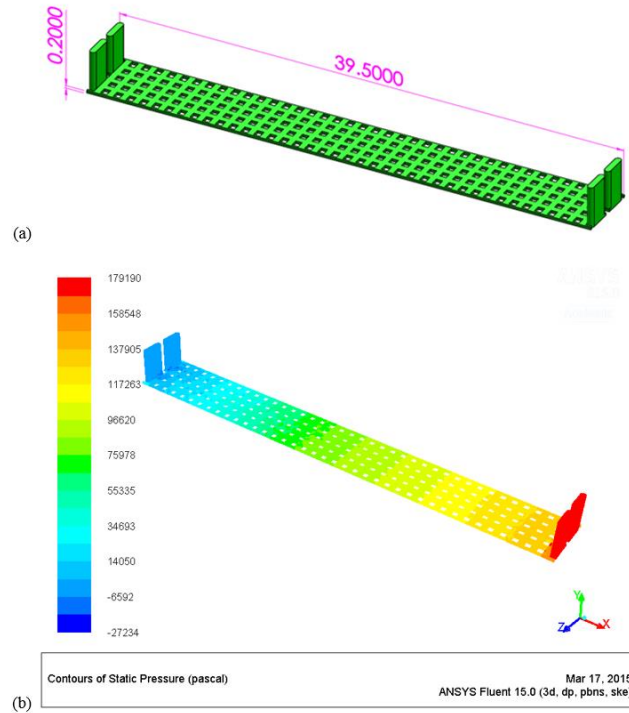


Figure 46. (a) Simulated fluid passage model in Fluent as a section of a unit cell (b) Pressure contour maps in the simulated model for SCO_2 working with required mass flow rate to dissipate 100 W/cm^2 incidental heat flux.

The exploded view of the finalized design which was sent out for fabrication is shown in Fig. 47a (from top) and b (from bottom). The laminates of the fabricated test section also are shown in Fig. 47c. The surface profilometry was performed on the fabricated plates to ensure the dimensions of the machined parts are in agreement with the designed model. A measurement from the pitch distance between two adjacent pin fins by the Zygo 3D surface profiler is shown in Fig. 48.

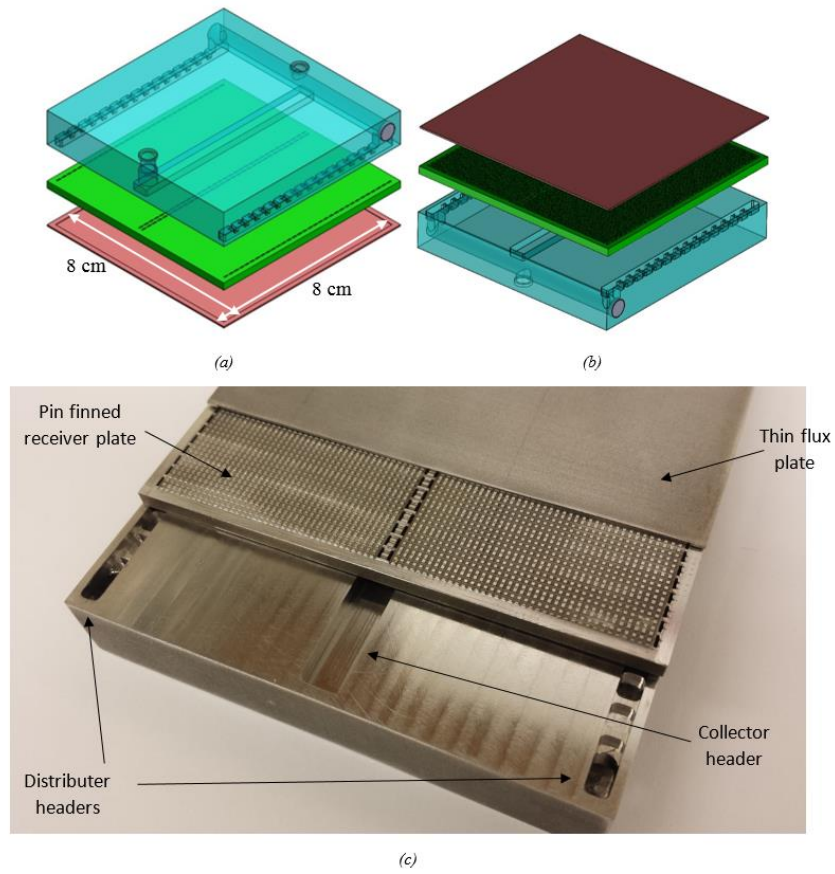


Figure 47. (a and b) Exploded view of the finalized design from top and bottom (c) The laminates of the fabricated test section

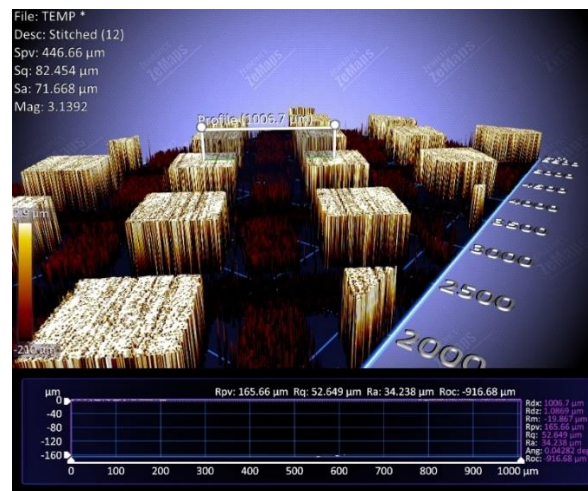


Figure 48. Surface profilometry from the receiver plate showing the pitch distance between two adjacent pin fins

Before bonding the machined parts, the plates were sent out for electroless nickel plating. The coated plates then were diffusion bonded by Refrac Systems. A picture of the bonded test section is depicted in Fig. 49. Mark up of the pin fins in the receiver plate could be seen clearly on the back side of the flux plate. This conveys that diffusion bond has occurred between all pin fins top and the flux plate. In order to provide inlet and outlet to the test section two quarter inch outer diameter Haynes 230 tubes were welded on top of the provided holes in the test section's header. The initial pressure testing with 5.5 bar pressurized air unfortunately showed significant leaks from the edges of the test section and the welded plug holes for the header connection channels.



Figure 49. Diffusion bonded 8x8 cm² test section showing apparent registration of pin features. Welds on the edges are from attempts to seal the bond seams after discovery of leaks.

Attempts were undertaken to eliminate the potential drawbacks found in the design of first version of the test section which resulted in the pressure testing failure in designing a new modified IR test article. Surface finish on the side edges of the receiver plate

where the bond occurs between receiver plate and the flux plate is of a critical importance. The approach of wire EDM machining on the receiver plate to make the micro pin fins resulted in several imperfections on the side edges. Visible grooves with depth even as high as 20 μm were formed on several spots on the side edges of the receiver plate as the result of the wire touch down. Although in the first IR, prior to plating and then diffusion bonding, polishing was performed with fine grit sand paper, but the imperfections could not be completely polished out. The exploded view of the revised IR is shown in Fig. 50a. From Fig. 50b one can see that the pin fins' base height is different than the level of the edges. This will provide enough room for the wire to do the machining of the pin fins without touching the polished edges. The second major design problem was determined in having all distributor and collector headering machined out in one plate in the 3-layer test section design. As it could be seen in Fig. 47a in order to split the inlet flow into the side distributor plenums a long hole was needed to be drilled from the side of thick (14 mm) header plate. The hole then was supposed to be capped off with welding. The thermal shock (expansion and contraction) as a result of welding process on the side hole showed a significant stress on the bonded laminates. This could even lead into the local bond breakage. The modified design as it can be seen in Fig. 50a has 4 layers. The channel for splitting the inlet flow between the side distributor headers can be machined in the most top plate without the need for any welding processes. Figure 51 (a-f) show the final IR lamina prior to plating and the bonded IR with inlet and outlet tubes welded on.

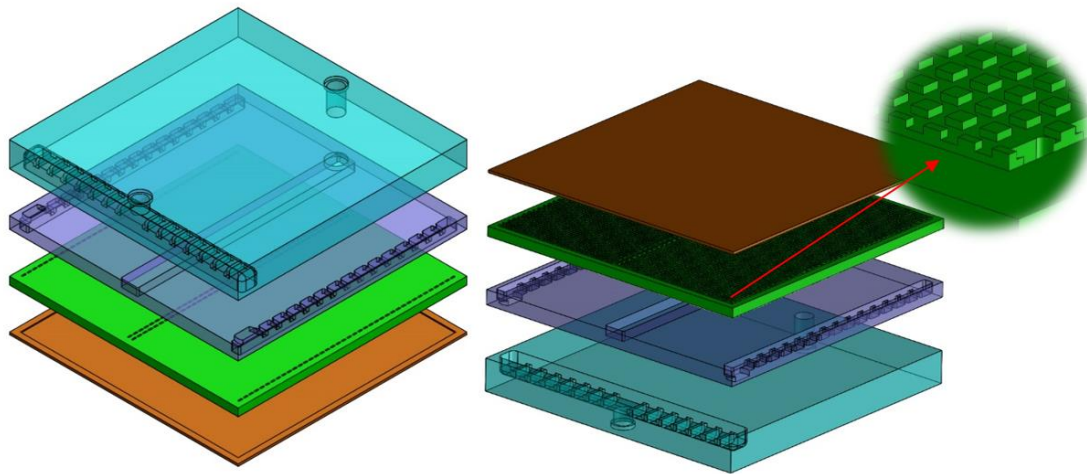
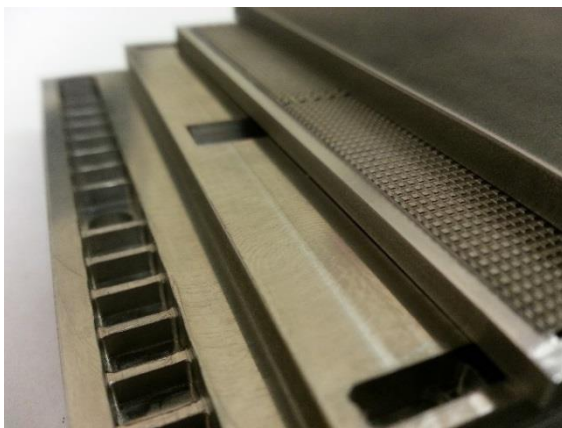
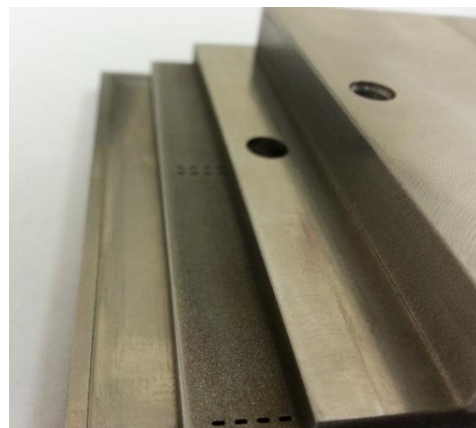


Figure 50. Exploded view of the modified design sent out for fabrication a) from top and b) from bottom with a zoom in showing the difference in the height of pin fins' base and edges on the receiver plate



(a)



(b)



(c)



(d)



Figure 51. (a) Revised design after fabrication stack and offset to view layers, (b) Flipped-revised design after fabrication stack and offset to view layers, (c) Aligned stack, (d) Post bond stack, (e) Detail view of bond interface, (f) Final IR design with inlet/outlet tubes weld in place

5.3 Integrity Testing

The pressure test facility used for burst testing of 2x2 cm² samples was modified to be able to pressure test the IR test section at room temperature. The objective of pressure testing is to test the test section mechanical strength after diffusion bonding up to the designed working pressure (i.e. 200 bar), in accordance to ASME Section VIII Div. 1 code. As is shown in Fig. 52, the test section is pressurized using a hydrostatic hand pump with water. The pump can generate pressure up to 410 bar (6000 psi) in the fluidic lines. An air-tight stainless steel pressure test chamber half filled with water is used to ensure the safety of operator. The line pressure is monitored by an ASHCROFT absolute pressure transducer calibrated for the working pressure range of the pump. The IR test section is then moved for integrity testing in a separate test facility at 200 bar and 750 °C surface temperature as shown in Fig. 53. A 6000 psi nitrogen tank and

regulator combination provides up to 320 bar line pressure. The IR test section was well insulated with two Omega type K thermocouples lining the perimeter just inside of the insulation to monitor and ensure the desired surface temperature of 750°C. Pressure is monitored by the same ASHCROFT absolute pressure transducer. The test procedure was the same as the LSR testing as described in Chapter 3.1.

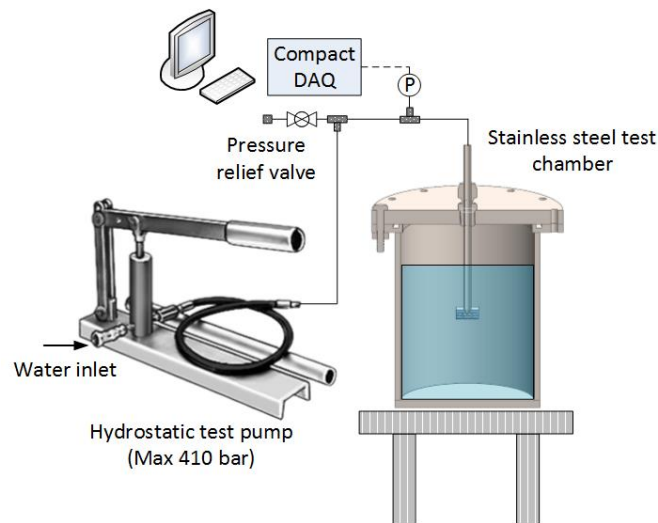


Figure 52. Schematic of assembled pressure testing facility

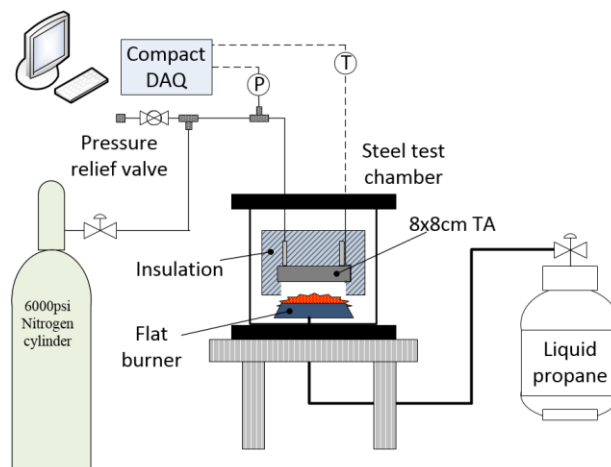


Figure 53. Schematic of assembled temperature and pressure testing facility

Figure 54 shows the results of the IR test article under the hydrostatic pressure test. After the successful pressure test, the IR was well insulated and installed into the temperature and pressure test facility. The insulation of the IR is shown in Fig. 55.

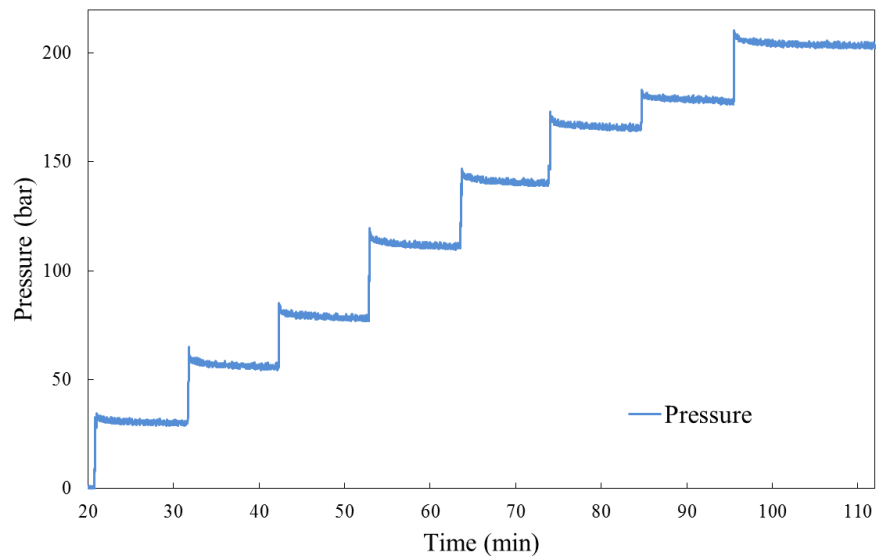


Figure 54. Results of the IR test article pressure test.



Figure 55. Two views of the insulation setup for the IR pressure test at temperature.

Results from the static pressure testing at temperature is presented in Fig. 56. The inability to reach the operational temperature of 750°C shouldn't diminish the

effectiveness of the design to with stand the operational conditions. Figure 57 shows the intact IR post testing.

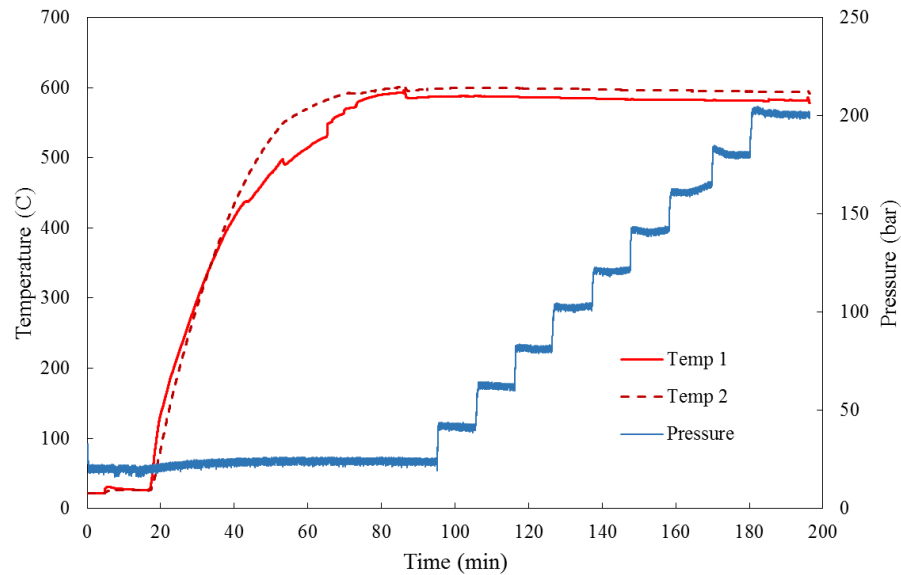


Figure 56. Static pressure testing at temperature of the IR test article

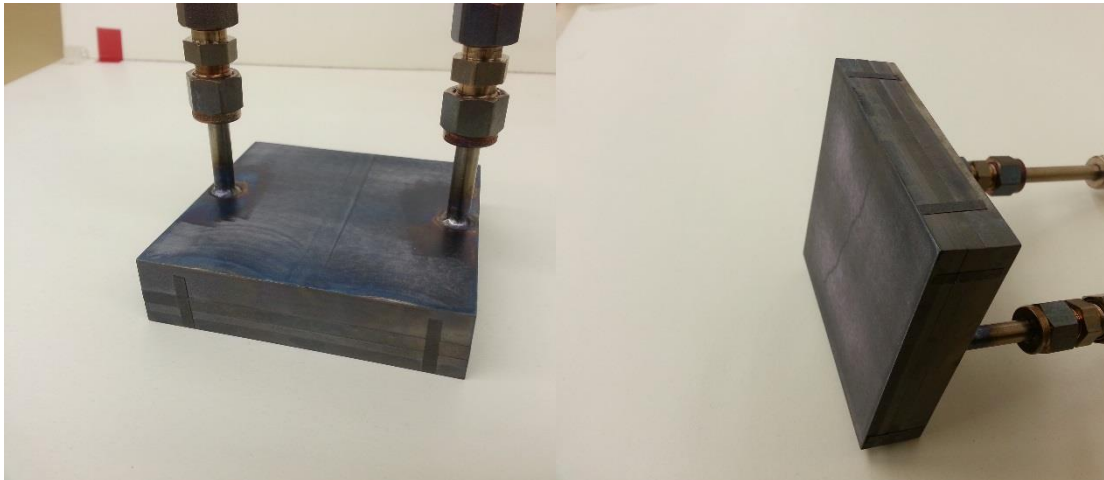


Figure 57. IR test article after structural verification testing.

After the initial integrity test the device was sent to a machinist to have to top flux plate ground down to approximately 500 um thick. The IR was manufactured this way to

ensure adequate bonding between the pin features and the flux. After the machining process, the facility shown in Fig. 53 was used again. Figure 58 shows the results of the pressure test at room temperature. Figure 59 presents the pressure test at operational temperatures, again a surface temperature of only 600C was achieved, but the pressure was brought up to a maximum of 220 bar.

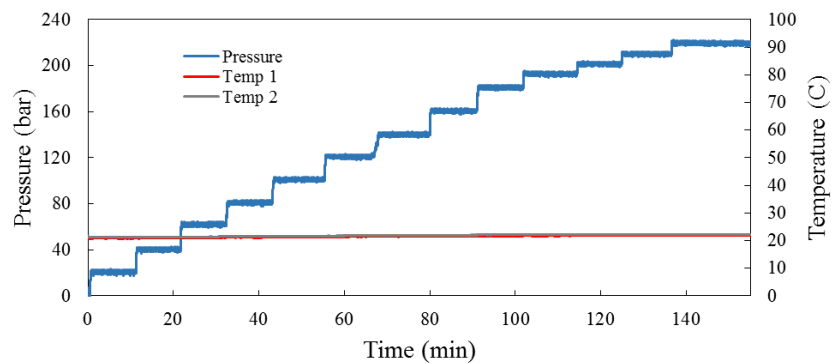


Figure 58. Pressure testing after top plate has been machined down to approximately 500um

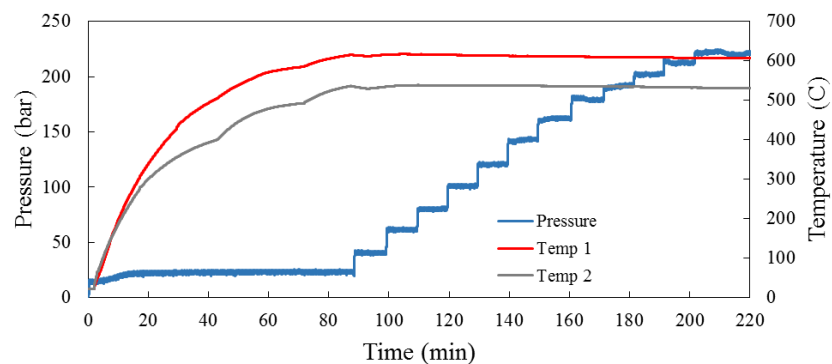


Figure 59. Pressure testing at high temperature after top plate has been machined down to approximately 500um

Images below show the surface discoloration of the test article after pressure testing at temperature, Fig. 60. There were no signs of deformation. After the structural testing, the article was prepped for Pyromark 2500 coating. Since the device will only see

temperatures below 400C, it was assumed the coating should remain intact and retain the manufactures specified spectral properties, Fig. 61.

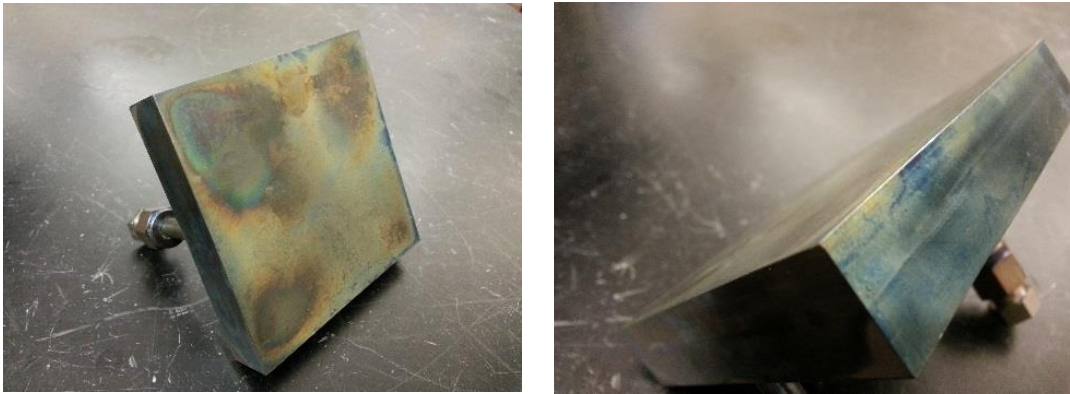


Figure 60. Test article surface condition after structural testing. Notice discoloration, but no visible signs of deformation.

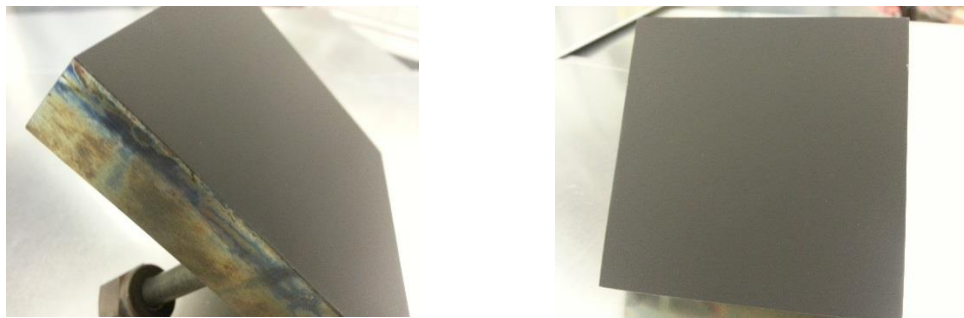


Figure 61. Pyromark 2500 Coating applied prior to IR imaging and data collection

The test article was then installed into the infrared imaging facility as shown in Fig. 62. Subcritical CO₂ gas was used as the heat transfer fluid. The CO₂ flow was controlled via high pressure regulator in conjunction with a fine turn needle valve. The preheater used in sCO₂ testing was used to heat the gas prior to entering the test article. Rope heaters and a water bath were used to ensure the CO₂ was gaseous prior to entering the preheater.

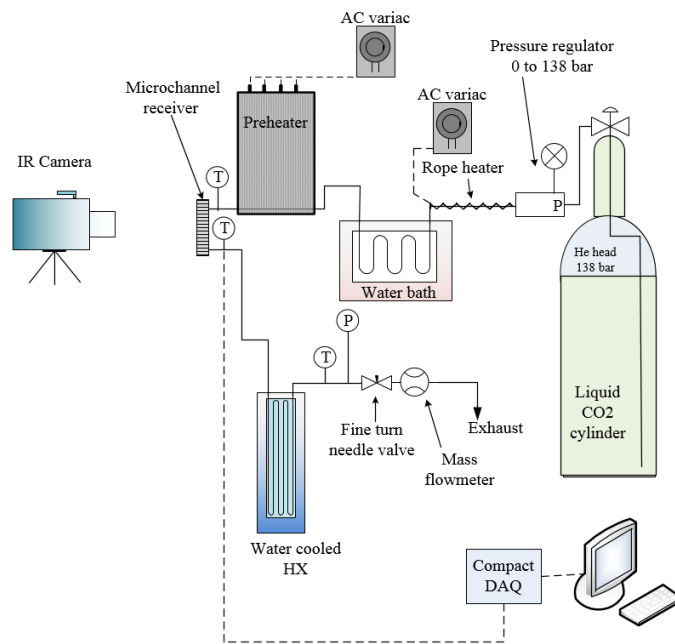


Figure 62. Schematic of infrared imaging facility

To understand the infrared images, the orientation of the test article is important. Shown in Fig. 63, is the header orientation (Fig. 63a) as well as an exploded view of the lamina in reference to the camera viewing direction (Fig. 63b). As shown the main inlet distribution header runs vertically, shown by the dotted lines in the left of Fig. 63a. This header distributes the flow to the secondary inlet headers that run horizontally. The single outlet header also runs horizontally through the center of the test article.

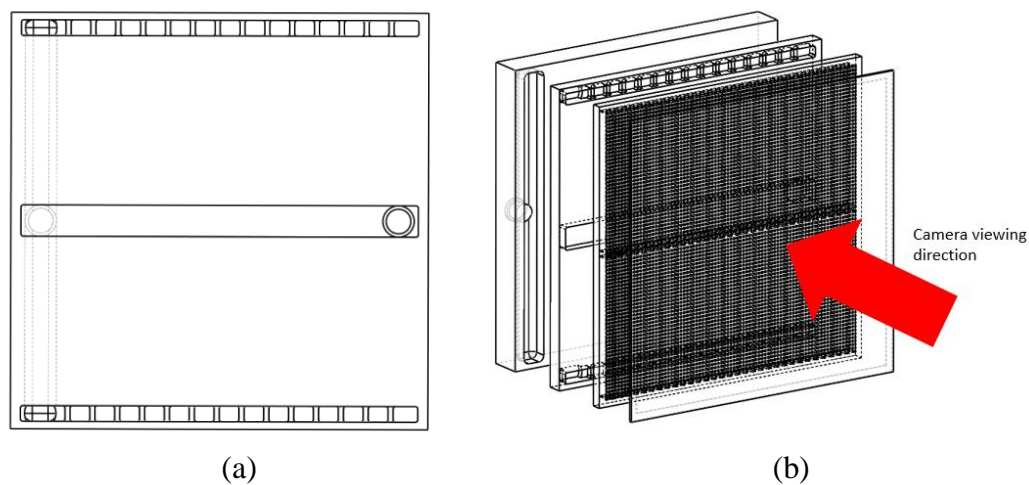


Figure 63. (a) Test article header orientation (b) exploded view of the lamina in reference to the infrared camera viewing direction

The IR camera was calibrated at room temperature. An Omega type K surface thermocouple was attached to the surface of the test article as shown in Fig. 64 and IR images were recorded. An average reading of 30 seconds of the surface thermocouple was then compared to the surface temperature. These results are shown in Fig. 10 in which the “X” mark the pixel selected for comparison and the lettering coincides with the values in the table. The pixel surface temperature from the camera and the thermocouple reading were found to be within 0.5°C of one another.

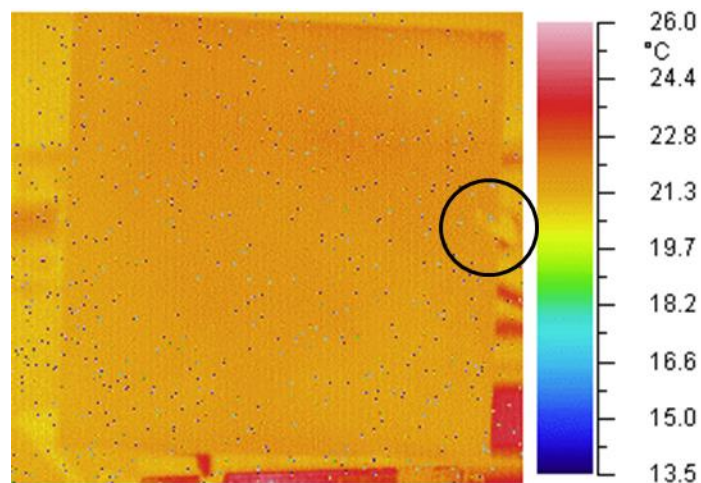
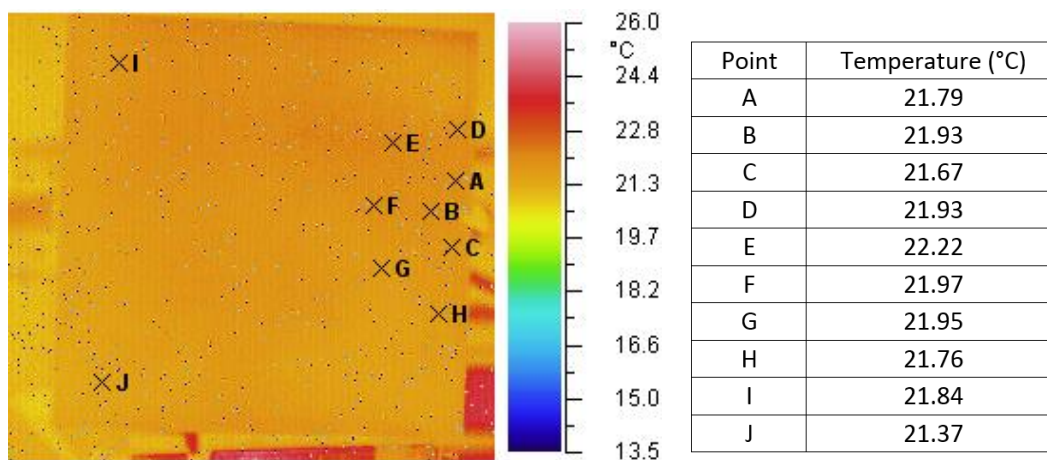


Figure 64. Location of thermocouple for room temperature calibration



Averaged Omega type K thermocouple reading - 22.25 °C

Figure 65. Room temperature IR camera calibration

After calibration, the test article was then well insulated. Gas flow rates were held constant and inlet gas temperatures were varied between 100-250°C. Results of the 100°C flow are presented in Fig. 65. Figure 66a is the infrared image and the 3 vertical lines are selections of pixel data. Figure 66b is the plot of these three lines of data. A pixel number of “0” represent the starting point, or “X”, of the line in the image. This same format is then repeated in Fig. 67 of the 250°C flow.

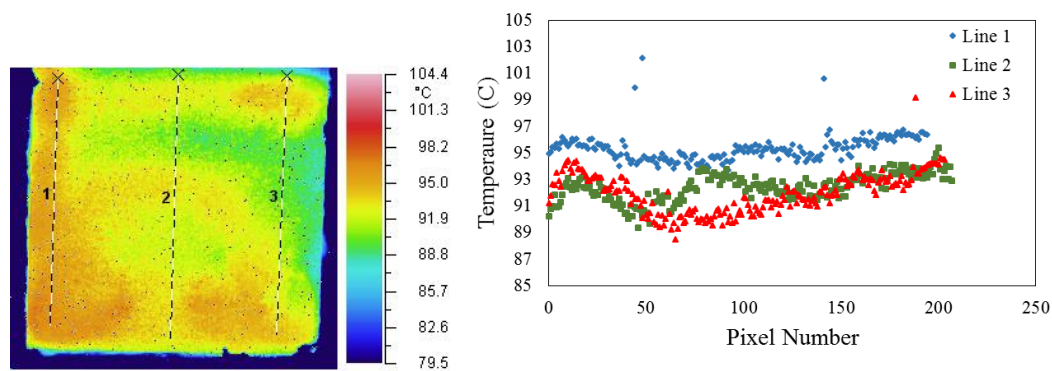


Figure 66a. Infrared image of the 100°C flow test

Figure 66a. Plot of the data lifted from the 100°C infrared image

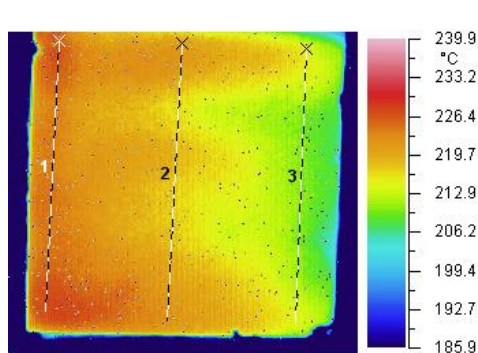


Figure 67a. Infrared image of the 250°C flow test

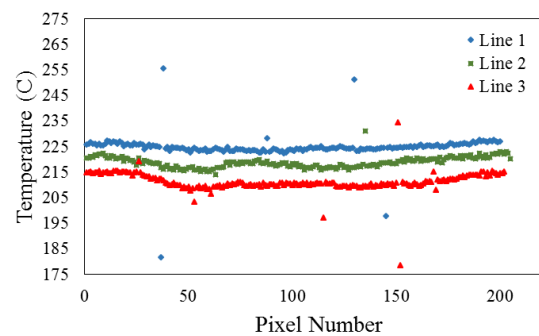


Figure 67a. Plot of the data lifted from the 250°C infrared image

Based on the above results, there seems to be a variation in temperature across the width of the pin fin array of approximately 10°C or approximately less than 5 percent of inlet temperature, which is significant. From this temperature variation, it can be inferred that the flow is unevenly distributed between the two headers. The lower header, as depicted in Fig. 63a, is allowing more flow through the lower pin array. This is indicated but the higher temperatures in the lower section as shown by both Fig. 66a and Fig. 67a. This flow maldistribution can be rectified by increasing the resistance in the pin array, for example, increasing the distance between the inlet header and the outlet header or by decreasing the pin height.

6. Conclusion

Characterization of a microchannel solar thermal receiver for sCO₂ was presented. The receiver design was based on conjugate CFD and heat transfer simulations as well as thermo-mechanical stress analysis. Two LSRs with a 2x2 cm² absorber area were fabricated and experimentally characterized. Lab-scale experiments were used to successfully demonstrate the receiver integrity at the design pressure of 125 bar at 750°C surface temperature. The thermal performance of the lab scale receiver test articles were also successfully conducted. The results indicate that, for a fixed exit fluid temperature of 650°C, increase in incident heat flux results in an increase in receiver and thermal efficiency. At a fixed heat flux, efficiency decreased with an increase in receiver surface temperature. The ability to absorb flux of up to 100 W/cm² at thermal efficiency in excess of 90 percent and exit fluid temperature of 650°C using the microchannel receiver while accounting for conductive heat loss through insulation was demonstrated. The successful test of the lab-scale receiver facilitated the design, fabrication, and structural testing of an 8x8 cm² integrated receiver. Structural testing at 600°C and 200 bar proved a device can be scaled up with more effective material usage and withstand operational conditions. Infrared imaging indicated the possibility of less than ideal flow distribution with in the pin array. Solutions to the maldistribution were noted. Flow conditions aside, the effectiveness of microstructures utilized in the field of concentrated solar energy production was demonstrated in addition to the ability to physically scale up the receiver design.

7. References

- [1] J.E. Pacheco, "Final Test and Evaluation Results from Solar Two Project," Paper No. SAND2002-0120, Sandia National Laboratory, PO Box 5800, Albuquerque, NM, 2002.
- [2] G.J. Kolb, "An Evaluation of the Next Generation of High Temperature Molten Salt Power Towers," Paper No. SAND11-9320, Sandia National Laboratory, PO Box 5800, Albuquerque, NM, 2011.
- [3] United States Department of Energy, Energy Efficiency and Renewable Energy Website, July 7, 2015
(https://www.eeremultimedia.energy.gov/solar/photographs/solar_two_tower_system)
- [4] U.S. Department of Energy, "High Efficiency Receivers for Supercritical Carbon Dioxide Cycles," Paper No. DOE/GO-102012-3661, SunShot Concentrating Solar Power Project Description.
www.solar.energy.gov/SunShot/csp_SunShotrnd_brayton.html.
- [5] Romero, M., Buck, R., and Pacheco, J. E., 2002, "An Update on Solar Central Receiver Systems, Projects, and Technologies," *Journal of Solar Energy Engineering*, Vol. 124, pp. 98-108.
- [6] D.B. Tuckerman, R.F.W. Pease, "High Performance Heat Sinking for VLSI," *IEEE Electron Device Letters*, Vol. 2, pp. 126-129, 1981.
- [7] Kosar and Y. Peles, "Thermal-hydraulic Performance of MEMS-based Pin Fin Heat Sink," *J Heat Trans*, Vol. 128, No. 2, pp. 121-132, 2006.
- [8] H.H. Bau, "Optimization of Conduits' Shape in Micro Heat Exchangers," *Int J Heat Mass Trans*, Vol. 41, pp. 2717-2723, 1998.
- [9] D.V. Pence, "Reduced Pumping Power and Wall Temperature in Microchannel Heat Sinks With Fractal-Like Branching Channel Networks," *Microscale Therm Eng*, Vol. 6, pp. 319-330, 2002.
- [10] J.A. Federici, D.G. Norton, T. Brüggemann, K.W. Voit, E.D. Wetzel, and D.G. Vlachos, "Catalytic Microcombustors with Integrated Thermoelectric Elements for Portable Power Production," *J Power Sources*, Vol. 161, No. 2, pp. 1469-1478, 2006.

- [11] D.B. Haley and V. Narayanan, "Performance Characterization of a Microscale Hydrogen Combustor, Recuperator and Oil Heat Exchanger," Paper No. IMECE2011-64176, in Proceedings of ASME International Mechanical Engineering Congress and Exposition, Denver, Colorado, November 11-17, 2011, Vol. 4, pp. 1283-1293, ISBN: 978-0-7918-5490-7.
- [12] R. L. Webb, "Next Generation Devices for Electronic Cooling With Heat Rejection to Air," J Heat Trans, Vol. 127, pp. 2-10, 2005.
- [13] A.Y. Tonkovich, J.L. Zilka, M.J. LaMont, Y. Wang, and R.S. Wegeng, "Microchannel Reactors for Fuel Processing Applications. I. Water Gas Shift Reactor," Chem Eng Sci, Vol. 54, Nos. 13-14, pp: 2947-2951, 1999.
- [14] Y. Joshi and X. Wei, "Keynote Lecture: Micro and Meso Scale Compact Heat Exchangers in Electronics Thermal Management--Review," in Proceedings of the 5th International Conference on Enhanced, Compact, and Ultra-Compact Heat Exchangers: Science, Engineering, and Technology, R.K. Shah, M. Ishizuka, T.M. Rudy, and V.V. Wadekar, eds., Engineering Conferences International Symposium Series, Whistler, British Columbia, Canada, September 11-16, 2005, Vol. P06, 2005. <http://dc.engconfintl.org/heatexchangerfall2005/18>.
- [15] W. Qu and I. Mudawar, "Flow Boiling Heat Transfer in Two-Phase Micro-channel Heat Sinks, I. Experimental Investigation and Assessment of Correlation Methods," Int J Heat Mass Trans, Vol. 46, No. 15, pp. 2755-2771, 2003.
- [16] K. Sai, X.S. Mylavarapu, R.N. Christensen, R.R. Unocic, R.E. Glosup, M.W. Patterson, "Fabrication and Design Aspects of High-Temperature Compact Diffusion Bonded Heat Exchangers," Nucl Eng Des, Vol. 249, pp. 49-56, 2012. <http://dx.DOI.org/10.1016/j.nucengdes.2011.08.043>.
- [17] L. Xiuqing, D. Kininmont, R. Le Pierres, and S.J. Dewson, "Alloy 617 for the High Temperature Diffusion-Bonded Compact Heat Exchangers," Paper 8008, in Proceedings of ICAPP '08, Anaheim, CA, June 8-12, 2008.
- [18] L. Xiuqing, R. Le Pierres and S.J. Dewson, "Heat Exchangers for the Next Generation of Nuclear Reactors," Paper 6105, in Proceedings of ICAPP '06, Reno, NV, June 4-8, 2006.
- [19] S. Leith, D. King, and B.K. Paul, "Toward Low-Cost Fabrication of Microchannel Process Technologies-Cost Modeling for Manufacturing Development: High Throughput and Compact Chemical Processing Technologies," in Proceedings of 2010 AIChE Annual Meeting, Salt Lake City, UT, November 7-12, 2010.

- [20] B. Lajevardi, S.D. Leith, D.A. King, and B.K. Paul, "Arrayed Microchannel Manufacturing Costs for an Auxiliary Power Unit Heat Exchanger," in Proceedings of IIE Annual Conference, Reno, NV, May 21-25, 2011.
- [21] P. Paulraj and B.K. Paul, "Metal Microchannel Lamination Using Surface Mount Adhesives for Low-Temperature Heat Exchangers," *J Manufacturing Processes*, Vol. 13 No. 2, pp. 85-95, 2011. DOI:10.1016/j.jmapro.2011.01.001.
- [22] R.S. Wegeng, D.R. Palo, R.A. Dagle, P.H. Humble, J.A. Lizarazo-Adarme, S. Krishnan, S.D. Leith, C.J. Pestak, Q. Songgang, B. Boler, J. Modrell and G. McFadden, "Development and Demonstration of a Prototype Solar Methane Reforming System for Thermochemical Energy Storage Including Preliminary Shakedown Testing Results," in Processings of the Ninth Annual International Energy Conversion Engineering Conference, July 31-August 3, 2011. DOI: 10.2514/6.2011-5899.
- [23] R.S. Wegeng, W. TeGrotenhuis, and J.C. Mankins, "Solar Thermochemical Production of Fuels," in Proceedings of the 5th International Energy Conversion Engineering Conference, St. Louis, MO, June 25-27, 2007. DOI: 10.2514/6.2007-4709a.
- [24] D. Peterson, S.V. Apte, V. Narayanan, and J. Schmitt, "Numerical Modeling of Mini/microchannel Reactor for Methane-steam Reforming," Paper No. FEDSM-ICNMM2010-31192, in Proceedings of ASME 2010 Fluids Engineering Summer Meeting, Montreal, Quebec, Canada, August 1-5, 2010.
- [25] K. Drost, B. Eilers, D. Peterson, S. Apte, V. Narayanan, and J. Schmitt, J., 2011, "Detailed Numerical Modeling of a Microchannel Reactor for Methane-steam Reforming," Paper No. AJTEC2011-44664, in Proceedings of the ASME/JSME 8th Thermal Engineering Joint Conference 2011, Honolulu, HI, March 13-17, 2011, Vol. 2, pp. 669-682.
- [26] K. Drost, S.V. Apte, J. Schmitt, and V. Narayanan, "Design of a Microchannel based Solar Receiver/Reactor for Biofuel Processing," Paper No. ISHMT-USA-018, in Proceedings of the 21st National and 10th ISHMT-ASME Heat and Mass Transfer Conference, Chennai, India, December 27-30, 2011.
- [27] Rymal, C. J., 2015, "Numerical Design of a High-flux Microchannel Solar Receiver", MS Thesis, Oregon State University, Corvallis, OR, USA.
- [28] Haynes International Inc., "Haynes 230 Alloy Specification Sheet", (www.haynesintl.com/pdf/h3000.pdf)

- [29] LA-CO Industries Inc., “Pyromark 2500 Flat Black Testing Information Sheet”, January 17, 2011 (www.tempil.com)

- [30] Moffat, R., 1988, “Describing the Uncertainties in Experimental Results,” *Experimental Thermal and Fluid Science*, 1(1), pp. 3-17.

8. Appendix

This appendix covers a detailed study of the Pyromark coating brought on by the issues that occurred during thermal testing of LSRs. In the later sections of the appendix are axillary part drawings, test loop schematics, and images.

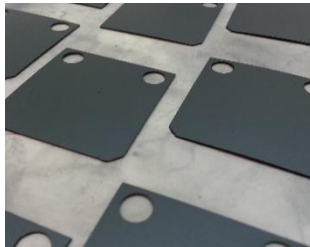
8.1 In Depth Coating Study – Pyromark 2500

In an effort to overcome the degradation of Pyromark 2500 and the increased reflective losses the Department of Energy facilitated a partnership with Sandia National Lab (SNL) for their new application approach for Pyromark. Sandia was contacted about the details of the application process. The attempts to use the SNL application approach initially were not successful. The paint application and cure process was provided by SNL. This process was followed as closely as possible with few variations from SNL's proscribed process. The tests were conducted using Haynes 230, both bare and ENi coated surfaces. Surface preparation was done using glass bead media with 60-120 mesh and the paint was applied using a Paasche TG-SET Talon Airbrushing System operating at 35psi. Sandia used ANSI 316L stainless steel, garnet media with 60-120 mesh, and an unspecified model of Binks paint gun. Surface of samples were prepared and chemical cleaning steps were followed. Some samples were not blasted or blasted and then hand sanded with varying grits in order to assess the effect of surface roughness. After the paint was applied the samples were air cured for 18 hours and then moved to the oven. The oven used for the cure cycle is a CM Rapid Temp lab furnace with a 1600°C max continuous run temperature and inert nitrogen atmosphere. Oven

temperature and ramp cycles are controlled using a Eurotherm 2404 temperature controller. Oven cure temperature cycle for max operating temperature of $\sim 750^{\circ}\text{C}$ is as follows:

- i. Heat to 120°C , dwell for 2 hrs
- ii. Heat to 250°C , dwell for 2 hrs
- iii. Heat to 540°C , dwell for 1 hr
- iv. Heat to 700°C , dwell for 1 hr
- v. Heat to 800°C , dwell for 1 hr
- vi. Cool to 25°C at $5^{\circ}\text{C}/\text{min}$

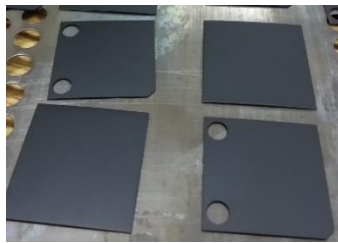
Upon visual inspection of samples the paint clearly showed poor adhesion (See Figure A1). A second round of samples was prepared along with 304 stainless steel pieces in order to assess if the result was due to process error or substrate material interaction. The result of this run showed successful adhesion on the stainless steel and again poor adhesion to the Haynes 230. Beyond media blasting, surface roughness showed to have minor positive effects. Haynes 230 non-plated samples showed slightly better adhesion, but still not satisfactory.



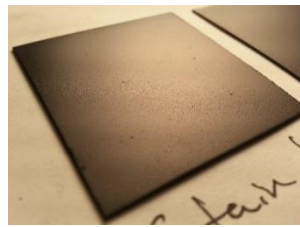
Pre-oven cure round 1



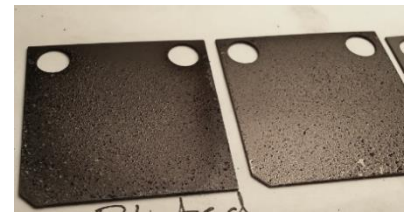
Post- oven cure round 1



Pre-oven cure round 2



Post cure 2 Stainless 304

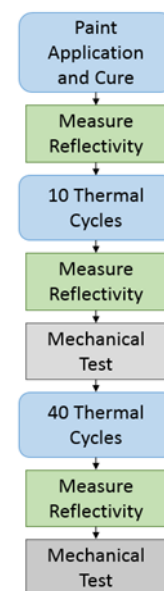


Post cure 2 Haynes 230 ENi plated

Figure A1. Initial Pyromark cure process results

The cause of poor Pyromark adhesion has been narrowed down to cure environment. After consulting SNL addressing the above results, two major conditions were changed. First the cure cycle must occur under an atmospheric air environment not an inert nitrogen environment. Second is to remove the final temperature step of 800°C. This was included previously to cure above proposed operational conditions desired in sCO₂ operations. The proposed changes produced a robust Pyromark 2500 coating on both ss316 and Haynes 230 test coupons.

After the initial cure reflectivity measurements were taken using spectrophotometer (JASCO UV-670). The samples were then cycled and the reflectivity and mechanical robustness was measured. The oven was brought to 750°C as rapidly as possible, in this case it was approximately 8min. The temperature was then held for 15min to ensure complete soak of the coupons. After the soak the temperature was dropped as rapidly as permitted. The cooling time was set to 30min to reach 50°C. Once cooled the cycle automatically repeated. Reflectivity measurements were taken of each sample after curing and after each set of thermal cycling. Results for each sample are provided in Figs. A2



and A3. Figure A5 is a comparison of both samples after 50 thermal cycles. A plot of the terrestrial solar insolation based on the ASTM G173 data set is provided to determine the greatest contribution section of reflectivity.

Every sample showed signs of increasing reflectivity after thermal cycling. From initial cure to after 10 cycles showed the largest increase and after 40 more cycles the increase in the reflectivity was minimal. The dip in Pyromark's reflectivity nearly matches the peak in solar insolation thus indicating an ideal reflectivity for a solar absorber coating.

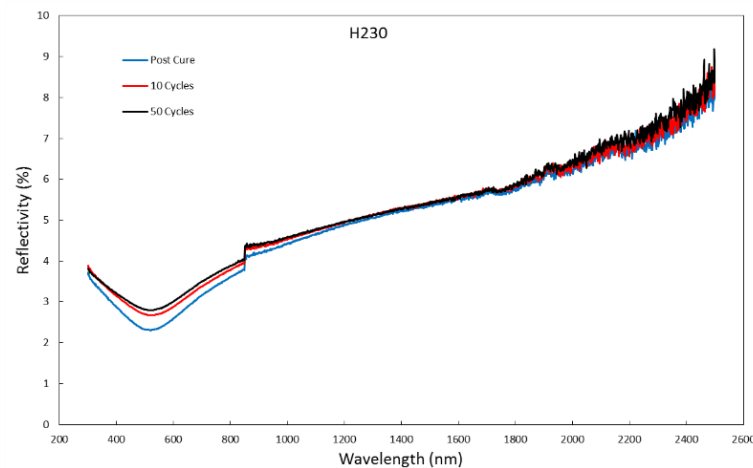


Figure A2. Pyromark 2500 on Haynes 230, reflectivity as a function of wavelength

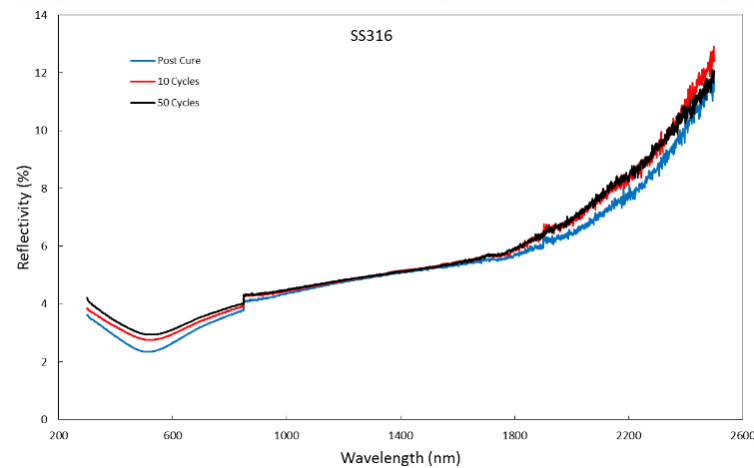
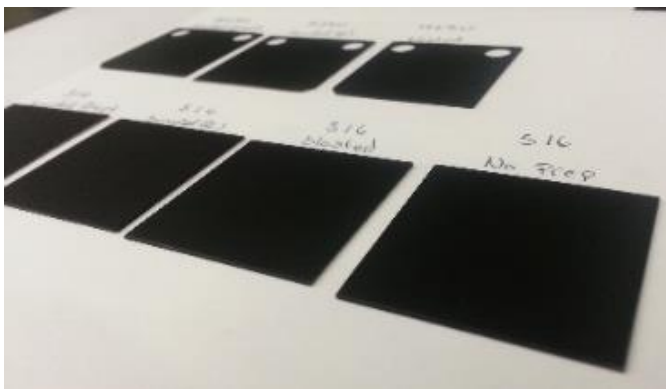
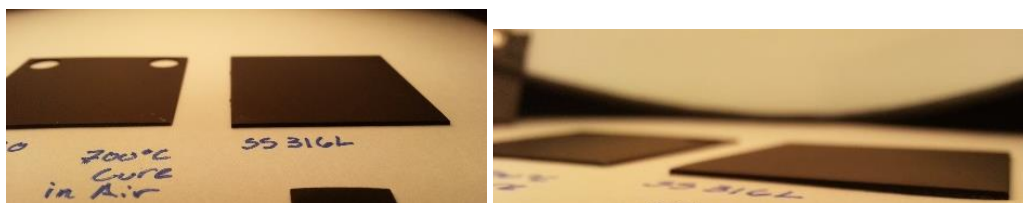


Figure A3. Pyromark 2500 on SS316, reflectivity as a function of wavelength



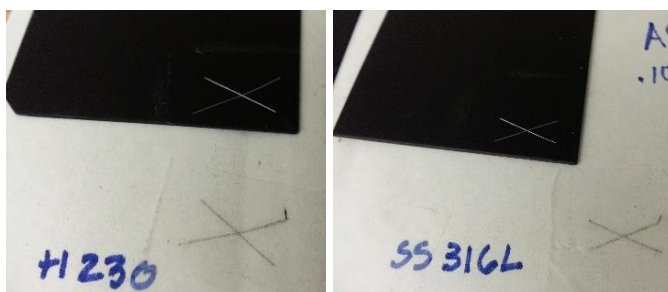
Pyromark 2500 Post air cure



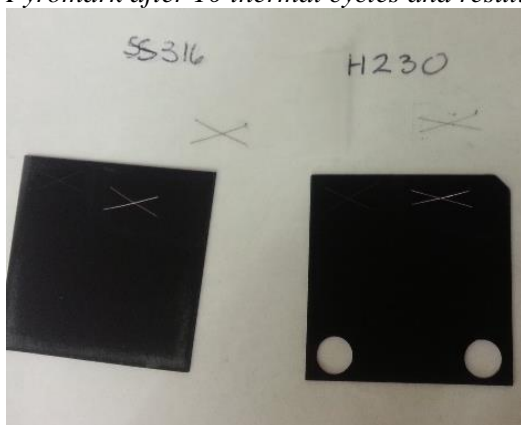
Pyromark 2500 Post oven cure



Pyromark 2500 after 10 thermal cycles



Pyromark after 10 thermal cycles and results of the mechanical tape test



Pyromark 2500 after 50 thermal cycles and results of the mechanical tape test

Mechanical testing was completed following the ASTM D3359-97 standard for adhesion by tape test. Scotch pressure sensitive tape produce by 3M was utilized. Since

the test specimens are small method B outlined in the standard was followed. An “X” formed by cutting two intersecting lines with a small angle of 30-45° into the coating such that bare metal shows. The tape is then applied and rubbed into place until uniform coloration occurs. The tape used went from a frosty white to clear under complete contact. For consistency the tape was allowed to rest for 1 minute prior to removal. Visual results for the tests are shown in Fig. A6 above. As can be seen the Pyromark shows no signs of lift except with in the cut line giving a rating of 5A, which is satisfactory. From the conducted test, Pyromark is shown to be a robust coating based on the refined application and curing process laid out by Sandia National Labs. Due to a failure of the power supply of the solar concentrator at the time of this study no “on sun” tests have been conducted using the improved curing process of Pyromark 2500.

8.2 Detailed Pressure Testing Procedure

ASME code for pressure testing:

The proof test required for verifying the applicability of test article of Option 1 under experiment conditions, can be performed according to ASME Section VIII Div. 1 codes. This division is including ASME codes pertained to boiler and pressure vessel. The maximum allowable working pressure (MAWP) for vessel/vessel parts for which the strength cannot be computed with satisfactory assurance of accuracy has to be assessed based on the requirements mentioned in paragraph UG-101.

Determination of the internal MAWP:

<p>Tests based on yielding of the part to be tested.</p> <p>Limited to:</p> $\frac{\text{Min specified yield}}{\text{Min specified ultimate strength}} \leq 0.625$ <p>For H230 usually it is true (Table 1).</p>	<p>Tests based on bursting of the part.</p>
---	--

Table 1: Tensile properties for hot-rolled and (1232C) annealed H230 plate

Temperature (C)	Ultimate tensile strength (MPa)	Yield strength (MPa)	Yield/ Ultimate tensile
Room	840	375	0.446
538	690	251	0.364
649	662	255	0.385
760	530	253	0.477
871	315	242	0.768

- The part shall not previously have been subjected to a pressure greater than 1.3 times the desired or anticipated MAWP.

- When the MAWP has been established by a proof test, duplicate parts need not to be proof tested. To determine a part as a duplicate all the requirements mentioned in paragraph UG-101-d-1 shall be met. The headline of those requirements can be named such as the same basic design configuration and type of construction, the same material specifications, the same nominal dimensions and the same heat treatment.

- As a check that the measurements are being taken on the most critical areas, the Inspector may require a brittle coating to be applied on all areas of probable high stress concentrations. The surfaces shall be suitably cleaned before the coating is applied in order to obtain satisfactory adhesion.

The parts being proof tested shall be examined between pressure increments for signs of yielding as evidenced by flaking of the brittle coating, or by the appearance of strain lines. The application of pressure shall be stopped at the first sign of yielding, or if desired, at some lower pressure.

- The applying pressure shall be increased gradually until approximately one-half the anticipated working pressure is reached. In our case about 60 bar.

- Thereafter, the test pressure shall be increased in steps of approximately one-tenth or less of the anticipated MAWP. In our case steps less than 12 bar.

- The pressure shall be held stationary at the end of each increment for a sufficient time to allow the observations required by the test procedure to be made.

MAWP calculation based on performed proof test:

- **Tests based on yielding**

P_t is MAWP at the proof test temperature. For any acceptable material listed in this division (Div. 1¹);

$$P_t = 0.4H$$

Where H is the hydrostatic test pressure at which the test was stopped, psi (kPa).

- **Tests based on bursting**

The MAWP of any component part proof tested by this method shall be established by a hydrostatic test to failure by rupture of a full-size sample of such pressure part. The hydrostatic pressure at which rupture occurs shall be determined. Alternatively, the test may be stopped at any pressure before rupture that will satisfy the requirements for the desired MAWP. Based on the measured pressure, MAWP can be determined by:

$$P_t = \frac{B}{4} \times \frac{S_\mu E}{S_{\mu r}}$$

Where B is the bursting test pressure or hydrostatic test pressure at which the test was stopped. E is the efficiency of welded joint (Table UW-12) which for our case it is 1.

S_μ is specified minimum tensile strength at room temperature. $S_{\mu r}$ is the maximum tensile strength of range of specification at room temperature.

¹ Referring to H-230 spec sheet Haynes 230 alloy is covered by ASME Vessel Code case No. 2063 for Section I and Section VIII Division 1 construction to 1650°F (899°C).

MAWP at Higher Temperatures:

If the part is going to be utilized in an application with higher temperature which cause the allowable stress value of the material drops to less than the value used for the proof test, the new MAWP can be determined by the following formula:

$$P_0 = P_t \frac{S}{S_2}$$

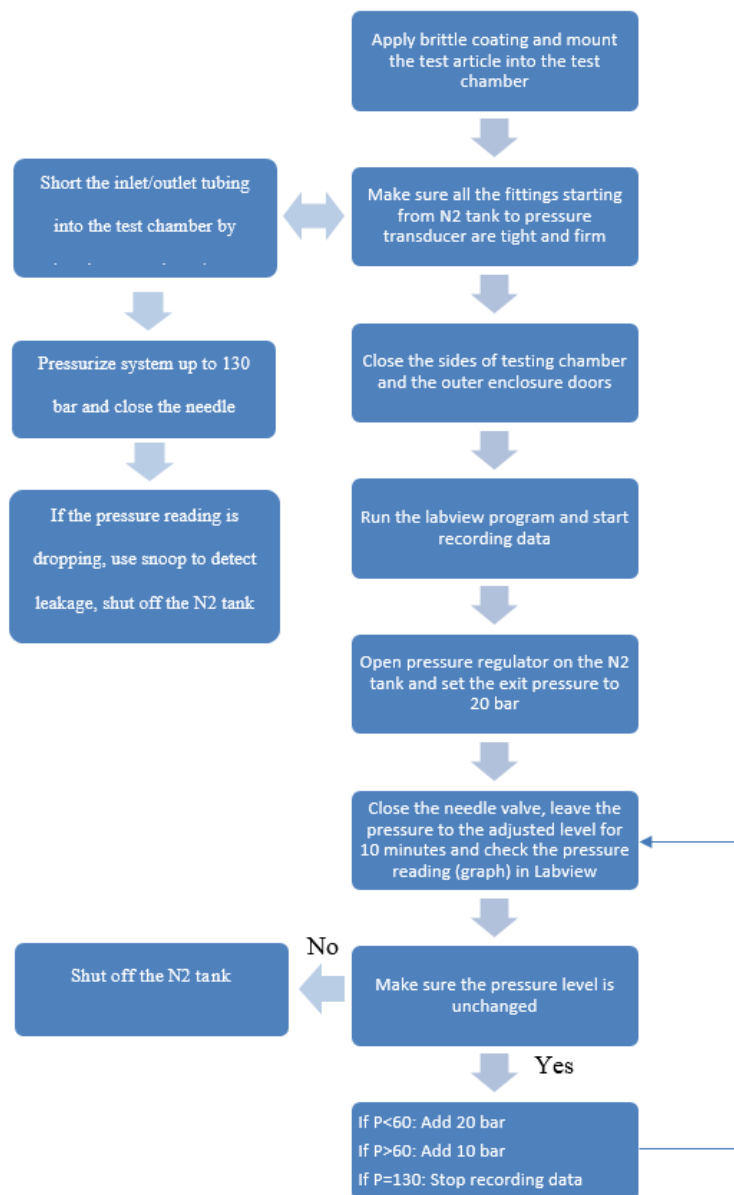
Where P_0 is MAWP at the design temperature, P_t is MAWP at the proof test temperature, S is maximum allowable stress value at the design temperature and S_2 is maximum allowable stress value for the material at the temperature used in the proof test.

Test gages

- An indicating gage shall be connected directly to the vessel. If the indicating gage is not readily visible to the operator controlling the pressure applied, an additional indicating gage shall be provided where it will be visible to the operator throughout the duration of the test.
- Dial indicating pressure gages used in the testing in no case shall the range be less than 1.5 nor more than 4 times of the maximum test pressure.
- All gages have to be calibrated.

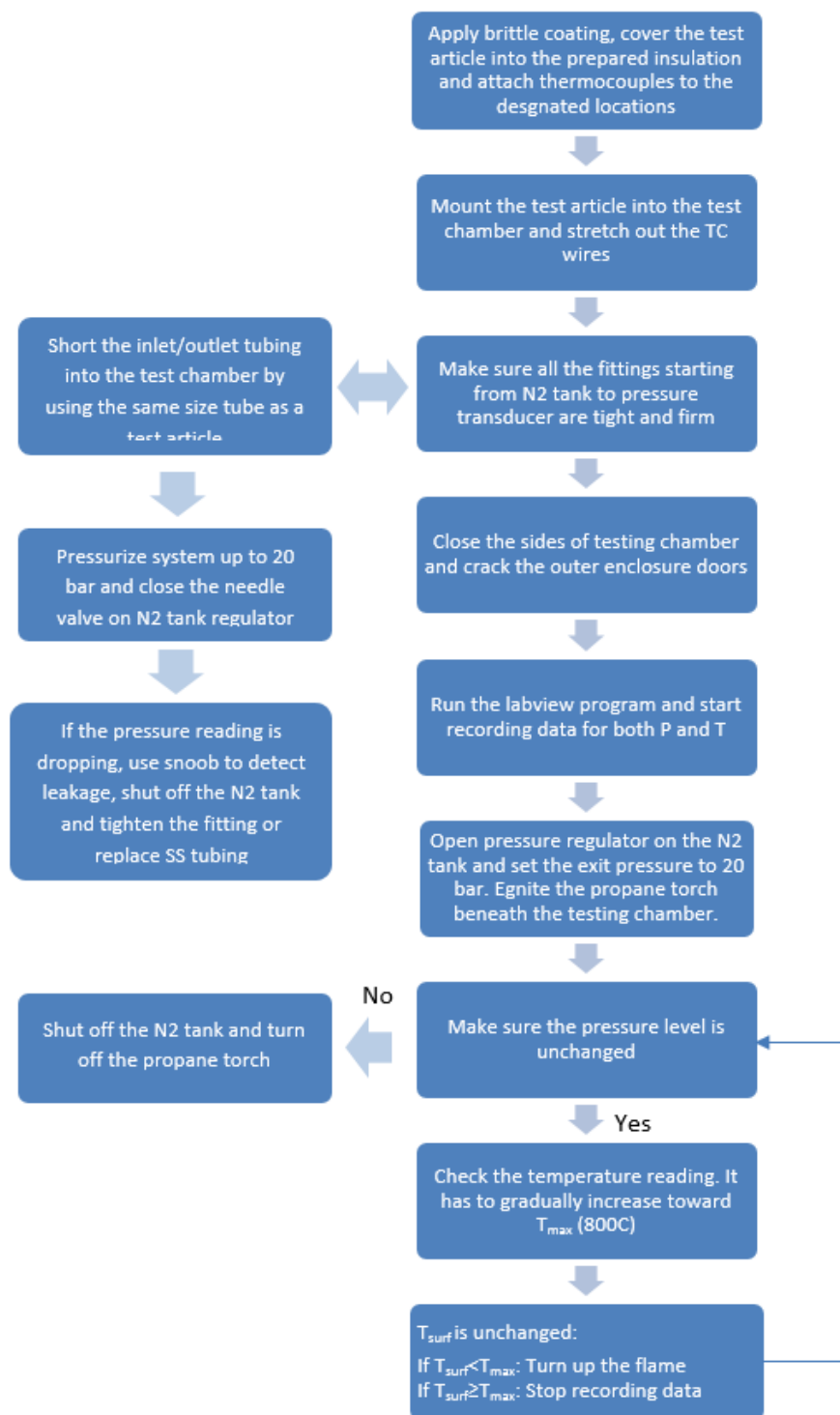
Test article pressure testing procedure

Based on the summary of ASME Section VIII Div. 1 UG-101 code which is reviewed above, the following procedure will be followed for pressure testing of LSR and IR test articles.



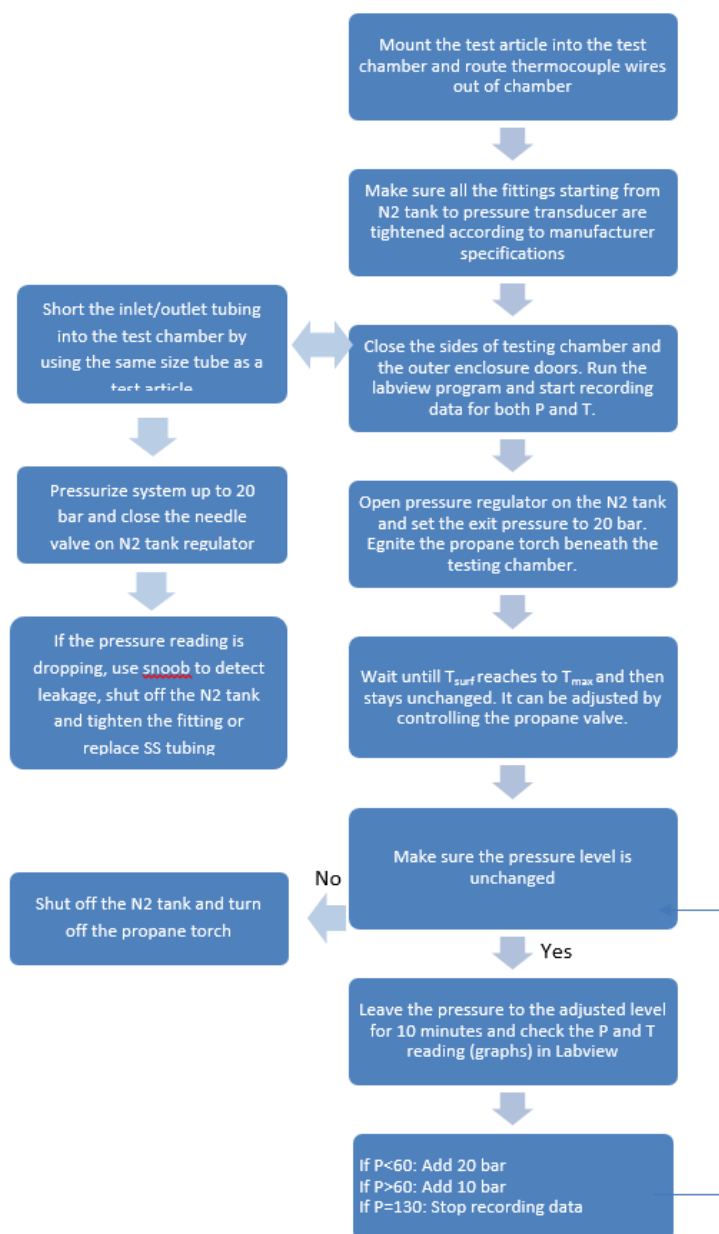
Temperature testing procedure

Following procedure will be followed for temperature testing of LSR and IR test articles.



Test article pressure and temperature testing procedure

Following procedure will be followed for temperature testing of LSR and IR test articles.



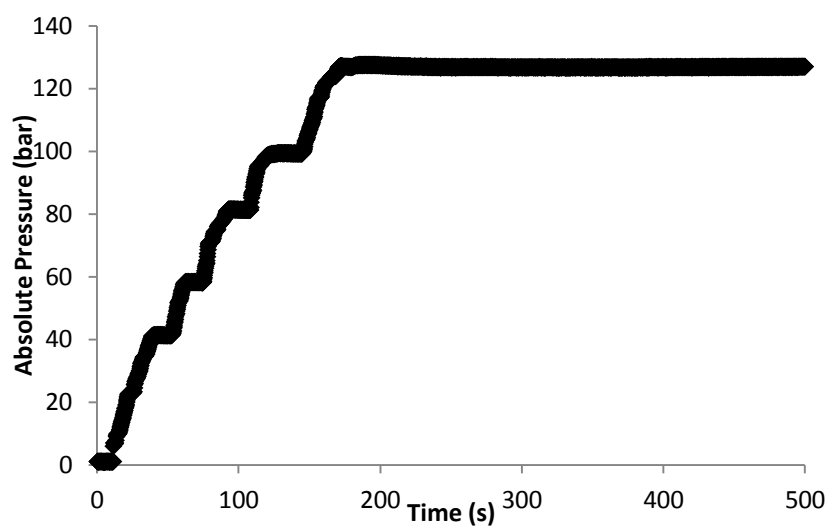


Figure 1: Leakage test of facility (tubing and fittings) by shortening the inlet and outlet of test chamber

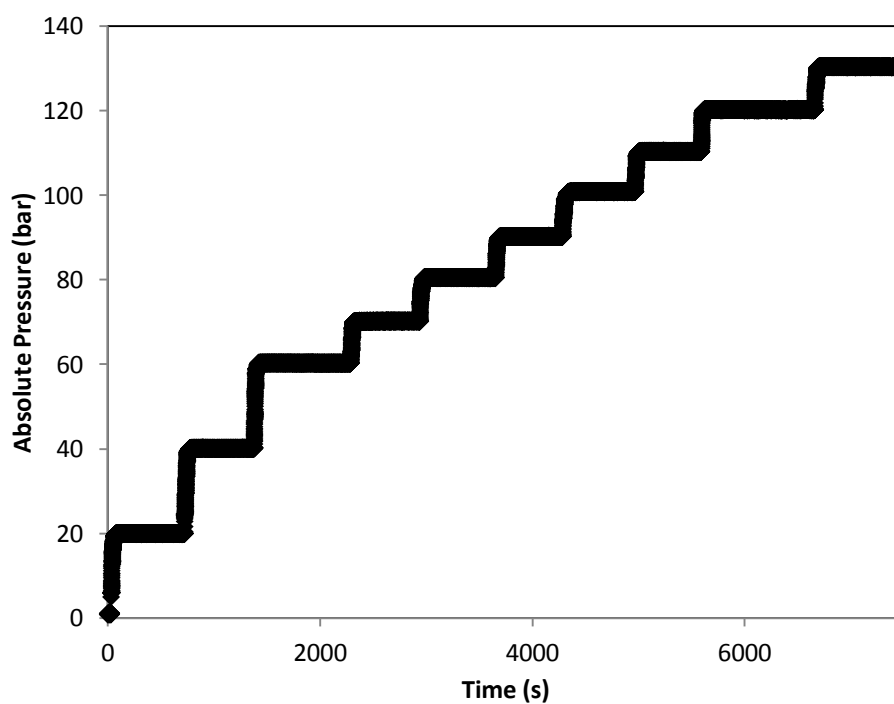


Figure 2: Pressure testing of test article option 1 according to the described procedure

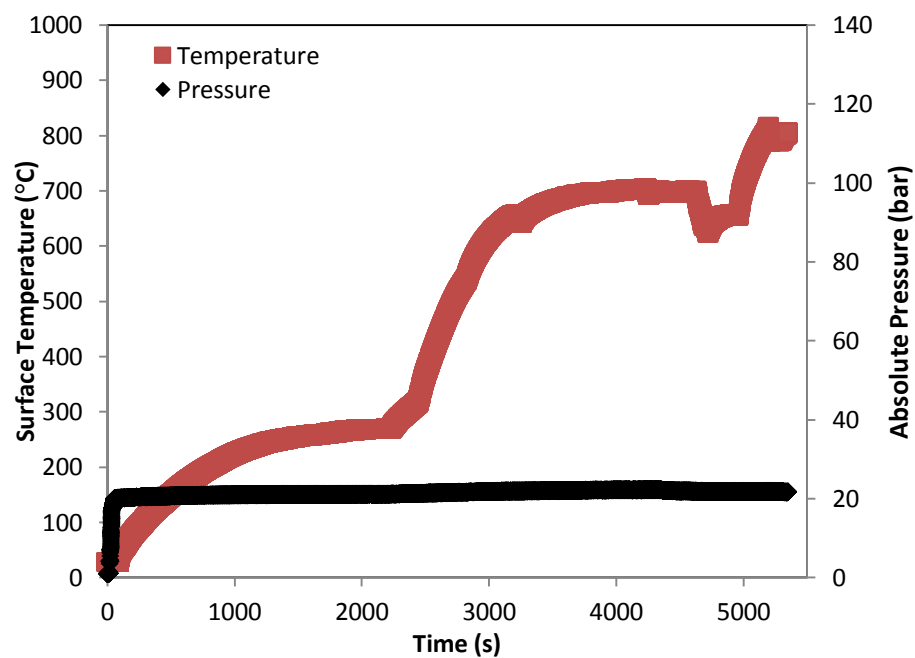


Figure 3: Temperature testing of test article option 1 according to the described procedure

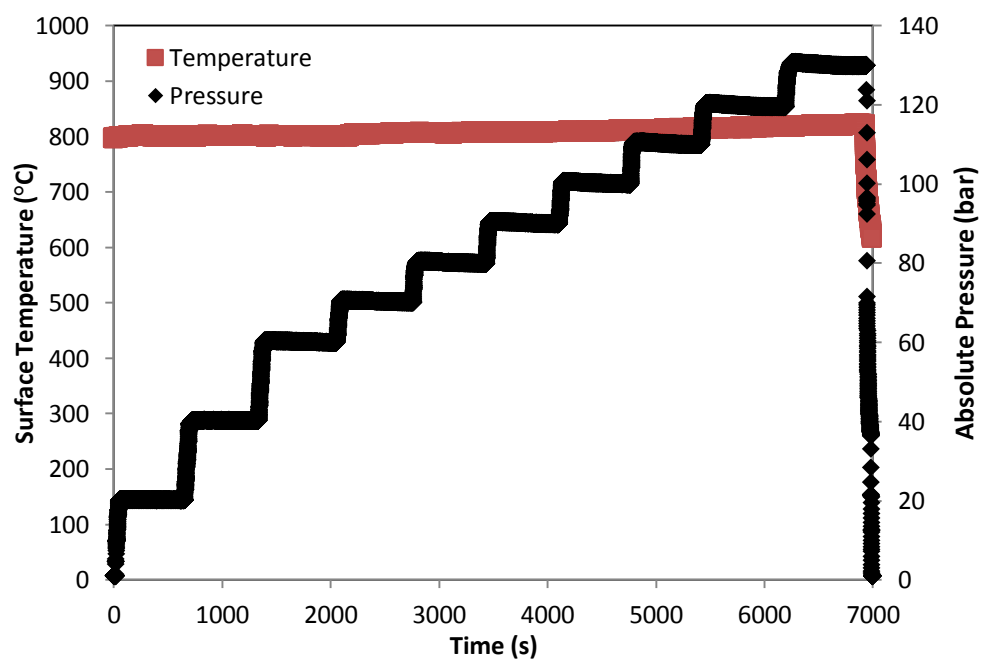


Figure 4: Temperature and Pressure testing of test article option 1 according to the described procedure

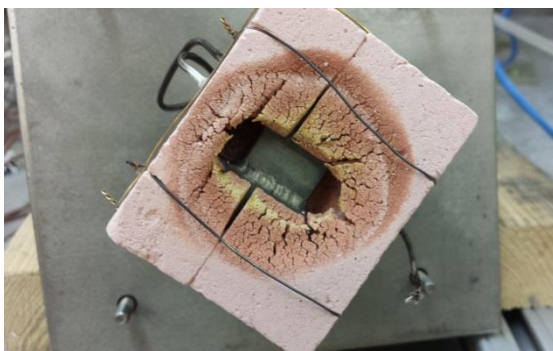
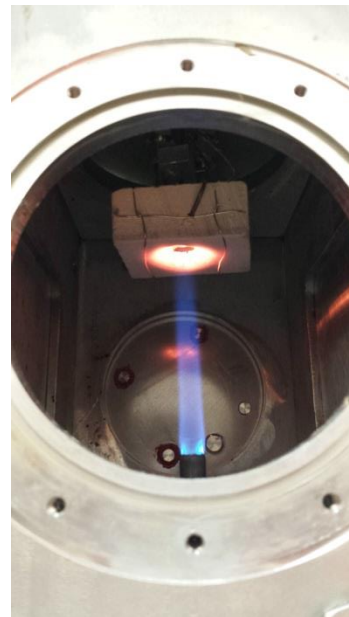
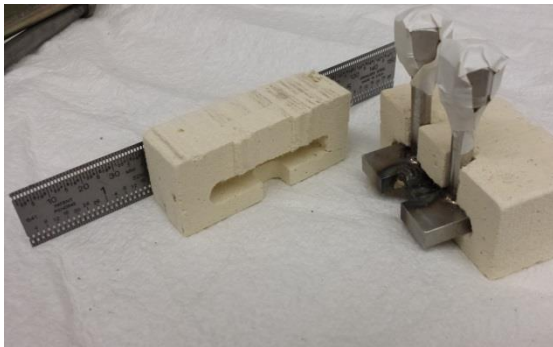


Figure 5: Different views of test article option 1 before, in the middle and after the pressure and temperature test